



HAL
open science

Four-dimensional dose calculation using deformable tetrahedral geometries for hadron therapy

Yazid Touileb

► **To cite this version:**

Yazid Touileb. Four-dimensional dose calculation using deformable tetrahedral geometries for hadron therapy. Modeling and Simulation. Université lyon 1, 2019. English. NNT : . tel-03019256

HAL Id: tel-03019256

<https://hal.science/tel-03019256>

Submitted on 23 Nov 2020

HAL is a multi-disciplinary open access archive for the deposit and dissemination of scientific research documents, whether they are published or not. The documents may come from teaching and research institutions in France or abroad, or from public or private research centers.

L'archive ouverte pluridisciplinaire **HAL**, est destinée au dépôt et à la diffusion de documents scientifiques de niveau recherche, publiés ou non, émanant des établissements d'enseignement et de recherche français ou étrangers, des laboratoires publics ou privés.



N° d'ordre NNT : xxx

THÈSE DE DOCTORAT DE L'UNIVERSITÉ DE LYON
opérée au sein du
Laboratoire d'InfoRmatique en Images et Systèmes d'information
Université Claude Bernard Lyon 1

École Doctorale ED512
InfoMaths

Spécialité de doctorat : Informatique

Soutenue publiquement le 30/09/2019, par :
Yazid Touileb

**Four-dimensional dose calculation using deformable
tetrahedral geometries for hadron therapy**

Devant le jury composé de :

Lydia Maigne, Maître de conférences, Université Clermont Auvergne
Marc Neveu, Professeur des Universités, Université de Bourgogne
Laurence Cheze, Professeure des Universités, Université Lyon 1
Alamin Mansori, Professeur des Universités, Université de Bourgogne
Juliette Thariat, Professeure des Universités, Centre Antoine Lacassagne

Rapporteure
Rapporteur
Examinatrice
Examinateur
Examinatrice

Behzad Shariat, Professeur des Universités, Université Lyon 1
Michael Beuve, Professeur des Universités, Université Lyon 1
Hamid Ladjal, Maître de conférences, Université Lyon 1

Directeur de thèse
Co-directeur de thèse
Co-directeur de thèse

Four-dimensional dose calculation using deformable tetrahedral geometries for hadron therapy

ABSTRACT: The estimation of energy and dose distribution patterns in respiratory-induced organ motion constitutes a significant challenge in hadron therapy treatment planning and dosimetry. Notably for lung cancer in which many difficulties arise, like tissue densities variation and the tumor position shifting during Respiration. All these parameters affect the ranges of protons or ions used in treatment when passing through different tissues and can easily result in Unexpected dose distribution. The present work consists of calculating the dose distributions of moving organs by means of Monte Carlo simulations and patient-specific modeling tools. The dose distributions are calculated using a time-dependent tetrahedral density map, describing the internal anatomy of the human body. Additionally, the internal motion can be described using either a biomechanical modeling based on Finite Element Analysis (FEA) or deformable image registration displacement map. Unlike methods based on the conventional voxel-based structures, the deposited energy is accumulated inside each tetrahedron during deformation, thus overcoming the problem of tissue tracking since that the tetrahedron is defined as a part of a tissue whose chemical composition and topology do not change. The first part of the Ph.D. project proposes a dose calculation method that generates a 4D dose map using a patient-specific tetrahedral model. Besides, we study the effect of the level of detail of tetrahedral meshes on the accuracy of the resulted dose distribution. In the second part, we focus on the optimization of the tetrahedral geometry to address the problem of time simulation, since obtaining a precise dose distribution can be very time-consuming. To overcome this issue, we've defined a new approach that takes into account the direction of the beam to minimize the error of the water equivalent thickness of the tetrahedrons before the tumor volume. This method allows for a coarsened tetrahedral mesh and as a result, improved computational performance in Monte Carlo simulations while guaranteeing a precise dose distribution in the target volume.

KEYWORDS: Hadrontherapy, tetrahedral meshes, voxel-based structures, dosimetry, Monte carlo, modeling

Calcul de dose 4D à l'aide des structures tétraédriques déformables pour l'hadronthérapie

RÉSUMÉ: L'estimation de la distribution de dose et d'énergie en présence du mouvement des tissus induit par la respiration, constitue un défi technologique important dans la planification du traitement en hadronthérapie. Notamment pour le cancer pulmonaire, dans lequel de nombreuses difficultés apparaissent comme la variation de densité des tissus, le changement de la forme des organes ainsi que le décalage de la position de la tumeur pendant la respiration. Tous ces paramètres affectent la portée du faisceau d'ions utilisés pendant le traitement, et, par conséquent entraînent une distribution de dose inattendue. L'objectif principal de cette thèse est de proposer une méthode de calcul de dose basée sur les structures tétraédriques, qui permet d'estimer les distributions de dose des organes en mouvement en utilisant les simulations Monte Carlo. Ces distributions de dose sont calculées en utilisant une carte de densité tétraédrique dépendante du temps, décrivant l'anatomie interne du corps humain. De plus, le mouvement interne peut être représenté à l'aide d'une modélisation biomécanique résolue par la méthode des éléments finis (MEF) ou d'une carte de déplacement issue d'un recalage d'images déformable. Contrairement aux méthodes basées sur les structures classiques à base de voxels, la dose déposée s'accumule à l'intérieur de chaque tétraèdre au cours de la déformation, surmontant ainsi le problème du suivi tissulaire puisque le tétraèdre est défini comme une partie d'un tissu dont la composition chimique et la topologie ne changent pas. Dans la première partie de la thèse, nous avons développé une méthode de calcul de dose qui génère une carte de dose 4D en utilisant un modèle tétraédrique spécifique au patient. En outre, nous étudions l'effet du niveau de détail des maillages tétraédriques sur la précision de la distribution de la dose obtenue. Dans la deuxième partie, nous nous concentrons sur l'optimisation de la géométrie tétraédrique pour réduire le temps de simulation, sachant que l'obtention d'une distribution de dose précise peut être coûteux en termes de temps. Pour surmonter ce problème, nous avons proposé une nouvelle approche qui prend en compte la direction du faisceau afin de minimiser l'erreur de l'épaisseur équivalent eau des tétraèdres avant le volume de la tumeur. Cette

méthode permet d'obtenir un maillage tétraédrique grossier et, par conséquent, d'améliorer les performances de calcul dans les simulations de Monte Carlo, tout en conservant une distribution de dose précise dans le volume cible.

MOTS CLÉS: hadronthérapie, maillages tétraédriques, structures voxéliques, dosimétrie, Monte Carlo, modélisation

Publications related to this work

Peer-reviewed journal articles:

Yazid Touileb, Hamid Ladjal, Michael Beuve, and Behzad Shariat. "Particle-beam-dependent optimization for Monte Carlo simulation in hadrontherapy using tetrahedral geometries". *Physics in Medicine and Biology*, 63(13), 2018. ISSN 13616560. doi: 10.1088/1361-6560/aacbe5.

Conference contributions:

Yazid Touileb, Petru Manescu, Hamid Ladjal, Joseph Azencot, Michael Beuve, and Behzad Shariat. "Motion-induced Monte Carlo dose calculation using deformable tetrahedral meshes". In 2016 IEEE 13th International Symposium on Biomedical Imaging (ISBI) 16 avril 2016, Prague (République Tchèque), pages 1257–1260. IEEE, apr 2016. ISBN 978-1-4799-2349-6. doi: 10.1109/ISBI.2016.7493495.

Yazid Touileb, Hamid Ladjal, Joseph Azencot, Michael Beuve and Behzad Shariat, "4D dose calculations: Tetrahedral meshes versus voxel-based structures" (2016), ICTR-PHE 2016, 19 février 2016, CERN, Genève (Suisse)

Petru Manescu, Hamid Ladjal, Yazid Touileb, Joseph Azencot, Michael Beuve & Behzad Shariat (2016). "4D POSITRON EMISSION TOMOGRAPHY IMAGE RECONSTRUCTION BASED ON BIOMECHANICAL RESPIRATORY MOTION". IEEE International Symposium on Biomedical Imaging (IEEE ISBI), 16 avril 2016, Prague (République Tchèque), pp. 99-102. HAL : hal-01267527.

Hamid Ladjal, Nadir Skendraoui, Matthieu Giroux, Yazid Touileb, Joseph Azencot, Michael Beuve, Philippe Giraud & Behzad Shariat (2015). "Physiological and Biomechanical Model of Patient Specific Lung Motion Based on 4D CT Images". The 8th Biomedical Engineering International Conference (IEEE BMEiCON2015), 27 novembre 2015, Patt (Thaïlande), pp. 1-5. HAL : hal-01214310.

Contents

1	INTRODUCTION	1
1.1	Radiation therapy for cancer treatment	1
1.1.1	Mechanisms of action of radiotherapy	2
1.1.2	Radiation therapy in history: from conventional radiotherapy to hadron therapy	3
1.1.3	Hadrontherapy	4
	Beam delivery systems	5
1.2	Treatment of moving targets using heavy charged particles	9
1.2.1	Organ motion from a clinical view	9
1.2.2	Respiratory motion	10
1.2.3	Dosimetric consequences of target motion	10
1.2.4	Density variations	12
1.3	Medical strategies to deal with motion	14
1.3.1	Motion Reduction techniques	14
1.3.2	Rescanning or repainting	15
1.3.3	Respiratory gating approach	15
	Expansion of the planned target volume	15
1.3.4	Real-time tumor tracking	16
1.3.5	Adaptive Radiotherapy	17
1.4	Aims and structure of the thesis	17

2	MOTION-INDUCED MONTE CARLO DOSE CALCULATION USING DEFORMABLE TETRA-	
	HEDRAL MESHES	20
2.1	Introduction	20
2.2	Dose calculation methods	21
2.2.1	Pencil beam algorithms	21
2.2.2	Ray-casting algorithms	22
2.2.3	Monte Carlo methods	22
2.3	Respiratory motion estimation	24
2.3.1	Image-based motion estimation approaches	24
2.3.2	Biomechanical methods	26
2.4	Modeling of moving organs in hadrontherapy	27
2.5	Continuous representation of moving organs	31
2.5.1	results	36
2.6	Tetrahedral mesh creation and density mapping: From voxel-based geometries to tetrahedral models	36
2.6.1	Mapping voxel densities into tetrahedral elements	37
	Tetrahedral mesh generation	37
	Density mapping	38
2.6.2	Time-dependant dose computation on deformable tetrahedrons	40
2.6.3	GEANT4-based implementation	41
2.6.4	Beam shaping and configuration	42
2.7	Evaluation and Results	44
2.7.1	Concentric spheres phantom	44
2.7.2	Patient case simulation	46
2.7.3	Density evaluation and dose distribution comparison	48
2.7.4	discussion and conclusion	50
2.8	Multiresolution tetrahedral model creation	51
2.8.1	Multiresolution tetrahedral model	51
	Tetrahedral model generation process	52
	Tetrahedralization and generation of different Levels of detail (LODs):	52
	Geometry configuration	53

Results and discussion	53
2.9 Conclusion	55
3 PARTICLE-BEAM-DEPENDENT OPTIMIZATION FOR DOSE CALCULATION	61
3.1 Introduction	61
3.2 Conclusion	62
3.3 The article	62
4 MOTION COMPENSATION OF WEPL FOR 4D DOSE CALCULATIONS	86
4.1 Introduction	86
4.2 Calculation of water equivalent thickness in proton beam irradiation	87
4.3 CT HU-to-Stopping Power Calibration	89
4.4 Multi-layer phantom (MLP) case	89
4.5 Experimental calculation of the WEPL	91
4.6 Effective density calculation using stoichiometric WEPL	94
4.7 Evaluation and result	96
4.7.1 simulation setup	97
4.7.2 4D Dose evaluation	98
4.8 Conclusion	103
5 GENERAL CONCLUSIONS AND FUTURE PERSPECTIVES	104
APPENDIX A LINEAR INTERPOLATION	107
A.1 Linear density variation	107
A.2 Linear Interpolation resampling (LR)	110
A.3 Resampling using Nearest Neighbor Interpolation (NN)	110
LIST OF FIGURES	114
LIST OF TABLES	115
REFERENCES	141

Acknowledgments

This PhD is supported by LABEX PRIMES (ANR-11-LABX-0063), within the program Investissements d'Avenir (ANR-11-IDEX-0007) and by France Hadron, and by ClaRys project CNRS, defis Imaging.



List of Acronyms

BP	Bragg Peak	HT	Hadron Therapy
CDT	Constrained Delaunay Detrahedralization method	HU	Hounsfield Unit
CDVH	Cummulative Dose-Volume Histogram	LOD	Level Of Detail
CM	Centroid Mapping method	MC	Monte Carlo
CMCM	Continuous Mass Conserving Mapping method	MCM	Mass conserving mapping method
CSG	Constructive Solid Geometry	MLC	Multi-Leaf Collimator
CT	Computed Tomograpy	MLP	Multi-Layer Phantom
CTV	Clinical Target Volume	OAR	Organs At Risk
DIR	Deformable Image Registration	PTV	Planning Target Volume
DTA	Distance To Agreement	RC	Range Compensator
DVF	Deformation Vector Field	RT	Radiation Therapy
EFFD	EFFective Density mapping method	SOBP	Spread Out Bragg Peak
FEM	Finite Element Methods	WEPL	Water Equivalent Path Length
GTV	Gross Target Volume	WET	Water Equivalent Thickness
HI	Homogeneity Index		

Learning never exhausts the mind.

Leonardo da Vinci

1

Introduction

In this chapter, we present the background and the objectives of our study. We first start with an overview of hadrontherapy and its use in cancer treatment then; we give an insight into the techniques used to incorporate organ movement. Finally, we end with a description of the goals of the present thesis and the structure of this manuscript.

1.1 RADIATION THERAPY FOR CANCER TREATMENT

Radiotherapy also known as radiation therapy or RT is one among five modalities of cancer treatment alongside surgery, chemotherapy, immunotherapy and hormonal therapy. It is considered as an essential element for effective cancer treatment since more than 50% of all patients worldwide receive radiotherapy during the management of their disease [1][2]. Either stand-alone or combined with another modality depending on the stage and the type of cancer. In RT, the radiations are delivered in three distinctive ways :

- **Brachytherapy (BT) or sealed source radiation therapy** sometimes referred to as curietherapy or endocurietherapy. In this form of RT, the radioactive sources are placed within or adjacent to the site of the cancerous tumor to deliver higher radiation doses [3]. For instance, a radiation source will be placed in the breast of a woman who has breast cancer. BT technique is widely used for breast, cervical, prostate, and skin cancers.
- **Radioisotope therapy or unsealed source radiotherapy** applied through the systemic injection of radioactive substances radiopharmaceuticals that have been designed to target disease. [4]. The radiation source is given orally or intravenously through an intravenous tubing. The most common cancer treated with radioisotope therapy is the thyroid cancer.
- **External beam radiation therapy (EBRT or XRT) or teletherapy** contrary to the other two methods, the beam in EBRT is delivered from outside the body using an external source of ionizing radiation and pointed to the target.

In this manuscript, our work will revolve mainly around the external beam radiation therapy, and we will refer to it therefore as radiation therapy.

1.1.1 MECHANISMS OF ACTION OF RADIOTHERAPY

The idea behind radiotherapy is to kill the tumoral cells using ionizing radiations. As the term implies, these radiations form ions and deposit energy in the tissues traversed by the beam, thus damaging their DNA or other critical cellular molecules. The energy deposition can either kill the cells immediately or cause genetic changes that lead to cell death [5]. As a result, the cell division process will be blocked, and further cell proliferation will be prevented [6]. Nevertheless, Since that normal cells may also be damaged and killed during irradiation, the goal of radiation therapy is to minimize exposure to healthy tissues while maintaining a high dose value in the target. Fortunately, Normal cells can repair themselves at a fast rate and retain their usual function statuses contrary to cancer cells which are not as efficient to fix the damage caused by the radiations [7].

1.1.2 RADIATION THERAPY IN HISTORY: FROM CONVENTIONAL RADIOTHERAPY TO HADRON THERAPY

The first to use ionizing radiation for a therapeutic application and to demonstrate the biological effects of x-rays on tissues was the professor Leopold Freund [8]. Very soon after the discovery of x-rays by Wilhelm Röntgen in 1895 [9], he successfully treated in 1896 a five-year-old girl suffering from hairy moles covering her back, thus becoming the founder of medical radiology and radiotherapy [10]. In the early twentieth century, an increasing number of the studies that use x-rays in medicine was reported. However, due to the low penetration of the radiations in tissues, the treatments were limited to superficial and shallow-seated tumors like in skin cancer. Besides, the lack of knowledge of the mechanisms of actions and the biological effects of the new rays conducted to poor cancer treatment and lower delivery control compared to the produced side effects [11] [12]. These outcomes have pushed physicians to study the properties of these new radiations and radiobiologists to investigate the impact of the particle beams on cell survival. By the end of this period of radiation medicine known as the era of discovery [13] in the late 1920s, researchers were able to understand the characteristics of the newly discovered beams and their effects on tissues, especially following the work of Ernest Rutherford on the atomic structure. Moreover, radioactive elements were also identified and diligently studied, as well. Not less important was the introduction of the ionizing chamber that made the measurement of the delivered radiation dose possible. In the following decades, radiation therapy became one of the main modalities used for oncology, and many technical advances have been made to enhance the quality of the treatment. These methods aim to improve the conformity of the administered dose to the target volume by limiting a high and a homogeneous dose in the diseased area and spare the surrounding healthy tissues to avoid unwanted side effects for the patient. Among the techniques that have made a significant impact on the quality and the precision of the beam delivery, we found computerized treatment planning systems, setup and patient positioning and the megavoltage x-rays. Another strategy that has been used to reduce the dose in critical areas is to take profit of the dose deposition characteristics of the different types of particles. The first to describe the potential of ions for medical use was Robert R. Wilson in 1946 [14]. He outlined the advantages of adopting beams of protons and heavier ions for the treatment of tumors, in comparison with the conventional high energy photon beams (x-rays). The well known physical properties of protons offer a better coverage of dose since that they slow

down during their penetration of the matter. In fact, Wilson has also extended his thoughts to the use of heavy ions.

1.1.3 HADRONTHERAPY

In the literature, multiple terms and designations are used to refer to the treatment of cancer using protons and other heavier ions. The most commonly used are particle therapy, hadrontherapy, hadron therapy and heavy-ion therapy. Even though photons and electrons are also particles, photon therapy, and electron therapy are not considered in particle therapy, but rather, they are usually grouped together and called conventional radiotherapy. To eliminate confusion, the term Hadrontherapy was introduced to cover all forms of radiations that use particles that are made of quarks: protons, neutrons, pions and helium, carbon, oxygen and neon ions, etc. Hence, excluding photons and electrons from the batch. On the other hand, although, there is no difference between Hadrontherapy and the two-separate-words Hadron therapy, the former is preferred [15]. Since, by analogy with radiotherapy, the term radiation therapy was used until it became an important modality in oncology. As for the designation heavy-ion therapy, it is used to characterize ions heavier than protons and also to describe their increased relative biological effectiveness. Currently, only protons and to some extent carbon ions are in use in the clinical environment [16] and thus they will be the focus of the current work.

Beyond the chosen terminology, the rapidly increasing adoption of hadrontherapy in the cancer treatment realm is due to the physical aspects and properties of heavy-ions. More specifically to their distinct depth-dose distribution named Bragg curve after Sir William Henry Bragg, who discovered it in 1903 [17]. This curve plots the deposited dose of ionizing radiations during their travel through matter, and it is characterized by a pronounced narrow peak known as the Bragg peak (BP). The latter occurs at the end of the range of particles, and it corresponds to the region where a significant amount of energy is deposited. Figure 1.1.1 illustrates a comparison of dose distributions between photons, protons and carbon ions in water using clinical relevant energies. Contrary to photons that have a steep exponential decrease of dose with depth, particle beams have a dose profile that increases up to a sharp maximum with increasing penetration with a very little energy beyond the Bragg peak.

In addition to the favorable dose distribution and the steep dose fall-off of ion beams [19], the

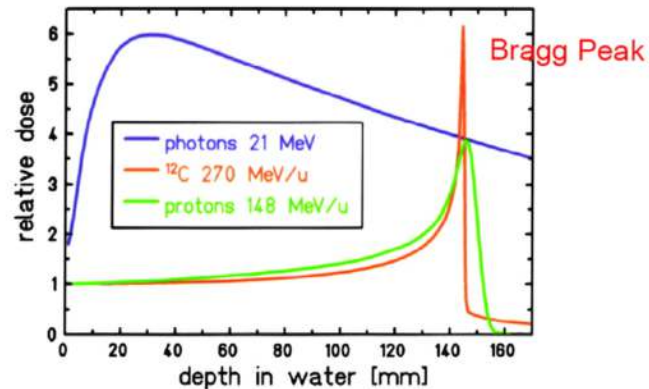


Figure 1.1.1: Depth dose distribution for photons and monoenergetic Bragg curves for carbon ions and protons [18].

position of the BP can be precisely adjusted to the desired depth by changing the kinetic energy of the incident ions. These characteristics yield to better tumor conformity and thus to better clinical outcomes compared to conventional radiotherapy [20]. Figure 1.1.2 illustrates a comparison of proton therapy and X-rays/IMRT treatment plans of esophageal cancer. Even though the dose conformity is precise in the target volume for the two modalities, the dose in the surrounding volumes is far less when using the proton beam.

To cover the entire target volume with a uniform dose distribution, the beam delivery system must extend the Bragg peak over a more significant size creating the so-called Spread-Out-Bragg-Peak (SOBP). The latter is formed by adding the contribution of individually modulated pristine Bragg Peaks. Figure 1.1.3 shows how the proton BPs of different ranges are superimposed to form the SOBP and to produce a homogeneous planned dose in the tumor area.

Beam delivery systems: Hadrontherapy requires complex beam delivery systems that can accelerate the particles to the prescribed energies and transport them onto the target. Since that, a unique Bragg Peak cannot cover the entire volume of the tumor, the ion beam needs to be shaped. Over the years, two major strategies have been developed: passive beam shaping and active scanning. The former method generates a broad therapeutic beam that is further collimated and shaped to conform with the target volume. More precisely, it relies on a combined use of such devices as range modulators, compensators, and wedges. As shown in Figure 1.1.4, the narrow monoenergetic

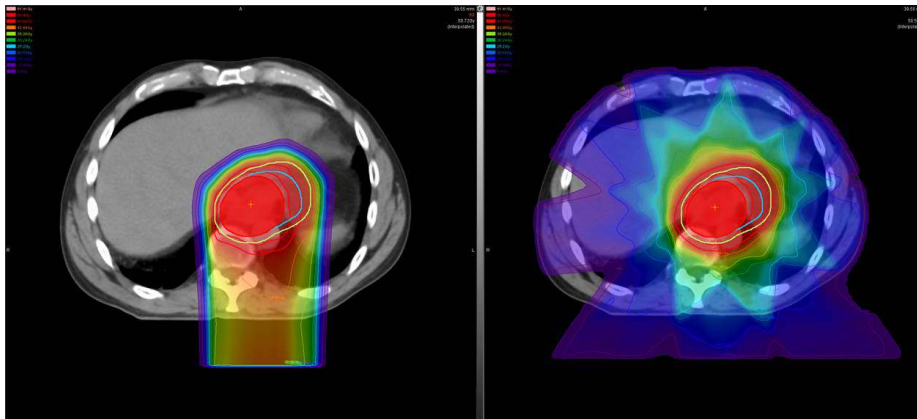


Figure 1.1.2: Treatment plans of esophageal cancer using proton therapy (left) and X-rays/IMRT (right). Proton therapy limits the radiation delivered outside the target and reduces the likelihood of lung complications. The conformity to the target volume is precise in the two cases. However, the dose of surrounding organs is minimized when using protons. Source Seattle cancer care alliance, Proton therapy center 2017 and [21].

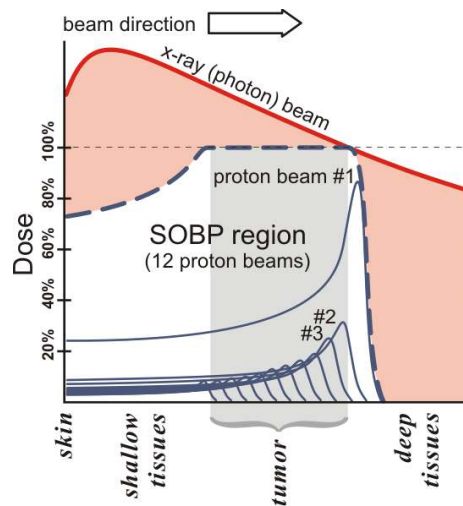


Figure 1.1.3: In a typical treatment plan for proton therapy, the spread out Bragg peak (SOBP, dashed blue line) is the therapeutic radiation distribution. The SOBP is the sum of several individual Bragg peaks (thin blue lines) at staggered depths. The depth-dose plot of an X-ray beam (red line) is provided for comparison. The pink area represents additional doses of X-ray radiotherapy—which can damage normal tissues and cause secondary cancers, especially of the skin

getic Bragg peak generated by the particle accelerator is spread out by the range modulator to generate the SOBP that covers the entire length of the tumor. Furthermore, a range shifter is used to shift the generated SOBP to align it with the depth of the tumor. The following two devices are specifically designed and made individually for each patient: the collimator block the particles that are outside the field of view of the target and finally, the range compensator adjusts the radiation field to the distal depth pattern of the target volume. Despite the fact that the passive beam delivery system is widely used in particle therapy centers around the world, it has significant drawbacks. The fixed width of the SOBP may result in the deposition of dose outside the tumor as illustrated by the hatched area in figure 1.1.4. This is due to the inability of the compensator to form the proximal edge of the target volume that leads to a restricted tumor conformity. Additionally to the need for manufacturing patient-specific hardware that generates more treatment costs, this method generates neutrons that can cause undesirable biological damage in healthy tissues. Those neutrons are the result of the interactions in beam scattering and collimation. However, scattering is more forgiving of tumor and organ motion because of the smearing effect of the broadened beam [22].

On the other hand, the active scanning beam delivery technique (or the Active beam shaping) approach the shaping differently by first dividing the target volume into layers of equal energy, then associating for each slice a grid of target points in a form of voxels. These voxels are furthermore irradiated sequentially by a pencil beam that scans the entire target area. Figure 1.1.5 illustrates how the beam scans the tumor by moving from a slice to another. The pristine Bragg peaks are positioned inside the tumor by employing scanning magnets and also by changing the beam energy. Using such a strategy has the advantage of eliminating the need for any additional patient-specific devices and also reduce drastically the amount of hardware in the beamline leading to less neutron flux towards the patient. Additionally, better conformity to the tumor is ensured hence sparing the surrounding healthy tissues [24]. The active scanning solves some of the weaknesses of the passive strategy regarding the efficiency of the beam delivery as it neither generates neutrons nor has scattered particles in the nozzle. Moreover, it doesn't require the use of complicated and patient-specific devices for the treatment. Nevertheless, the enhanced ability with particle scanning to paint dose more conformally, voxel by voxel, increases the risk of target misses due to breathing. Still, Multiple re-paintings can compensate for the organ motion by effectively smearing out the dose [22].

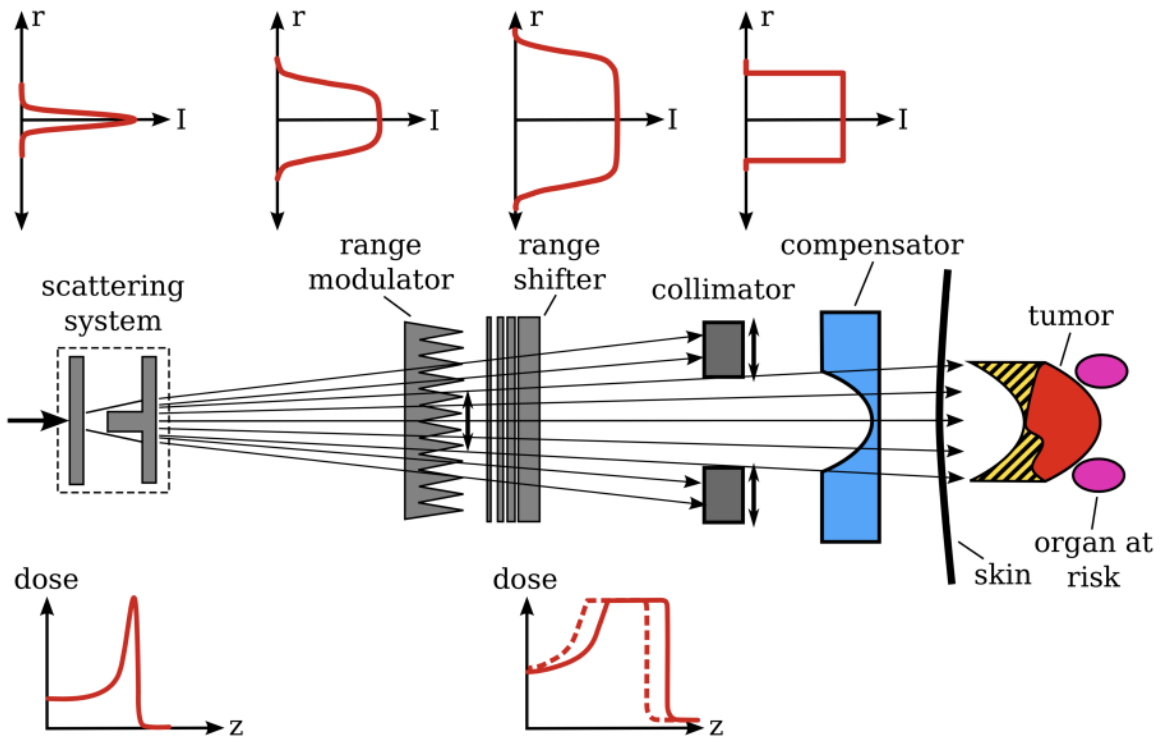


Figure 1.1.4: Schematic of a fully a passive beam shaping system in Hadrontherapy. Figure redrawn from [20].

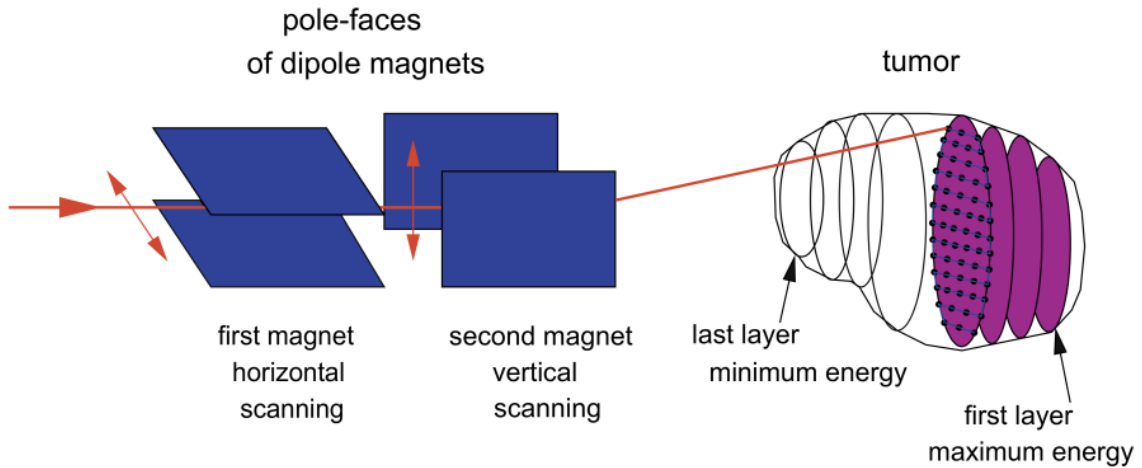


Figure 1.1.5: Schematic of the GSI raster-scan system. Figure redrawn from [23].

1.2 TREATMENT OF MOVING TARGETS USING HEAVY CHARGED PARTICLES

Despite the increased accuracy offered by modern radiotherapy modalities regarding both the treatment precision and the dose conformity, the treatment of moving targets still make a very compelling challenge. Consequently, during the last decades, the management of organ motion established a major research field in radiotherapy. In this section, we will discuss the impact of internal organ motion on the treatment with ion beam therapy and the different strategies employed to mitigate motion effects.

1.2.1 ORGAN MOTION FROM A CLINICAL VIEW

In the following, we will briefly introduce the different types of organ motion and their characteristics. A more extensive review can be found in [25] and [26]. The variation of the density distribution of the patient and the location of the target can occur at different time scales: The entire treatment, in-between sessions and during the treatment delivery.

- **Over the Course of Treatment:** It is referred to the gradual and systematic variation of the density distribution following a redistribution of densities between different tissues or the disappearance or the addition of matter. Examples include shrinkage and tumor growth [27], weight variations and the change in lung density. Moreover, the patterns of motion can also be affected as is the case with breathing trajectories. Furthermore, the patient motion can affect either the inter-fractional or the intra-fractional motions.
- **Inter-fractional organ Motion:** It includes the changes that the anatomy undergoes between treatment fractions and having a more random behavior than the variations that occur over the entire treatment. The sources of inter-fractional changes are diverse and can be the error related to the positioning or the setup of the patient, the changes in the tumor volume or even the daily variation of rectal and bowel filling. Besides, we can also mention the average tumor position that can change during the breathing cycle [26].
- **Intra-fractional organ Motion:** it occurs in the course of a single treatment fraction within a short time interval, and it is mainly originated from the organ motion like swallowing, respiration, heartbeat, organ filling or peristalsis.

Since that the main focus of our work is the treatment of lung cancer, we will emphasize the treatment of intra-fractionally respiratory motion throughout the rest of the document.

1.2.2 RESPIRATORY MOTION

Respiration motion is the primary source of uncertainties during the treatment session [28] [26] [29] and it also contributes to several tumor sites: thorax [30], liver [31], abdominal [32][33], breast, prostate and naturally it constitutes a big challenge for lung cancer [34]. For lung tumors, the motion is more pronounced in the superior-inferior (SI) dimension of the chest cavity and in the regions close to the diaphragm, generating an amplitude that can be as high as 30 mm. The authors in [35] have reported a magnitude of motion less than 13.4 mm for 95% of the lung tumor cases in the SI direction. Additionally, in the study of [36], 35% of total patients have manifested an amplitude greater than 10 mm.

Furthermore, not only the breathing motion is patient-specific but it is also characterized by a random behavior that has patterns that fluctuate in magnitude, period, and regularity. This is due to the fact that the breathing is governed by a set of independent muscles giving a multidirectional facet to the movements. Figures 1.2.1a and 1.2.1b show the patterns of respiration of the same patient taken at very close time intervals. It highlights the necessity of having an individual method for respiratory management. Besides the displacement, breathing may affect the tumor size and shape [37] and also the density of organs over the course of treatment. These uncertainties will have further repercussions on dose delivery for respiratory management.

1.2.3 DOSIMETRIC CONSEQUENCES OF TARGET MOTION

In the case of nonmoving targets, range and patient setup uncertainties are consistent and relatively measurable over the course of treatment and can be taken into account by the treatment planning system to better the target coverage and spare the organs at risk (OAR). Moreover, only one computed tomography image (CT) is needed in the treatment planning to estimate the density of the patient tissues. However, with target motion, more challenging issues are introduced to the treatment planning and dose delivery:

- As opposed to static targets where the density of tissues is assumed to be unchanged during a treatment fraction, handling and representing the variation of the density over time by the

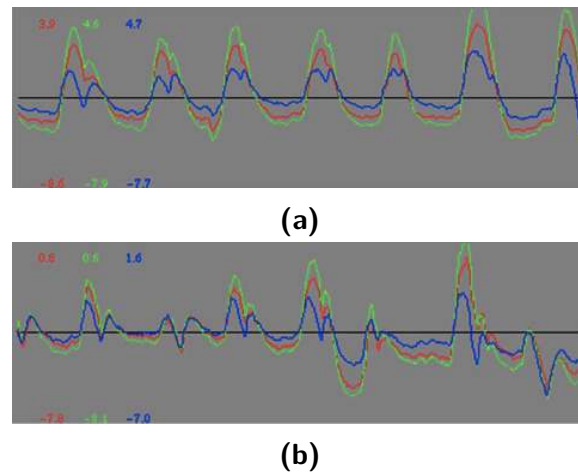


Figure 1.2.1: Fluctuations in respiratory motion patterns registered at close time intervals. The curves represent the patient surface displacement in the superior-inferior, anterior-posterior and medial-lateral dimensions. In (a) the patterns are almost identical but in (b) there are no respiratory distinguishable patterns [34].

planning system is not straightforward. Even by using 4D CT scans that only represent a snapshot in time of the patient geometry.

- Target motion may result in the interplay effect which is the interaction between the beam delivery and the tumor when they have similar time structures.
- The displacement of the target during treatment needs to be estimated and taken into account to adjust the dose distribution determined by the treatment plan.

The classical treatment planning approach that consists of using a single CT scan is limited and insufficient to handle moving targets due to the above-mentioned reasons. Using this approach will clearly generate a discrepancy between the planned dose and the real delivered dose. The deviation of the dose distribution for a circular phantom is illustrated in Figure 1.2.2. It shows how the dose distribution has deformed for a displacement of 10 mm resulting in an under dosage of the tumor and affecting the surrounding tissues.

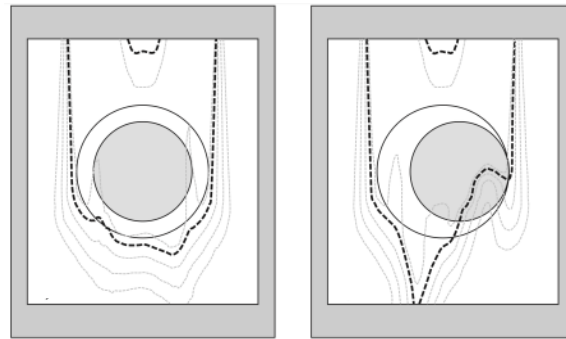


Figure 1.2.2: Effect of target motion on a circular phantom. The tumor is centered and it is represented by the gray circle. The thin black circle indicates a 10-mm 3D geometric expansion of the tumor into the planning target volume (a) The dashed lines are isodose lines (50%, 80%, 90%, 95%, 100% of the maximum dose) for a single passive proton beam. (b) Isodose lines for a 10 mm displacement of the tumor with respect to the treatment beam. [25].

1.2.4 DENSITY VARIATIONS

The densities of the patient geometry are of less concern in conventional photon beam radiation therapy since they have negligible effects on the dose distribution. However, since that the range of ion particles depends strongly on the density of the traversed tissues, the complete knowledge of the density distribution of the patient is necessary for Hadrontherapy. An illustration of the effect of density variations is shown in Figure 1.2.3 where the SOBPs of the proton beam has shifted backward a few millimeters after adding a layer of a material with an increased density. On the other hand, the depth-dose profile of the photons has remained unchanged. Consequently, with breathing, density variations occur and should be estimated to obtain an accurate treatment plan [38][39] preventing severe potential dosimetric consequences. Authors in [40] have studied the effect of breathing motion and systematic setup errors on the cumulative dose of a lung tumor. They have simulated a 50-mm-diameter sphere inside the lung tissue and evaluated the cumulative dose for multiple breathing patterns. They have shown that if the density variations are not considered by the treatment plan, the dose inside the target is reduced from 96 % with no motion to 41% and 65% for a 10 mm breathing amplitude and a 5 mm of setup errors with motion. Additionally, Mori et al. [39] investigated the impact of water equivalent path length (WEPL)¹, the calculation

¹The water equivalent path length (WEPL) is the thickness of a water volume in which the particles lose the same amount of energy as they pass through a given tissue.

of WEPL is density dependent) variations on the range of a charged particle beam using eleven four-dimensional computed tomography images of lung cancer patients. Their results showed that the maximum local range fluctuations vary from 10 to 35 mm for the applied WEPL variations, and furthermore lead to overdosage of organs at risks and/or underdosage inside the target volume as shown in Figure 1.2.4. Hui et al. [41] examined the impact of interfractional changes on the dose distribution inside lung tumors. They have analyzed weekly 4D-CT scans of 8 lung cancer patients. The mean target volume coverage calculated on the weekly data was 1% less than the original plan for all the patients except for one case, where the coverage was 90.9% compared to the planned 99%. This reduction was caused by the large variation between the original simulation 4D-CT image and the weekly 4D-CT image. They have also found a strong correlation between the dose and the changes in density and they concluded that if the target motion is considered in the treatment plan, the target volume coverage will receive an adequate dose for most lung cancer cases. Finally, even though the variation in the density of the tissues is taken into account, the current treatment plans still rest on the experience and the skill level of the clinical practitioner. Therefore, adaptive 4D treatment methods are needed to reduce the dose in surrounding tissues.

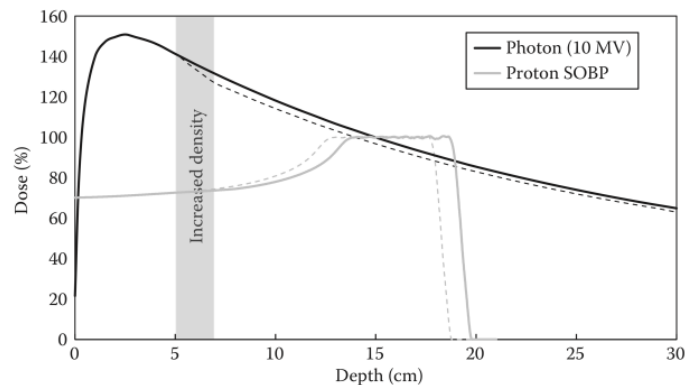


Figure 1.2.3: Impact of density on the beam range. Depth-dose profiles of a photon beam and a proton SOBP, dashed lines represent the profile generated after adding a higher density material (gray rectangle from 5 to 7 cm) in the trajectory of the used beams. [25].

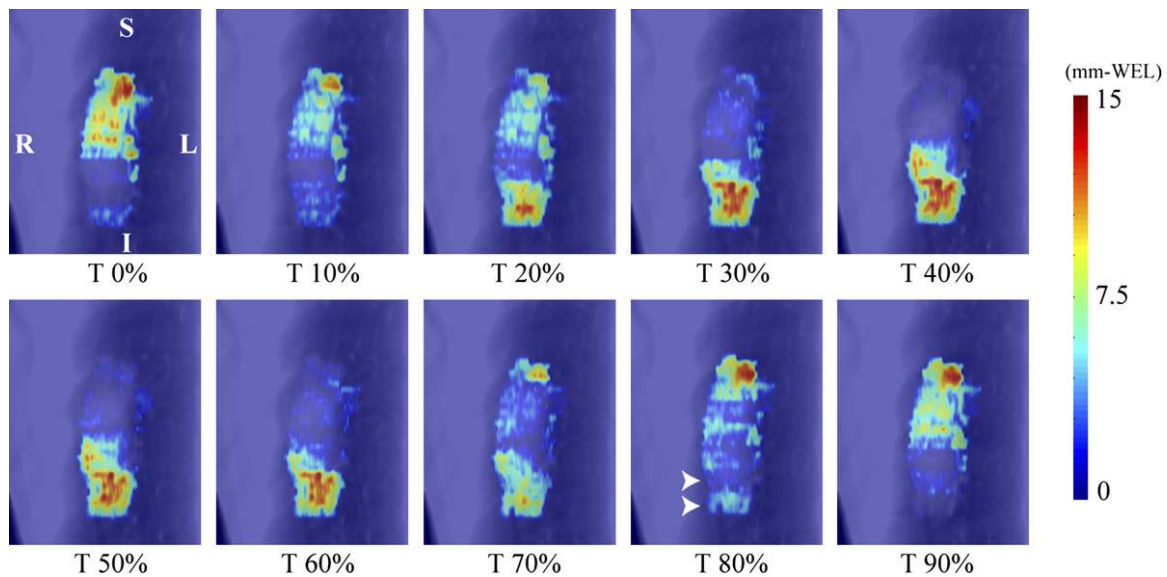


Figure 1.2.4: Range fluctuations expressed in water equivalent path length overlapped on the 4D-CT images. Image from [39].

1.3 MEDICAL STRATEGIES TO DEAL WITH MOTION

Various approaches have been defined to mitigate and manage respiratory motion in cancer treatment with hadrontherapy. During the plan design, all the strategies are taken into account even though few of them are employed during the treatment. In the following, we will describe the pros and cons of each method with an emphasis on dose distribution.

1.3.1 MOTION REDUCTION TECHNIQUES

The most radical and intuitive strategy to reduce motion effects is to reduce motion itself. This category of techniques includes abdominal compressing, breath holding, and apnea. Breath-hold [42] requires an active cooperation of the patient and thus by inhaling and maintaining a fixed target position for an extended period of time. The patient is first triggered by an audio or a visual signal, then monitored to guarantee that the position of the tumor is correctly aligned with the planned location to start dose delivery. For abdominal compression (AC), a respiratory belt is used to immobilize the abdominal region. Even though AC has shown its efficiency to reduce the amplitude of respiration [43] [44], it limits considerably the potential directions of the treatment beam dur-

ing the plan design. Rinecker Proton Therapy Center introduced a more sophisticated method that uses the apnea during the treatment to manage the motion [45]. The common drawback of all these methods is that they are unbearable for patients with lung cancer and require an increased clinical workload. Also, they raise the inter-fractional variations in the daily tumor position.

1.3.2 RESCANNING OR REPAINTING

The idea behind this technique is to control the beam delivery with respect to the breathing cycle by exploiting the fact that repeated irradiations lead to statistical dose averaging inside the tumor volume [46][47][48]. Instead of delivering all the prescribed dose at once, multiple scanning is used to smooth the dose distribution. Although this approach produces homogeneous dose distribution and annihilates overdosage and underdosage regions, it expands the planning target volume to consider the movement of the target volume in the different breathing phases.

1.3.3 RESPIRATORY GATING APPROACH

Comparing to other strategies, gating requires a time-resolved monitoring of the breathing cycle [49][50][51]. The irradiation is only triggered when the amplitude of respiration is lower than a predefined threshold. The beam delivery is limited to a specific portion called "gate". In addition, a real-time monitoring system like spirometers [52] or infrared reflectors [53] is required to observe the motion of the patient. Even though the tumor motion could be diminished to less than 10% of free-breathing respiration (generally during full exhale [54])[55], the treatment time using this approach is much longer comparing to a continuous beam delivery. Besides, the residual motion will still cause interplay effects during the treatment session[56].

Expansion of the planned target volume: In current clinical practice, three main volumes of tissue are defined during the treatment plan design to guide the beam delivery. The first is the gross target volume (GTV), which is the position and the extent of the gross tumor. The second volume includes the GTV and an additional margin that take into account disease spread that cannot be entirely imaged, and it is called the clinical target volume (CTV). A third volume named the ITV for Internal Target Volume was added in the ICRU report 62 to take into account the variations in the size and position of the CTV relative to the patient's reference frame (usually defined by the

bony anatomy). Lastly, the planning target volume (PTV) that takes into account the geometrical variations. Moreover, the organs at risk (OAR) must also be contoured and defined (See figure 1.3.1). The intrafraction motion was conventionally addressed by expanding the PTV volume to cover the target motion completely.

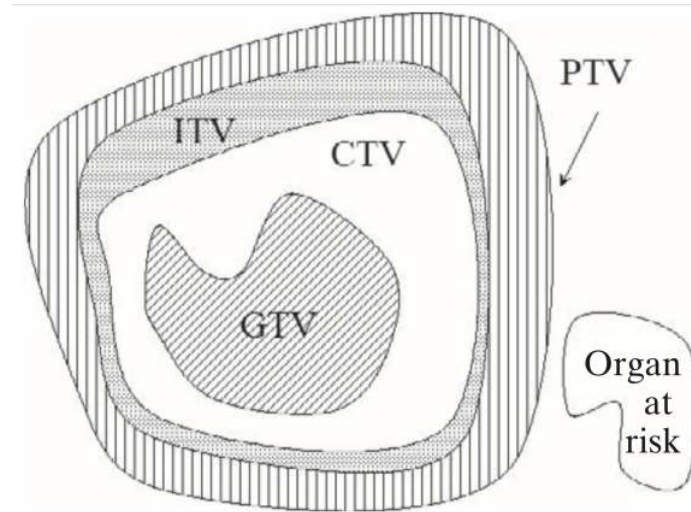


Figure 1.3.1: Graphical representation of the volumes of interest, as defined in ICRU Reports No. 50 and 62.

1.3.4 REAL-TIME TUMOR TRACKING

Tumor tracking is arguably the most advanced and challenging strategy to accommodate the respiratory motion. The beam is shifted dynamically in space to follow the target position in real time during free breathing. Ideally, tumor tracking would exclude the need for adding treatment motion margins while managing a homogeneous dose distribution inside the tumor volume. To follow the target in space this method should know the target position in real time, predict organs motion to give time delays to the beam positioning system and adapt the delivered dose according to lung density and volume variations. This method was first proposed by [57] and then clinically applied for photon therapy, for instance, the Cyberknife treatments applied to x-ray radiosurgery[58]. For radiotherapy, the tracking is a two-dimensional problem that requires the adjustment of the beam to the 2D lateral position of the target. However, for hadrontherapy, the tracking additionally needs

the water-equivalent path length of all the points in the target over time. This approach has only been tested by means of computer simulation investigations [59] [60][61] [62][63] and computational phantom studies [64][65].

1.3.5 ADAPTIVE RADIOTHERAPY

Online adaptive radiotherapy is referred to as the changing of the treatment plan during a treatment session to manage time changes in the patient anatomy such as the weight loss or the internal motion. It could be a good replacement for beam tracking since it addresses efficiently the uncertainties related to the estimation of range using 4D-CT scans, and also the geometrical variations of the patient over the course of a fractionated treatment. Incorporating patient-specific changes of the target surrounding organs can deliver more precise dose distributions by minimizing the volume of margins. Furthermore, it can be employed as a decision protocol that evaluates the used treatment plan and decides if a replanning is needed.

1.4 AIMS AND STRUCTURE OF THE THESIS

The present work is a collaboration project between Saara and CAS-PHABIO teams from Liris (Computer Science Laboratory for Image Processing and Information Systems) and IPNL (The Nuclear Physics Institute from Lyon) laboratories, respectively. The main research field of the Saara team is the biomechanical modeling of the respiratory system [66], [67], [68], [69], [70], [71] and [72]. More recent studies have focused on the correlation of the biomechanical model with external respiratory surrogate signals to track organ motion. In parallel, the collaboration with IPNL is meant to use the biomedical model with a treatment planning system for Hadrontherapy, to calculate dose distributions and to verify the treatment. The broad goal is to have a patient-specific tetrahedral model to use in breathing simulations, treatment planning including dosimetry, and treatment verification. This work doesn't address the movement simulation even if both the biomechanical and image-based movement estimation were used. The general context of this Ph.D. is the treatment of lung cancer using Hadrontherapy.

Independently from the chosen strategy to manage breathing motion, a dedicated treatment plan based on a time-dependent motion model is needed. In Hadrontherapy, to calculate the dose distribution inside the patient, the plan must consider not only the position and shape of the target

but also the density and the chemical composition of the traversed tissues. Since that continuous imaging of the anatomy is still not possible with the state of the art medical technologies, an alternative approach that utilizes a motion model is used by the treatment plan to represent the correspondence between internal variations and respiratory surrogates.

There are two main groups of internal motion estimation methods that are image-based and biomechanical approaches. The first method uses the 4D-CT scan of a single breathing cycle and employs similarity measures between the images to create a displacement map. In biomechanical approaches, the internal displacements and deformations are calculated using the finite element method applied to either voxel-based structures or tetrahedral geometries. Even though the conventional voxel grids are widely used in clinical practice, they suffer from multiple limitations including their poor ability to appropriately estimate the organ density variations during respiration. On the other side, tetrahedral geometries represent the organs using a deformable tetrahedral grid where the movement is defined by vertex displacement. Unlike voxel grids, they have a compact representation of the human body, and they allow for a better description of complex organs with smooth surfaces. As for motion-compensation simulations, these methods have even more advantages considering their ability to appropriately alter organ shape and the fact that they offer more precise tissue tracking. The latter property is guaranteed since every tetrahedron represents a piece of matter that endures deformation during breathing while maintaining its mass and topology.

Apart from geometry features, these models describe also the tissues mass density and the chemical compositions to allow the Monte Carlo code to simulate particle transport through matter as well as energy deposition. Our contribution consists of a 4D dose calculation method using tetrahedral geometries in which we have developed a `geant4` code and an optimization method to improve simulation time. The manuscript is organized as follows: Chapter 2 presents the proof of concept of using tetrahedral geometries for dose calculations in the case of organ motion using an approach based on the principle of mass conservation along with an implementation on the `Geant4` platform. The same tetrahedral structure has been used for both the Monte Carlo simulation and dose accumulation and the dose is calculated on tetrahedral elements. This chapter led to the publication of an article in the international symposium on biomedical imaging conference, titled "Motion-induced Monte Carlo dose calculation using deformable tetrahedral meshes." The methods and results of the article are included in this manuscript along with other details. In chapter 3 we describe our contribution to optimize the geometry and computation time of tetrahedral models

in Monte Carlo simulation using the Geant4 platform. We start by describing the flaws of the current dose calculation methods and then introduce our approach that consists of taking advantage of the accuracy of the water equivalent path length instead of the mass. The work presented in this chapter led to the publication of a Physics in Medicine and Biology peer-reviewed medical journal titled "Particle-beam-dependent optimization for Monte Carlo simulation in hadrontherapy using tetrahedral geometries." Finally, chapter 4 presents the extension of the optimization method to incorporate the movement of organs. We first outline our method for updating the density map of the tetrahedral mesh, then we introduce the strategy for the computation of the reference water equivalent path length.

Ever tried. Ever failed. No matter. Try Again. Fail again. Fail better.

Samuel Beckett

2

Motion-induced Monte Carlo dose calculation using deformable tetrahedral meshes

2.1 INTRODUCTION

In this chapter, we describe our method to calculate the dose in Monte Carlo simulations using deformable tetrahedral meshes. Thus by using a step-by-step approach that first creates a 3D tetrahedral model of the human anatomy, then incorporates the breathing motion into the model. Furthermore, we compute the dose accumulation over time on every tetrahedron to produce a 4D dose map resulting from Monte Carlo simulation. At the end of this chapter, we will discuss the results of our method by using a Geant 4 platform implementation and furthermore study the effect of mesh level of detail on the dose. As a perspective, we will discuss the flows of our approach and offer an improvement for it.

2.2 DOSE CALCULATION METHODS

Having a direct measurement of the spatial distribution of the delivered dose is not yet clinically possible. Therefore, the prediction of dose distribution inside the patient geometry relies on calculation models that simulate the passage of particles through matter. The calculated dose needs to be as accurate as possible to the prescribed dose in order to validate the treatment plan. Moreover, the calculation accuracy determines at what extent the treatment plan reflects the real physical interactions between the beam and the traversed tissues. Furthermore, it might influence treatment strategies concerning treatment margins or beam parameters. Three main dose calculation approaches are used in hadron therapy: pencil beam, ray-casting, and Monte Carlo methods. The first two approaches are analytical methods that use a deterministic algorithm that generates an identical outcome for a given set of input parameters, while the last one is based on a statistical method that generates a large number of random events. In the following, we will describe each method in more detail.

2.2.1 PENCIL BEAM ALGORITHMS

Pencil beam methods (PB) use deterministic but empirical algorithms to model the transport of particles in a medium [73] [74] [75] [76]. They represent the treatment beam with a piecewise physical and geometric approximation such as every pencil beam provides enough accuracy in the calculation of dose deposition in the patient geometry along its path. The final dose distribution is the result of the accumulation of all individual contributions of pencil beams. Pencil beam models take into account the possible degrees of freedom of the radiation field and simulate interactions with the medium using geometry slabs around the pencil beam axis. One of the main limitations of these methods is the fact that they are insensitive to heterogeneities lateral to the bounding envelope of a given pencil beam. Moreover, their accuracy is compromised by the simplifications and assumptions built into them. In 2017, the authors in [77] have concluded that analytical algorithms in proton therapy should not be considered for dose calculation of Lung tumor since they can overestimate the dose to the tumor by up to 46 %. They have also compared PB approach to Monte Carlo based methods using an anthropomorphic phantom, and they showed that MC algorithms produce much better results and are in a better agreement with the real physical measurements.

2.2.2 RAY-CASTING ALGORITHMS

Also known as depth penetration or broad beam methods, ray-casting algorithms (RC) [78] [79] [80] [81] are very similar to pencil beam methods. Instead of using physical pencil beams, they subdivide the treatment beam into rays, and they track them along straight lines through the patient geometry to calculate the dose contribution only on the points belonging to their path. The dose value of a given point $P(x, y, z)$ in a ray parallel to the z -axis is defined as follow:

$$D(P) = W \times I_{IDD}(E, WEPL(P)) \times K(x - x_o, y - y_o, \sigma)$$

Where W is the number of particles (or weight), I_{IDD} is the integral dose and K is the kernel which is a 2D function containing the lateral beam model. E is the energy and σ is the width of the beam and it contains the contribution from the initial beam shape. Finally, the $WEPL(P)$ is the water equivalent path length along the ray intercepting the point P and it is defined in [82] as : $WEPL(P) = t_w = t_m \frac{\rho_m \overline{S_m}}{\rho_w \overline{S_w}}$, where t_w and t_m are the thicknesses of water and the target material, respectively. ρ_w and ρ_m are the mass densities of water and the material, respectively. Finally, $\overline{S_w}$ and $\overline{S_m}$ are the mean values of mass stopping power for water and the material, respectively. Since that the calculation of the dose in a given point depends only on the ray passing through that point, the time needed to simulate the particle transport is much less than the time required in PB algorithms. Hence, ray casting approaches are suitable for applications that demand short calculation times like treatment plan optimization even though they are less accurate than PB.

2.2.3 MONTE CARLO METHODS

Monte Carlo methods (MC) [83] [84] are considered the most accurate dose calculation methods since they model explicitly each particle interaction in the patient. Nevertheless, to reach a high level of accuracy and to obtain low statistical uncertainty, more particle events need to be simulated. In a Monte Carlo approach, the final dose distribution is obtained by calculating the contribution of all individual particles. However, prior to that, the simulation starts with randomly generating a number of events from a set of possible combinations given by the beam phase space which contains information about the beam shape, divergence, particle composition, and energy distribution. Furthermore, the simulation of the passage of particles in the patient geometry is triggered starting from the particle source. The algorithm processes the particles one after the other

and calculates their trajectories in a step-by-step fashion. A random sampling from one or several probability distributions is used to define the behavior of a particle in a given step and decide if it will be annihilated, change direction, absorbed, or change energy and thus by using theoretical physical models and experimental cross-section data. Additionally, the energy deposited in the detectors is recorded, and then both the primary particle and the resulting particles (i.e., secondary particles) continue to be traced in the same way. This process is called tracking, and it operates on the tracking geometries that could be the patient geometry or the beamline equipment. Finally, the result of the entire process is a statistical dose distribution with a precision defined by the number of simulated particles. Unlike analytical methods, Monte Carlo simulations don't only take into account the tracking geometries but also tissue inhomogeneities along the treatment beam by incorporating the materials and their physical properties, like the chemical composition, mass and electron densities and the mean excitation energy. They even simulate secondary particles production. These reasons make this method the gold standard for conventional radiotherapy and hadrontherapy since it converges the best to the real dose map. Nonetheless, the main limitation of MC methods is the time required to simulate and track particles, which can restrict their use in routine treatment planning [85]. The time and the number of particles in a given simulation are determined by the desired accuracy of the dose distribution which depends on the level of statistical uncertainty, the chosen step size, the spatial resolution of the dose grid and also on the number of physics interactions that the particle undergoes during the tracking. The adopted step size needs to be small to ensure that the difference of the cross sections at the extremities of the step is small. A larger step size could be used to reduce calculation time at the expense of the simulation precision in regions with low interest. Moreover, Monte Carlo codes usually apply different methods to guarantee suitable step sizes especially in regions close to boundaries where a variation in the material is encountered. In the last decades, the interest in using Monte Carlo methods in hadrontherapy has increased with the high-performance machines and parallel computing capabilities. To design and execute a Monte Carlo simulation in Hadrontherapy, multiple software solutions exist, for example: FLUKA [86] [87], Geant4 [88][89], MCNPX [90] [91], VMCpro [92], Shield-Hit [93]. Generally, the user provides an input file that contains the simulation settings and parameters including the beam energy, the geometry assembly and the physical processes to use. As a result, the MC code generates typically information about the tracked particles in every step in a form of histograms. The level of control during the tracking differs from a MC code to another depending

on the interface provided to the user. In the case of Geant4, every parameter (e.g., step sizes, and material constants) can be adjusted and modified since the code has the form of oriented-object toolkit libraries in which the processes are organized using a C++ class structure. In this work, we will use Geant4 for its flexibility and its ability to incorporate new modules in its code. Finally, it gives control to the lowest level of physical interactions.

2.3 RESPIRATORY MOTION ESTIMATION

The treatment plan procedure must track the continuous changes in the patient's anatomy over time to ensure the delivering of the planned dose to the target during breathing. The tracking includes not only geometrical transformations but also the physiological changes of the tissues, as the range of ion beams depends on the density and the chemical composition of the traversed tissues. Since the clinical and direct measurement of organs' deformation is, at least currently, not possible as explained in the previous chapter, two main strategies have been defined to provide an estimation of the deformation between different breathing cycles: image registration and biophysical modeling. For both methods, the final aim is the calculation of a deformation vector field (DVF) that represents the transformation that the geometry undergoes to go from a breathing phase to another. Image registration use similarity measures between 3D frames of the 4D images based on the intensity values or features like closed-boundary regions and edges. On the other side, biophysical (or biomechanical) modeling rely not only on the images but also on the breathing physiology and physical properties of organs. The two methods will be briefly described in the following sections.

2.3.1 IMAGE-BASED MOTION ESTIMATION APPROACHES

These methods are widely used in modern medical imaging to determine the spatial correlation between different image acquisitions, and they consist of the so-called Deformable Image Registration techniques (DIR). These techniques estimate the motion vector field between two images by optimizing similarity measures of individual voxel intensities. The first image is referred to the moving or the source image and the second one is called the fixed or the target image. Furthermore, the optimal transformation is achieved by means of an energy minimization problem applied to the two images and defined in [94] as follows:

$$\arg \min_{\theta} \mathcal{A}(F, M \circ \mathcal{T}(\theta)) + \mathcal{R}(\mathcal{T}(\theta))$$

Where \mathcal{A} is the first term of the energy and it represents the level of alignment between the fixed image F and the moving image M using a transformation \mathcal{T} characterized by the parameter θ . Furthermore, the term \mathcal{R} regularizes the transformation \mathcal{T} and can be used to privilege deformations that are consistent with the patient's anatomy. In the case of breathing motion, DIR creates a voxel-to-voxel displacement map that associates to every voxel from a reference breathing phase its corresponding voxel in any other phase. More exhaustive reviews can be found in [95][96][97][98][94][99][100]. Since that the clinical patient deformation is hard to predict, the validation of any deformable image registration method is challenging. In fact, the three main methods used to verify and validate the resulted deformation vector fields (DVF) are respectively based on : anatomical landmarks [101][102], anthropomorphic phantoms [103][104], and mathematical phantoms [105][106]. Brock et al have conducted a study on the performance of a set of DIR algorithms in [107] and they concluded that the registration accuracy of the bulk of these algorithms is near the voxel size if a good image contrast is available.

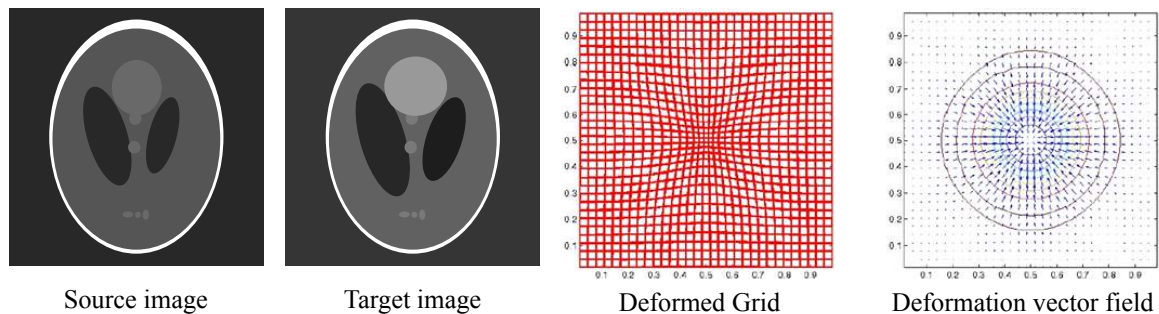


Figure 2.3.1: The result of a deformable image registration algorithm applied on a phantom. The deformed grid represents the transformed pixels of the source image using the deformed vector field (DVF).

Moreover, DIR algorithms are not only used for motion estimation, but also in the treatment planning stage for dose accumulation as will be discussed in the following sections. Additionally, the resulted deformation field is used to deform the organs during the particle-matter interaction. Finally, it is worth mentioning that the registration uncertainties have direct consequences on further treatment planning stages as dose calculation and accumulation.

2.3.2 BIOMECHANICAL METHODS

Unlike DIR-based approaches that only take advantage of the 4D sequences of images, the biomechanical or biophysical models benefit additionally from the physical properties of organ's tissues and their breathing physiology to estimate the internal deformation during respiration. They are often associated with Finite Element Methods (FEM) since FEMs are used to solve the partial differential equations of the mathematical formulation of the modeling process. More precisely, biomechanical models use continuum mechanics and the mechanical properties of the respiratory system such as the tissue's elasticity, to model the organ motion. Moreover, the patient's organs are extracted from corresponding images and modeled using a discretization process that generates a mesh of small elements called finite elements. Furthermore, the displacement of each node is calculated by applying the forces engaged in the respiration process. Biomechanical modeling could also be used as an additional constraint for image registration to enhance the quality and the robustness of the field estimation. Even though biomechanical modeling of respiration dynamics has been addressed by [108][109] in the early 1970s, it has gained particular attention from researchers over the last two decades, especially for radiation therapy application.

Villard et al. have simulated the pulmonary ventilation using a 3D idealized deformable model of the respiratory system calculated with the finite element method [66]. They have extracted surface displacements using external thoracic movement alongside airflow and abdomen external motion. [110], [111] later adopted a similar approach in which they have developed a patient-specific model from 4D computed tomography data. The interactions between the lung surface and the chest cavity were taken into account by applying pressure forces to the 3D mesh surfaces that represent the geometry. In these works, negative pressure was used on the lung surface to mimic the physiology of the respiratory system and to trigger the deformation of the lungs. Additionally, the increasing volume of the lungs is bounded by either the final intended lung shape generated in the maximum inhalation or the surface of the chest cavity to ensure realistic outcomes. Furthermore, AL-Mayah et al. have conducted a series of studies that address the simulation of lung ventilation mechanism in [112] [113] [114]. They have created a biomechanical model containing a small lung tumor, and instead of utilizing the pressure to simulate the deformation, they have employed the geometrical differences between inhale and exhale as boundary conditions. Later in [115], Karami et al. have developed an in vivo patient-specific lung model with variable tissue incom-

pressibility and thoracic pressure to obtain more accurate deformation. However, even though the lung model was calculated with FEM, the diaphragm's motion was generated using image registration. Additionally, tissue deformation was only considered for the lung's base, and the respiratory system hysteresis was neglected. A more realistic patient-specific biomechanical model based on the diaphragm's behavior as well as rib kinematics has been introduced by Didier et al. [67], and further improved by Ladjal et al. and Giroux et al. in [116] [117] [118] [72]. Interestingly, the model can also be guided by external respiratory surrogate signals generated using spirometer and/or abdomen surface. The whole geometry of the thorax was modeled including lungs, tumor, rib cage, diaphragm, mediastinum, and the spine. Finally, the effectiveness of the model was validated using a comparison study between the FEM simulations and the 4D image sequences. Furthermore, to simulate the complete respiratory cycle, the authors in [118] have used not only a patient-specific patient geometry but also a personalized physiological compliance (pressure-volume curves) to define lung pressure and the parameters of diaphragm's forces (see figure 2.3.2).

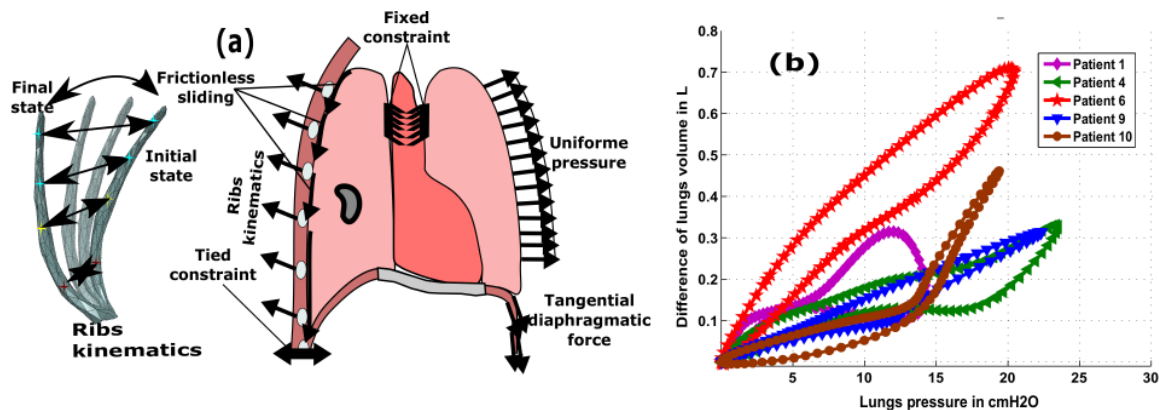


Figure 2.3.2: (a) Biomechanical model of the thorax including lungs, rib cage, and diaphragm. (b) Physiological compliance calculated for lung for five patients. Image taken from [118].

2.4 MODELING OF MOVING ORGANS IN HADRONTHERAPY

To simulate particle-matter interactions in Monte Carlo simulations, both the treatment beam line equipment and the patient's geometry need to be modeled. The patient's geometry is represented

by what is called computational phantoms. Human computational phantoms are widely used for multiple areas of medical research, particularly for radiation dosimetry. They represent the anatomical features of the human body and define the geometry of organs in which radiation interactions are to be calculated. Besides the geometry definition, a computational phantom describes the tissues mass density and the chemical compositions in order to allow the Monte Carlo code to simulate particle transport through matter as well as the energy deposition. Three major families of phantom exist Voxel-based, surface and tetrahedral models. The focus of this study will be on tetrahedral geometries.

Radiation therapy aims at delivering a lethal dose of ionizing radiation to tumor tissues while sparing the surrounding tissues from the adverse effects of radiation. However, ensuring a homogeneous dose inside the tumor in lung cancer is challenging, since that the respiratory motion during irradiation reduces the target coverage and increases dose deposition within healthy tissues. To calculate and to ensure sufficient dose coverage throughout the treatment, a first margin is added to the gross tumor volume (GTV) to compensate the movement, this is known as the clinical target volume (CTV). Additionally, a planning target volume (PTV) is also defined to allow for planning uncertainties in the treatment. The addition of these margins leads to an excessively large PTVs that would go beyond the patient's dose tolerance and does not reflect the actual clinical consequences. Moreover, in the case of Hadrontherapy, apart from the ballistic problem caused by the target movement and deformation, the organs density variations also affect the particle range which can lead to unwanted dose distributions. Current 4D-dose-calculation techniques based on voxel-based structures and deformable image registration (DIR) [119][120][121][122][123] can not adequately take into account the organ density variations during respiration because they don't rely on the anatomy and the physiology of the respiratory system. Besides, the anatomical fidelity of voxel phantoms depends strongly on voxel size especially for thin tissues like ribs and bone marrow. They also have stair-stepped surfaces that can provoke additional uncertainties in some dose calculation scenarios [124]. Often, these methods are accomplished by optimizing similarity measures between image sequences which make it difficult to simulate advanced interactions between organs like lung sliding. Most of all, these approaches are not suitable for organs such as lungs that undergo large deformations.

The limitations of voxel-based phantoms have pushed many authors to develop deformed surface-based computation anthropomorphic phantoms [125][126][127][128][129][130][131][132]

[133][134][135]. They offer an accurate organ representation with smooth surfaces that can also model thin and complex geometries. At the same time, they have shown high capabilities in deformable anatomy and respiratory motion simulations. However, since that these models have been developed initially for medical imaging, they suffer in Monte Carlo particle transport simulations, considering that they can not represent the spatial density map of heterogeneous mediums like the patient tissues. Moreover, the Monte Carlo simulation time needed for the surface-based models is much slower than the corresponding voxel-based structures.

To overcome these problems, alternative methods based on tetrahedral geometries have arisen, in which the internal motion is described using either Biomechanical models based on finite element method or DIR. As opposed to the conventional-voxel-based representation, organs are represented by a deformable tetrahedral grid where the movement is defined by vertex displacements. Tetrahedral-based methods are increasingly used in medical research due to their compact representation of the human body and their better description of complex organs with smooth surfaces. As for motion compensation simulations, these methods have even more advantages considering their ability to appropriately alter organ shape and the fact that they offer a more precise tissue tracking. The latter property is guaranteed since every tetrahedron represents a piece of matter that endures deformation during breathing while maintaining its mass and topology. Apart from geometry features, these models describe also the tissues mass density and the chemical compositions to allow the Monte Carlo code to simulate particle transport through matter as well as energy deposition.

Tetrahedral geometries were investigated by several authors for Monte Carlo particle transport simulation to demonstrate their computational efficiency compared to surface-based models [136][137], [138], [139], [140]. Authors in [141] and [142] have used the tetrahedral mesh generated from a closed tessellated surface as an acceleration structure for navigation in Geant4 Monte Carlo code [143][144]. They demonstrated that the navigation time is reduced by two orders of magnitude since that the computations are performed only on local tetrahedra rather than the entire tessellated surface. However, even if the Monte Carlo simulation time is improved, the geometry load time of the tetrahedral mesh is twice the time needed for loading the equivalent tessellated solid. The same approach was used by [145] to simplify the geometry of a polygonal computational human phantom named PSRK-Man [146] to create the equivalent tetrahedral-based phantom. This geometry was also exploited to represent the density variation inside organs, which is considered

one of the limitations of tessellated solids.

To incorporate the movement in tetrahedral geometries, some authors have developed other approaches to compute four-dimensional dose distributions for Hadrontherapy. [147] have proposed a model for liver cancer treatment. They create two voxel-based density maps at the extreme phases of the breathing cycle that are used in dose calculations. Then, the dose value for each tetrahedron is approximated as the dose deposited in the voxel closest to the centroid of the tetrahedron. The model of [148] is based on mass-spring models where each tetrahedron has its specific density value. This value is obtained by taking the density value of the voxel containing the centroid of the tetrahedron. This method will be referred to as the centroid mapping (CM) in the rest of the document. Afterwards, the meshes are voxelized to perform dose calculations then the 3D dose distribution for each phase is remapped to the reference phase. Furthermore, authors in [149] have created a tetrahedral mesh for 4D Monte Carlo dose calculations by integrating organs movement issued from deformable image registration (DIR). Their results show that 4D tetrahedral geometries give accurate dose distributions. Nevertheless, they haven't detailed the method used for density mapping and tissues definition. Manescu et al. [150] [151] have developed a more sophisticated model coupled with a biomechanical model of the liver, that uses a continuous density function inside the mesh. Thus by mapping the densities issued from CT-images to the nodes of the tetrahedral mesh instead of its elements. This has the advantage of having a different density value for each point inside the mesh and more importantly preserving the mass of tissues since it respects the mass conservation principle. However, the accuracy of their algorithm depends strongly on the density heterogeneity of the mapped tissues and also to the number of tetrahedra representing the mesh. This method is known as the Continuous mass conserving mapping (CMCM). For particle transport simulation, they had voxelized the mesh and calculated a 3D dose map for every breathing phase. Moreover, these resulting maps were remapped back on the tetrahedral-based model for dose accumulation. The CMCM method will be further detailed in the next section.

Furthermore, to avoid the generation of intermediate voxel-based densities, we have implemented in [152] a 4D tetrahedral model on Geant4 to be able to perform simulations directly on the mesh. We have employed a lung geometry to evaluate the dose distribution in motion-compensated Monte Carlo simulation. Thus, using the movement generated using deformable image registration algorithm (DIR) applied to the 4D CT scans. Finally, we compared it to the corresponding voxel-based

model. We demonstrated that the two 4D dose distributions are quite similar and that the tetrahedral model gives promising results for dose calculations. We have nevertheless used a very refined model to describe the organs which engendered a high-cost computation time. As for the density mapping, they have defined the density of a tetrahedron as the mean density of the density values on the vertices. Our method will be referred to as the Mass conserving mapping (MCM).

2.5 CONTINUOUS REPRESENTATION OF MOVING ORGANS

Petru et al. In ([150][151], [71]) have adopted another approach based on tetrahedral geometries to model not only the human anatomy, but also the organs deformation during breathing. This new method usually used in biomechanical modelling, takes advantage of the geometrical and topological properties of tetrahedrons to address the problem of deformation and movement. They have proposed a continuous representation of the human body where each organ is described with a deformable tetrahedral mesh. Additionally, the values of interest of the physical quantities of the medium inside the mesh are mapped onto the vertices of tetrahedrons. This approach is inspired from finite element methods and it ensures the continuity of the represented quantities such as mass density or dose. Contrarily to the voxel representations where only one discrete value represents the physical quantity of the medium inside a given tetrahedron, in this method, the physical point inside a tetrahedral element depends on its relative position inside its enclosing tetrahedron. Hence, they have first distributed the physical quantity to the vertices of the tetrahedral mesh then they have used a linear interpolation to calculate the physical value. As a result, they could calculate a unique value of each physical point inside the domain of the modeled tissues. The novelty of this method resides in using a unique model to represent multiple physical quantities like density or dose.

The choice of the tetrahedron over the voxel as the basic element for the modeling of both the human body and the movement simulations was backed by several advantages. First, for geometrical reasons since that tetrahedral meshes provide a better description of complex volumes and allow for smooth surfaces that are well suited for internal organs. Moreover, the triangular surfaces can be quickly and easily tetrahedralized to create a volumetric representation of the organs. Additionally, the tetrahedron is considered a 3D-simplex which is an element that can be used to build any other 3D shape including prisms, pyramids or even hexahedra. Another benefit of using a tetrahedron is

its ability to maintain its topology during deformation since that whatever the transformation that its vertices undergo it will remain a tetrahedron. While, a deformed hexahedron can become a dodecahedron if it's subject to large deformations. Additionally, tetrahedral meshes allow for precise tissue tracking during motion compensation simulations since each element represent a piece of matter that preserves its mass and topology during breathing. Finally, they offer a good structure for energy and dose accumulation.

Dose calculation simulations require a detail description of the human anatomy to estimate the energy deposition along the traversed tissues, therefore, creating a model that represents the density of the medium and its chemical composition is essential, especially in Monte Carlo simulations. To this end, the authors in [150] have introduced a new approach that maps the density information issued from 3D CT images to the corresponding deformable tetrahedral mesh. This method is based on the principle of mass conservation and it correlates the geometrical deformations of the mesh with the density variation during respiration.

Since that this method represents the foundation and the starting point of our work, we will introduce it in detail in the following section. But before that, we will lay the groundwork by defining the mathematical notations to be used in the rest of the document. Thus, by describing the tetrahedral elements and the distribution of the physical quantities on the mesh. It is worth mentioning that this method is intended to map any physical quantity in a tetrahedral mesh, but it will be only discussed for mass density mapping.

Two structures will be used to represent the volume of the human body, the voxel-based and tetrahedral-based structures. The former represents the CT-scans and it is required since it is the source for HU numbers and density values. It will be denoted as \mathcal{V} and V_i represents a given voxel i . Finally, n_V will represent the number of voxels in the image. A tetrahedral mesh representing the same volume will be denoted by \mathcal{T} and it is defined as a set of tetrahedral elements T_j with n_T the number of tetrahedrons and n_{VER} the number of vertices. Furthermore, we define every tetrahedron T_j by its four vertices VER_1^j , VER_2^j , VER_3^j , and VER_4^j as illustrated in figure 2.5.1.

Since that the vertex is relative to the tetrahedral element, a shared node is denoted differently according to the referred tetrahedron. For example the nodes VER_2^j and VER_1^{j+1} referred to the same vertex. Furthermore, to incorporate the movement and the deformation of the organs, a displacement vector is specified for each vertex as shown in figure 2.5.2. A given vector represents the node displacement from a time step t (E.g. a breathing phase) to another step $t + 1$ and it is

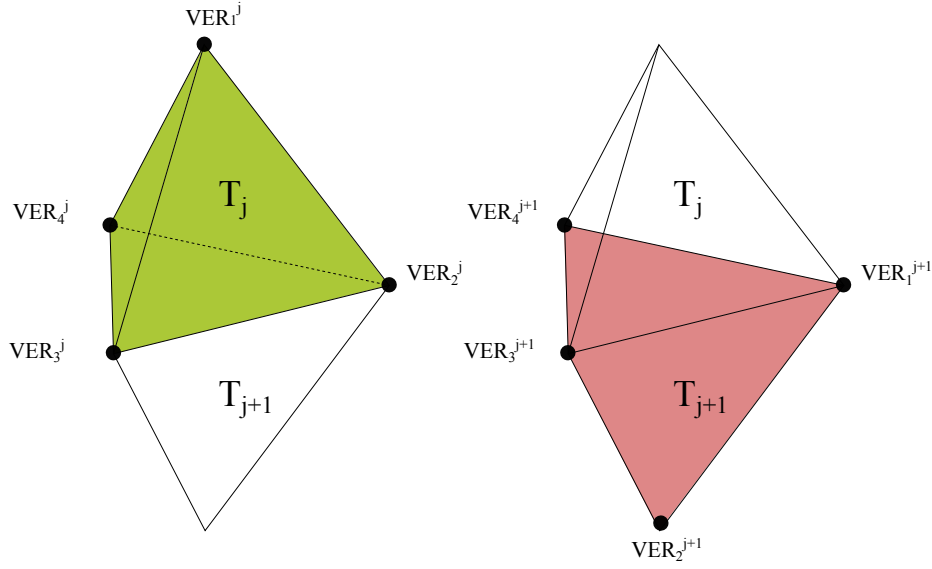


Figure 2.5.1: Notation used for tetrahedrons. T_j and T_{j+1} are two adjacent tetrahedrons.

denoted by:

$\Delta U_{VER_i^j}^{T_j}(t \rightarrow t+1)$. Thus, during simulation, the position of the vertex is updated as follow:

$$VER_i^j(t+1) = VER_i^j(t) + \Delta U_{VER_i^j}^{T_j}(t \rightarrow t+1).$$

As explained earlier, image-based models describe the patient anatomy as a set of 3D images taken at different time intervals. These images are related to one another using a vector field containing the relative displacement of each voxel. Additionally, the physical value of interest is the same for all the points inside a voxel. To distribute a given information function F on the vertices of a tetrahedral mesh, Petru et al. assumed that it varies linearly within a tetrahedron and they defined the density information function as follow: $f = \frac{dF}{dV}$. This function estimates the physical value of a given point inside the tetrahedral element by using the values calculated on the vertices.

$$f_j : \left\{ \begin{array}{l} T_j \longrightarrow \mathbb{R}_+ \\ p = \sum_{l=1}^4 \lambda_l^j \cdot VER_l^j \longrightarrow f_j(p) = \sum_{l=1}^4 \lambda_l^j f_l^j \end{array} \right. \quad (2.1)$$

Where $f_l^j = f^j(VER_l^j)$ and λ_l^j with $l \in \{1, 2, 3, 4\}$ are the barycentric coordinates of the point p

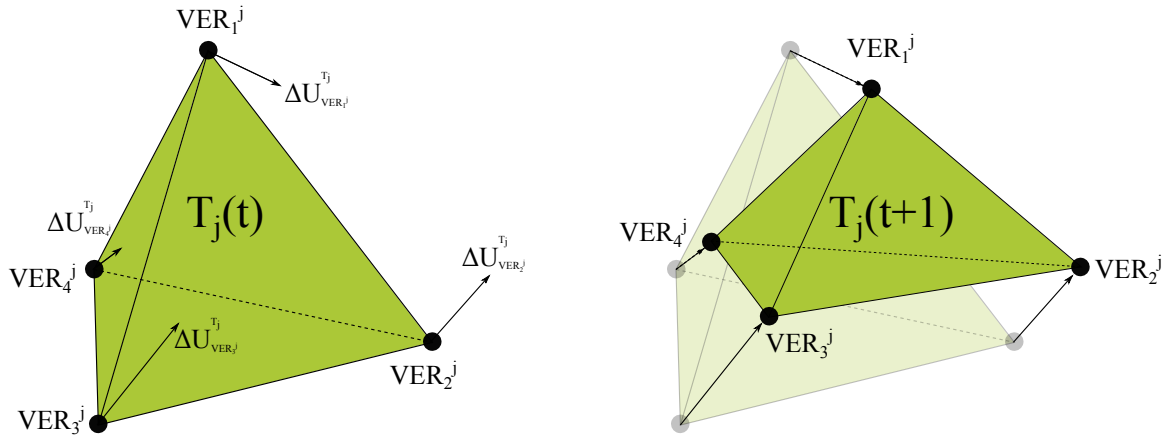


Figure 2.5.2: Tetrahedral mesh deformation from the time step t to $t + 1$. Deforming the tetrahedron T_j using vertex displacement.

inside the tetrahedron T_j . Furthermore, the integral of the function f over the tetrahedral element can be approximated linearly by:

$$F_j = F(T_j) = \int_{p \in T_j} f_j(p) dp \simeq \frac{\text{Vol}(T_j)}{4} \sum_{l=1}^4 f_l^j \quad (2.2)$$

The proof of the equation 2.2 is detailed in Appendix A.

The next step consists of defining the value of the density function of all the nodes of the tetrahedral mesh. To achieve that, the equation 2.2 is written for all the tetrahedrons T_j of the mesh, which leads to a linear system with n_T equations and n_{VER} unknowns. The system is written as follows:

$$\begin{cases} A \cdot x & = F \\ A & = \frac{1}{4} \cdot \Omega \cdot M \end{cases} \quad (2.3)$$

With x the vector of the values of the mesh nodes and F the integrated values inside a tetrahedron. The vector F contains all the elements of the mesh F_j with $j = 1, \dots, n_T$. Additionally, the matrix Ω is defined as follows:

$$\Omega = \begin{bmatrix} Vol(T_1) & 0 & \cdots & 0 \\ 0 & Vol(T_2) & \cdots & 0 \\ \vdots & \vdots & \ddots & \vdots \\ 0 & 0 & \cdots & Vol(T_{n_T}) \end{bmatrix}$$

The matrix M is a $n_T \times n_{VER}$ sparse matrix that indicates if a given node i belongs or not to the tetrahedron T_j by putting 1 in $M_{i,j}$ or 0 otherwise. Since that there are more elements in a tetrahedral mesh than vertices due to the fact that a given vertex can be shared by multiple tetrahedrons, the final system in equation 2.3 is overdetermined and can be solved using a least-square method. Finally, the solution will ensure the continuity of the information throughout the entire mesh as well as the information inside the elements.

In the case of the density map needed by the Monte Carlo code to perform dose calculation, the density values defined on the tetrahedral mesh are calculated using a method defined in [150]. For this approach, the CT-image is used as the source of density information and then, the values are mapped to the tetrahedral. Once the density information is defined on the tetrahedral mesh, the next step is to compute the density variation during deformation, for all the breathing phases. To address this challenge, Petru et al. in [71] have classified the organs tissues into three different types: Constant volume tissues, variable volume and variable mass volumes tissues. The aim is to update the information of density on the vertices. The first category contains tissues with a high density like bone. Since it is very hard to change their volume even with considerable forces, the node density values belonging to tetrahedrons of bone structures remain unchangeable. For variable volume tissues such as soft or fat tissues, the density on the nodes needs to be recalculated. In this case, the principle of mass conservation is used to preserve the mass of each tetrahedron after deformation:

$$\sum_{l=1}^4 \rho_l^j(t_{i+1}) = \frac{vol(T_j)(t_i)}{vol(T_j)(t_{i+1})} \sum_{l=1}^4 \rho_l^j(t_i) \quad (2.4)$$

Writing this equation for all the nodes and solving the resulting linear system gives the new values of density.

The last category of tissues corresponds to internal volumes that show a mass change between two temporal frames such as the bladder or the in our case the lungs that change their mass while

filled with air. Therefore the mass becomes:

$$m(T_j)(t_{i+1}) = m(T_j)(t_i) + \Delta m_j^{air}(t_i \rightarrow t_{i+1}) \quad (2.5)$$

Where $\Delta m_j^{air}(t_i \rightarrow t_{i+1})$ is the mass of air inhaled per tetrahedron between t_i and t_{i+1} .

2.5.1 RESULTS

Although the continuous representation showed interesting results in [151] and [71], it has some weaknesses related to its continuous nature. This is manifested by a poor outcome in discontinuous mediums which can be solved by creating sub-regions. Another drawback is related to the time needed to update the information on the vertices of the mesh since that for every breathing phase the continuous function has to be recalculated to cope to the deformation of the mesh. Additionally, the tetrahedral mesh has to be voxelized before Monte Carlo simulations since the MC software packages don't support the aspect of continuous density, and they only require a single density value for every tetrahedron element.

To address these problems, we have defined a discrete version of the continuous representation, that considers a unique value of density per tetrahedron and calculates it using the densities on the vertices of the tetrahedral mesh. In the following, we will describe our method named MCM for mass conservation method by first describing the process of density mapping. Then, we will show the dose accumulation process, and we finish by describing the Geant4 implementation and evaluating it using spheric and patient cases.

2.6 TETRAHEDRAL MESH CREATION AND DENSITY MAPPING: FROM VOXEL-BASED GEOMETRIES TO TETRAHEDRAL MODELS

This section describes the methodology of using deformable tetrahedral meshes in Monte Carlo simulations. We start by describing how to create a tetrahedral material density map starting from a CT image. Next the dose accumulation process is described, and the section ends with an example of implementation based on the GEANT4 toolkit.

2.6.1 MAPPING VOXEL DENSITIES INTO TETRAHEDRAL ELEMENTS

The primary source of patient data for the present work is CT scan data, as they contain information related to the material densities needed for simulating particle-matter interactions. A CT image is a voxel map of linear X-ray attenuation coefficients of the different tissues to be visualized. The voxel values are scaled such that the linear X-ray attenuation coefficient of air equals -1000 and that of water equals zero. This scale is the Hounsfield scale with the unit HU. *Schneider et al.* present a method to convert Hounsfield values into tissue parameters (mass density and chemical composition) needed for dose calculations [153]. Figure 2.6.1 depicts the flowchart of a three-dimensional tetrahedral density map creation.

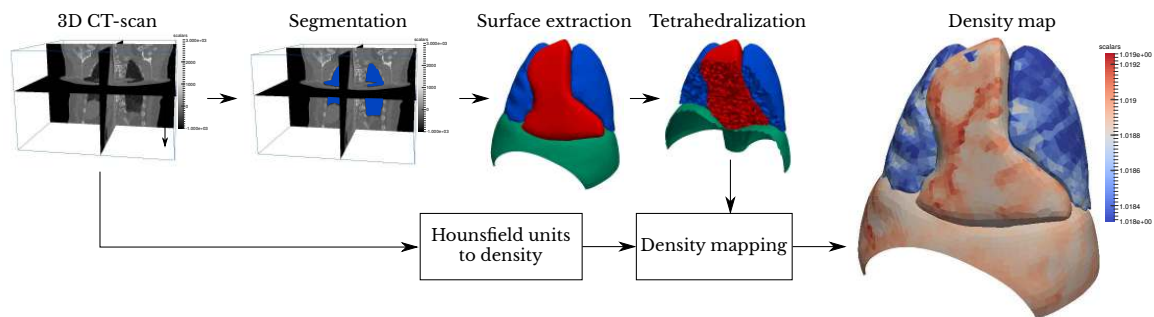


Figure 2.6.1: Flowchart of tetrahedral model construction: from 3D-CT to tetrahedral density map. Each organ is described by a tetrahedral mesh obtained from 3D CT images. The CT images are first converted into voxelized mass density maps which are then mapped to the tetrahedral elements of the meshes.

Tetrahedral mesh generation: The first step in generating tetrahedral models is the processing of CT data. In this context, images are at first preprocessed by thresholding the image intensities. Next, the organs of interest are segmented using the *snake evolution* method [154] based on active contours. Besides, triangular surface meshes corresponding to the organs are extracted using the *marching cubes* technique [155]. Given that the resulting meshes are very dense, we used the ReMESH software to simplify these surface meshes [156]. Further on, these meshes are converted into tetrahedral meshes suited for finite element analysis applying the tetrahedralization algorithm based on the Delaunay technique [157]. For this, we used both the Abaqus FE software developed by Dassault System as well as the Tetgen software [158].

Density mapping: The density mapping process aims at defining the density distribution of the mediums simulated by the Monte Carlo code. Thus, by mapping the densities from CT-images to the tetrahedral meshes. We define the Mass Conservation Mapping method (MCM) as the discrete version of the Continuous Mass Conservation Mapping (CMCM) method proposed by [150][152] and described in the previous section (section 2.5). In CMCM a continuous density function is defined inside the domain of the mesh by calculating the density values of the vertices. These values are further used in MCM to calculate a single density value for each tetrahedron by taking the mean of the densities of the vertices (see figure. 2.6.2).

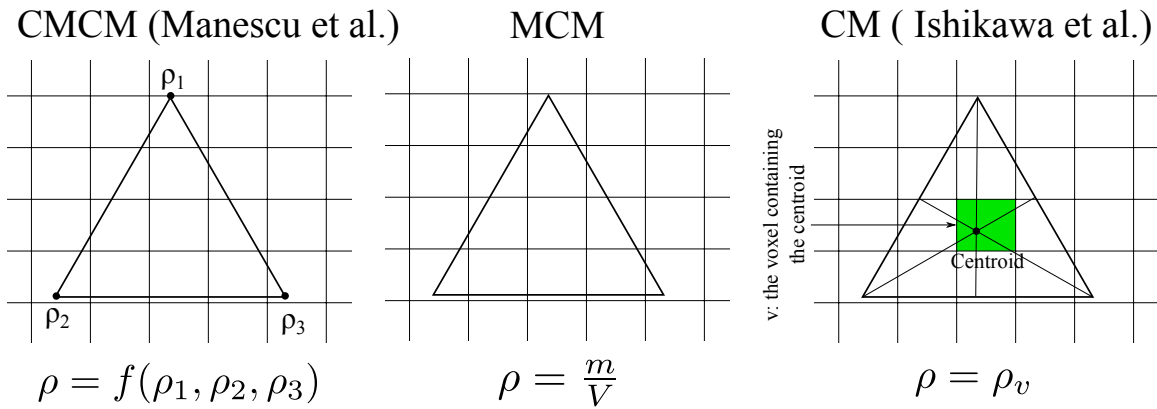


Figure 2.6.2: Density mapping methods, f is a linear interpolation function. Left: Continuous Mass Conservation Mapping (CMCM). Center: Mass Conservation Mapping (MCM). Right: Centroid Mapping (CM).

A second approach to calculate the mean density in MCM is to calculate the total mass of the parts of voxels that superimpose the tetrahedral element then deduce the density value using the volume respecting the principle of mass conservation. The mass of each tetrahedron is computed by intersecting the tetrahedral mesh with the voxel grid. The mass of a tetrahedral element can be expressed as the sum of the volumes of intersection between the tetrahedron and the grid of voxels. Let $J_k = \{j, I_k^j \neq \emptyset\}$ where $I_k^j = V_j \cap T_k$ represent the intersection volume between the voxel V_j and the tetrahedron T_k . Then:

$$m(T_k) = \sum_{j \in J_k} m(I_k^j) \quad (2.6)$$

Figure 2.6.3 shows a 2D example of calculating the mass of a mesh element as the sum of the

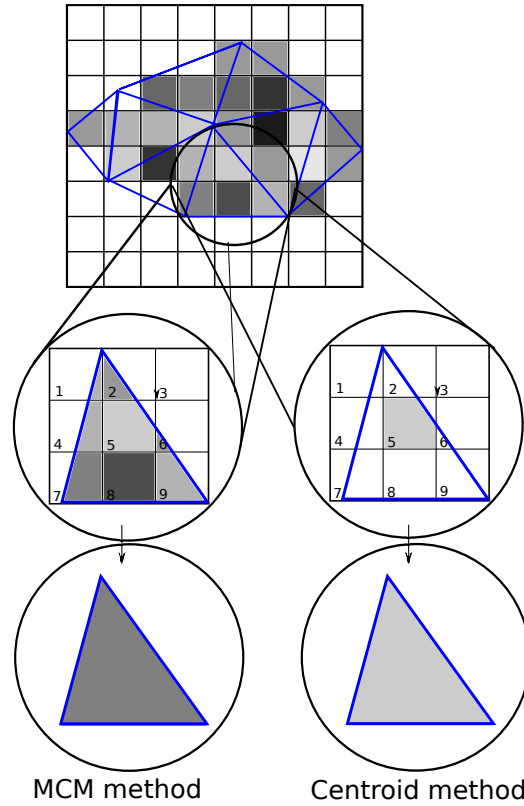


Figure 2.6.3: Tetrahedral density map generation. The mass of a tetrahedral element equals the sum of the masses of volumes of intersection between the tetrahedron and the grid of voxels. Example of applying equation (2.6) in a 2D space: $m(T_k) = m(I_k^1) + m(I_k^2) + m(I_k^4) + m(I_k^5) + m(I_k^6) + m(I_k^8) + m(I_k^9)$ for the MCM method. In the case of the Centroid Method: $m(T_k) = m(V_s)$.

masses of the overlapping volumes. Next, a density value can be obtained for each tetrahedron :

$$\rho(T_k) = \frac{\sum_{j \in J_k} m(I_k^j)}{\text{vol}(T_k)} \quad (2.7)$$

where $\text{vol}(T_k)$ represents the volume of the tetrahedron k . We are going to refer to this method of assigning a different density for each tetrahedral element as the Mass Conservation Mapping (MCM). For the rest of this chapter, the MCM method will be evaluated and compared to the centroid mapping method (CM). The latter is an approach introduced by Ishikawa et al. [148], and it defines the density value of a given tetrahedron as the density of the voxel containing its

centroid (see figure 2.6.2).

2.6.2 TIME-DEPENDANT DOSE COMPUTATION ON DEFORMABLE TETRAHEDRONS

Instead of accumulating dose distribution using regular grids of voxels describing the internal anatomy at every time step during the respiratory cycle, we calculate the time-dependent dose deposition on deformable tetrahedral meshes that contain material density information. The total dose distribution inside a tetrahedron can be calculated as the integral of the energy distribution inside the tetrahedron over its mass.

$$D^{TOTAL}(T_j) = \frac{\int_t E(T_j)(t) \cdot dt}{m(T_j)} \quad (2.8)$$

In practice:

$$D^{TOTAL}(T_j) = \frac{[\sum_{i=1}^{n_i} E(T_j)(t_i)]\delta i}{m(T_j)} \quad (2.9)$$

where $E(T_k)(t_i)$ is the energy deposited inside the tetrahedron T_k at the time step t_i and $m(T_k)$ represents its mass and δi is the duration of the time step t_i .

Contrary to voxel-based methods that use image registration algorithms to track individual voxels from one frame to another, our tetrahedral-based method implicitly tracks the tissues as the tetrahedral meshes maintain their topology from one deformation step to another. As an example, the tetrahedron T_k at the time t_A will remain T_k at the time t_B , and will be defined by the same four vertices. Image-based methods that make use of linear interpolation for dose estimation cannot fully take into account the change in the density of each lung voxel during ventilation, since the dose deposited inside each voxel is computed as the energy deposited inside the voxel divided by its mass, as discussed in [159]. Using deforming tetrahedral meshes, the density variations are implicitly included in the simulations. In the following subsection, an implementation of this dose computation method based on the GEANT4 toolkit is described.

2.6.3 GEANT4-BASED IMPLEMENTATION

Geant4¹ is a toolkit used for particle/matter interaction. It supports volumes defined by tetrahedral elements. *Poole et al.* demonstrate that defining a volume as an assembly of tetrahedra reduces the navigation time by two orders of magnitude as compared to a tessellated solid (closed triangular surface) often obtained by Computer Aided Design [160]. However, there is no notion of mesh in Geant4 from a topological point of view, i.e. there is no correspondence between the vertices of the mesh and the tetrahedral mesh elements. Internal motion is described by mesh vertex displacement and not by volume transformations, as it is usually done in most Geant4 applications. For this reason, we have created a mesh-like structure where each vertex in the mesh has a unique identifier and every tetrahedral volume (G4LogicalVolume) is associated to four vertex identifiers.

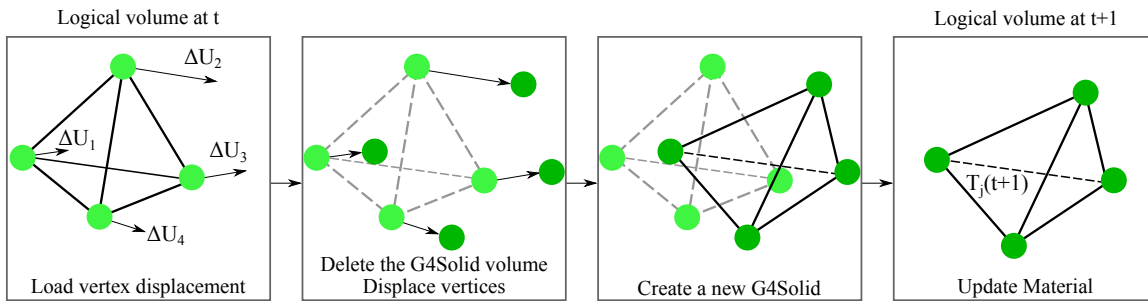


Figure 2.6.4: Deformable tetrahedron implementation using Geant4

Fig. 2.6.4 shows how the deformation of a tetrahedron T_k from one time step t_i to another t_{i+1} is implemented using the Geant4 geometry description. First, the solid volume (G4Tet) at the time step t_i is removed. Next, the positions of the vertices S_j^k describing the volume are updated: $S_j^k(t_{i+1}) = S_j^k(t_i) + \Delta U_j(t_i \rightarrow t_{i+1})$, $j = 1 \dots 4$, where $\Delta U_j(t_i \rightarrow t_{i+1})$ is the displacement of the vertex S_j^k from t_i to t_{i+1} . A new solid volume (G4Tet) is then constructed using the new position of the vertices. The vertex displacement modifies not only the shape but also the volume of the tetrahedra. Therefore, at each time step, a new density is calculated respecting mass conservation principle. Finally, depending on density variation, the material properties of the logical volume (G4Material) are updated. The deposited energy is thus calculated inside each tetrahedral element at every time step t_i and accumulated inside these elements. The geometry is updated at the beginning of each time step t_i .

¹<http://geant4.cern.ch/>

Algorithm 1 summarizes this implementation.

Algorithm 1: Dose accumulation using Geant4 and deformable tetrahedral meshes. n_t and n_T are respectively, the number of steps and the number of tetrahedra.

Initialize simulation: beam parameters, physical models, etc.

for $1 \leq i \leq n_t$ **do**

 Modify geometry

 Recalculate material densities

 Shoot particles at the target

for $1 \leq j \leq n_T$ **do**

$$E^{TOTAL}(T_j) = E^{TOTAL}(T_j) + E(T_j)(t_i)$$

end for

 Calculate $D^{TOTAL}(T_j)$

end for

At first, the simulation is initialized, meaning that the beam parameters and the physical models are set. Then, the simulation is divided into temporal frames (t_i). For each temporal frame, the geometry of the tetrahedral meshes is modified as a consequence of calculated vertex displacements. If needed, the densities of the material used in the simulation are updated. Next, a number of particles is shot at the target. This number of particles depends on the duration of the time frame. During this step, usually referred to as a "run", the geometry cannot change. For each tetrahedron in the mesh the deposited energy during the run is calculated ($E(T_k)(t_i)$) and is added to the total energy deposited in the tetrahedron $E^{TOTAL}(T_k)$. Finally, once all the deposited energy has been accumulated inside every tetrahedron T_k , the dose values for each node of the mesh are calculated.

2.6.4 BEAM SHAPING AND CONFIGURATION

In order to take into account the shape of the tumor in hadrontherapy beam line simulation and to improve the efficiency of treatment delivery, we have developed an algorithm that constructs a patient-specific range compensator (RC) and multileaf collimator (MLC) from CT images (see algorithm 2). These two devices are used in passive scattering to shape the beam and to minimize the delivery dose in organs at risk (OAR).

The 3D voxelized image A is defined as a $M \times N \times P$ matrix, we consider a *voxel line* (VL) as a set of voxels aligned all together in the direction of the beam (z – *direction*) and it is defined as follow

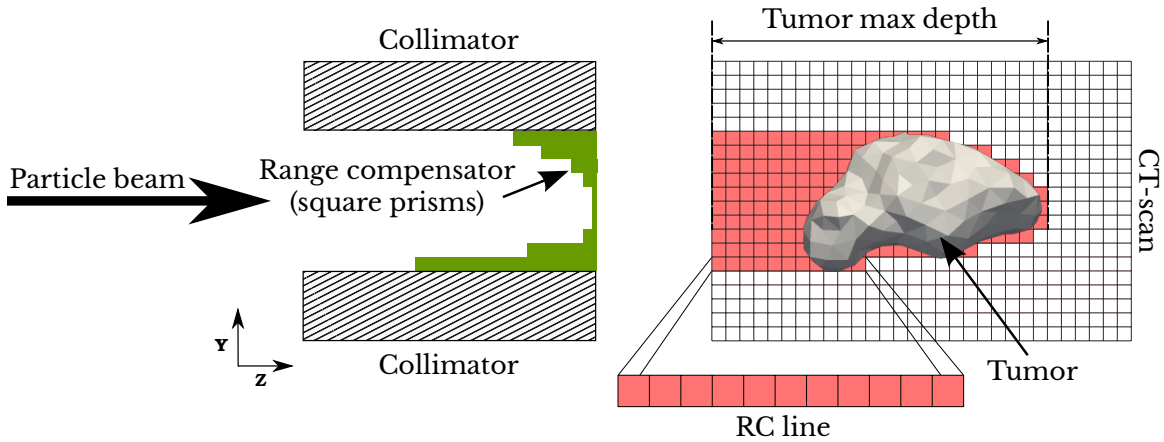


Figure 2.6.5: Beam shaping with range compensator and multileaf collimator. In this particular example we have 10 *RC lines*.

: $VL_{ij} = \{A_{ijk}\}$ for $k = 0, \dots, l$ with $0 \leq l \leq P$. Let *RC line* be a *VL* that is with intersection with the tumor and where l is the index of the last voxel with intersection. The range compensator is constructed based on the set of all the *RC lines*. In fact, for every *RC line* we construct a square prism (*SP*) having the same width and height, and its depth is calculated using the water equivalent thickness of all the voxels.

With regard to the collimator, it is created by adding square prisms around the range compensator. A very dense material such as Tungsten has to be used to stop particles that are outside of the field of the tumor.

To take into account the geometry of the tumor in dose delivery, a clinical target volume (CTV) was defined. First, the gross tumor volume (GTV) was segmented using ITK-SNAP[161] for all the phases of CT-data, then, a margin of 3 voxels was added. This value was deduced from the lateral penumbra of the used proton beam to have a homogeneous physical dose.

We have defined a class called `RangeCompensatorConstructor` that takes as input the CTV volume and generates in a pre-processing phase a `gdml` (Geometry Description Markup Language) file containing the XML description of the geometry and the materials used for both the range compensator and the collimator. This file is loaded and parsed in run time by `G4GDMLParser` object, then, the resulting volumes are added to the simulation scene.

Besides, tumor depth and length are generated and passed to `sobpConstructor` object in order to configure the beam. As depicted in figure 2.6.6 The Spread-Out Bragg Peak (SOBP) is achieved

Algorithm 2: Calculation of the depth of all square prisms in range compensator.

```

TumorMaxDepth = -infinity ;
foreach RC linei,j do
  | foreach voxel in RC linei,j do
  | | SPi,j.Depth+ = WaterEquivalentThickness(voxel)
  | end
  | if SPi,j.Depth > TumorMaxDepth then
  | | TumorMaxDepth = SPi,j.Depth
  | end
end
foreach SPi,j in RC do
  | SPi,j.Depth = TumorMaxDepth - SPi,j.Depth
end

```

by using seven particle sources placed inside a water box to shift their range, each one of them generates a Bragg Peaks (BP) with different number of particles.

this object creates a macro file containing the definition of all the particle sources used for the simulation. 3×10^7 primary protons with 270 MeV energy were generated by all the sources. this configuration allows an average statistical uncertainty for the dose deposited in the tumour below 2%.

2.7 EVALUATION AND RESULTS

In order to evaluate the tetrahedral-based dose accumulation approach, we have built a GEANT4-based application able to include deformable tetrahedral geometries together with the passive scattering beam line. Simulations have been performed on two different phantoms in this study: A constructive solid geometry (CSG) spherical phantom, and a real patient case from the DIR-lab[162] database. The purpose of this simulations was to investigate the differences between the tetrahedral and the voxel-based models when accumulating dose distributions over time.

2.7.1 CONCENTRIC SPHERES PHANTOM

In the aim of quantifying the difference in the amount of dose between the tetrahedral and the voxel-based structures, we have defined a CSG spherical phantom and then constructed the two

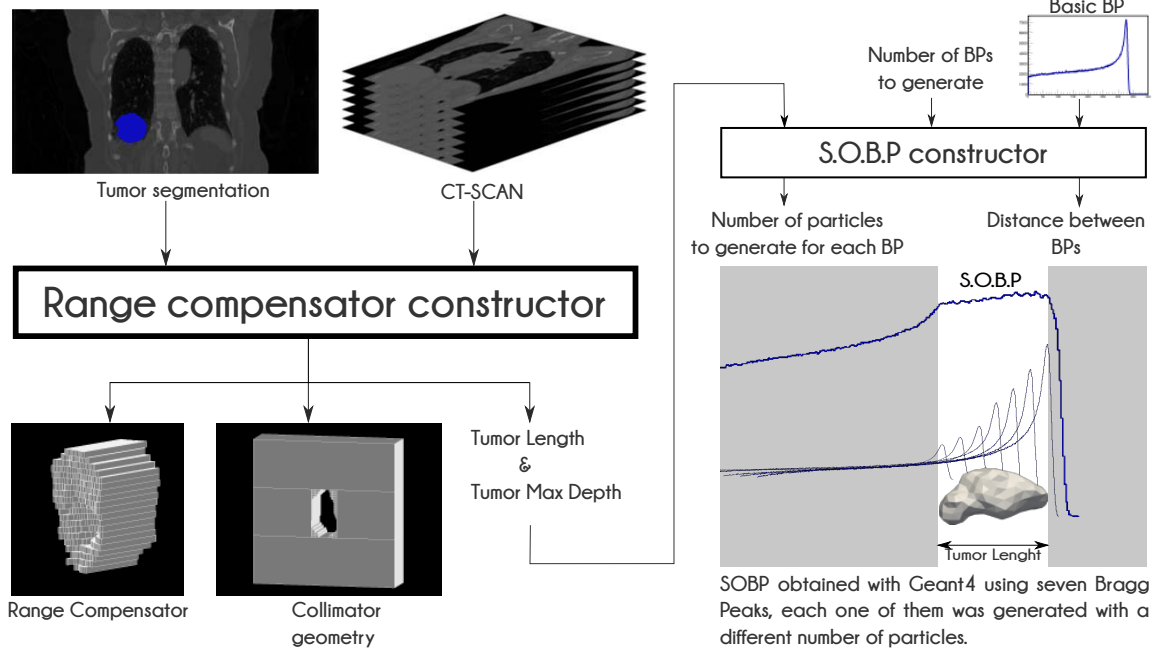


Figure 2.6.6: Range compensator and S.O.B.P constructor

structures based on it. The derived dose distributions of this phantom were considered as our gold standard in the evaluation. Three concentric layers of matter have been used: Tumor, Lung and Bone tissues (i.e. layers 0, 1 and 2 respectively) each of them with a different density value. Besides, a scaling transformation with a factor of 1.3 was successively applied four times to the target in order to mimic breathing motion and to have a total of five steps (i.e. $step_0$ to $step_4$). The deformations that the target undergoes were exaggerated, with the purpose of showing the limitations of voxel interpolation-based methods when dealing with important volume variations. The beam line configuration described in *figure 2.7.1* was used for all the simulation steps.

We have performed a Monte-Carlo simulation on the three representations with the aim of comparing the total dose deposited DD_l in each layer l over time. This measure is obtained using the following formula :

$$DD_l = \sum_{step=0}^4 DD_l(step), \text{ with } 0 \leq l \leq 2$$

The constructive solid geometry (CSG) spherical phantom was implemented using a set of three

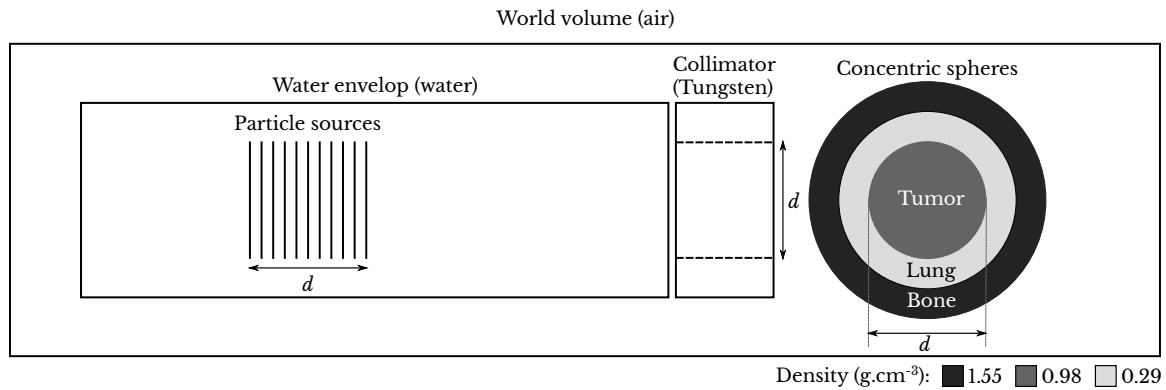


Figure 2.7.1: Sphere simulation setup in Geant4. 10 disk sources particles are placed inside the water envelop to generate the SOBP. A cylindrical collimator is used to adapt the passive beam to the inner concentric sphere (tumor).

spheres primitives in Geant4. With respect to voxel-based structure, we have used a cartesian grid of voxels that contains the discrete representation of the concentric spheres. In the last simulation, we have constructed the tetrahedral mesh by using Tetgen [163] on the concentric spheres triangular surfaces, then, we applied the process of density mapping on it.

Energy deposition distribution was first investigated with the plotting of energy profile of the concentric spheres with no motion for all the structures. Figure 2.7.2 shows that there is no compelling difference between the three curves. In the motion compensated simulation, dose evaluation was performed by accumulating dose values of each layer apart and calculates the dose relative error in comparison with the gold standard.

We note that with the same configuration and the same movement we get a slightly better results in dose accumulation with the tetrahedral mesh comparing to our gold standard (Table 2.7.1), even tough fewer elements have been used (2522 tetrahedra vs. 10^6 voxels). This is due to the fact that tetrahedral meshes represent better smooth surfaces, and also to the interpolation of dose values in the accumulation process, which is not an issue for the tetrahedral model since it accumulates dose inside the elements.

2.7.2 PATIENT CASE SIMULATION

We have used the case6 images from DIR-lab [162] data sets as a case study. It is a thoracic 4D-CT image that contains a set of ten respiratory phases (T_{00} , T_{10} ... T_{90}) covering a complete respi-

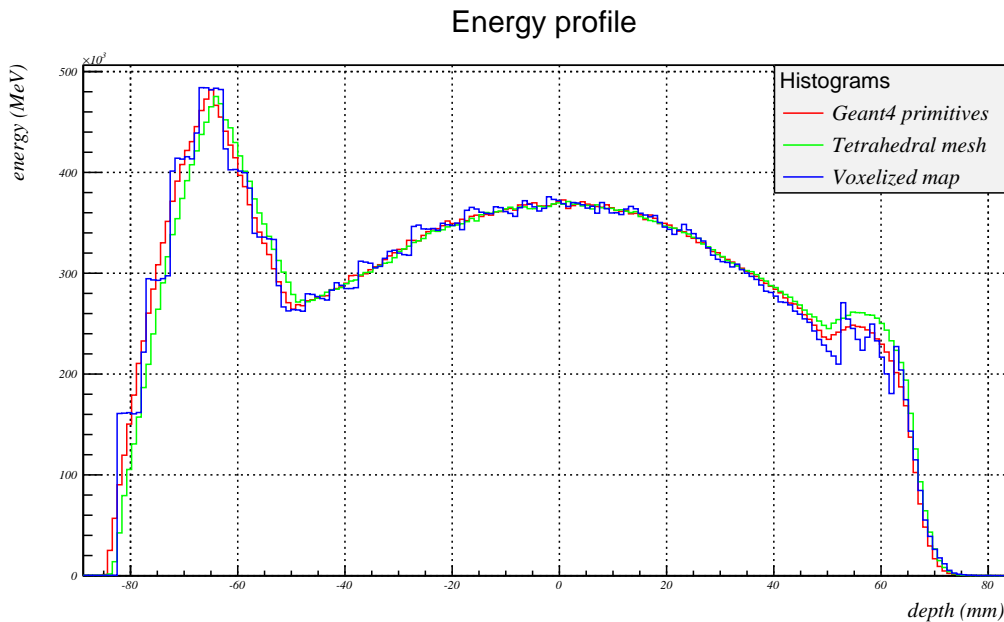


Figure 2.7.2: Energy profile of static simulation for the three geometric configurations : Geant4 primitives, tetrahedral mesh and voxelized map.

ratory cycle. The corresponding movement is generated using the deformable image registration (DIR) approach commonly used in voxel-based 4D dosimetry. Furthermore, it is applied to both tetrahedral and voxel-based structures to simulate the deformation. Therefore, even if errors of registration exist, they will affect both representations in the same manner.

Figure 2.7.3 illustrates the process used to accumulate dose in respiratory-induced simulations. The publicly available computer program for intensity-based medical image registration Elastix[164] was used for this study. We have opted for non-rigid B-spline registration, represented by a sparse grid of control points that covers the entire region to be registered. The transformation of a point can thus be computed from only a couple of surrounding control points. The CT image of phase T_{50} was defined as the reference image (3D density image $step_0$) in all the registrations. The output of the previous registration is provided as an initial transformation to the next one, in order to minimize registration errors. As depicted in figure 2.7.3, the generated B-spline grid is not only used to accumulate dose on voxel grid, but also to deform the tetrahedral mesh. Once we obtain the transformations between respiratory phases, we perform Monte Carlo simulation on the two structures

		Tetrahedral model		Voxelized model	
		not refined	refined	LR	NN
DED(%)	Layer ₀	1.21	0.0235	0.4018	0.1448
	Layer ₁	3.16	0.0224	0.1834	0.0779
	Layer ₂	3.87	0.1846	1.3558	0.6513

Table 2.7.1: Dose relative error of voxels and tetras comparing to gold standard of spheres simulation. DED: dose relative error, LR : Linear resampling, NN: nearest neighborhood. LR and NN are two different methods used for interpolation (see Appendix A.2 and A.3).

		Dose ($\times 10^{-4}$ Gray)			HI
		D_{min}	D_{max}	D_{mean}	
No motion	Voxels	0.64	1.77	1.41	1.30
	Tetras	0.40	1.97	1.41	1.30
With motion	Voxels	6.82	15.09	12.72	1.60
	Tetras	3.45	15.50	12.93	1.47

Table 2.7.2: Evaluation of dose distribution in tumor volume. D_{min} , D_{max} , D_{mean} are respectively the minimum, the maximum and the mean dose deposited. Hi (Homogeneity index).

and then accumulate dose. In order to take into account the shape of the tumor in hadrontherapy beam line simulation and to improve the efficiency of treatment delivery, we have developed an algorithm that constructs a patient-specific range compensator (RC) and a multileaf collimator (MLC) from CT images. These two virtual devices are used in passive scattering mode to shape the beam and to minimize the dose delivery in organs at risk (OAR).

2.7.3 DENSITY EVALUATION AND DOSE DISTRIBUTION COMPARISON

To assess the accuracy of density mapping after the construction of the tetrahedral model, voxel-based model, and tetrahedral mesh density distributions are compared. We define the density absolute error (DAE) of a given voxel V_i , as: $DAE(V_i) = |\rho(I_i) - \rho(M_i)|$, V : is the DAEs image, I : is the voxel-based structure, and M is the voxelized tetrahedral model. The histogram of DAEs shows that 92% of voxels have a DAE less than $0.1 \text{ g} \cdot \text{cm}^{-3}$, and the mean DAE of all the voxels is $0.055 \text{ g} \cdot \text{cm}^{-3}$ which is considered very low.

The calculation of dose distribution has been performed with Monte Carlo simulation approach in which three million proton particles with an energy of 270 MeV were fired into the target for ev-

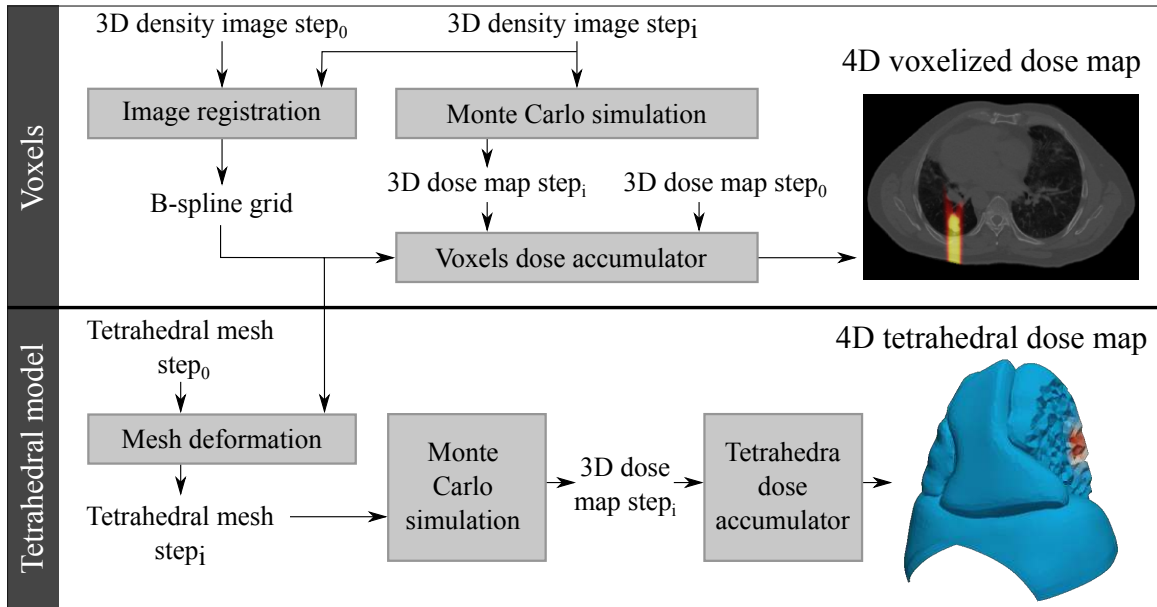


Figure 2.7.3: Flow chart of 4D dose accumulation in respiratory motion-induced simulation.

ery step. While the resulting dose values are accumulated on tetrahedral elements in the tetrahedral model, they are summed to the reference phase T_{50} for the voxel-based model by using the inverse transformation of the movement. As illustrated in Fig.2.7.5, dose distributions are almost the same and dose values are in the same order of magnitude. To investigate dose homogeneity and uniformity in the lung tumor volume, dose distributions are converted into 2D cumulative dose-volume histograms (CDVH). These curves give the percentage of volume within a defined volume that received more than a certain amount of dose. Besides, CDVHs also allow to define parameters like maximum dose (D_{max}), minimum dose (D_{min}) and mean dose (D_{mean}) as well as homogeneity index $HI = \frac{D_5}{D_{95}}$, where D_5 and D_{95} are respectively the minimum dose of 5% and 95% of the target volume. The ideal value is 1 and it increases as the distribution becomes less homogeneous [165]. As shown in Fig.2.7.4, the CDVH curves fit very well even though there is a difference in HI s due mainly to: the voxelization of the tetrahedral dose map, the DAEs and also the averaging out of the density distribution. The last one is responsible for the over-estimation of dose in the tetrahedral model, and also for having a higher HI . For the same reasons, a small difference between the values of D_{min} , D_{max} , D_{mean} is observed in table 2.7.2.

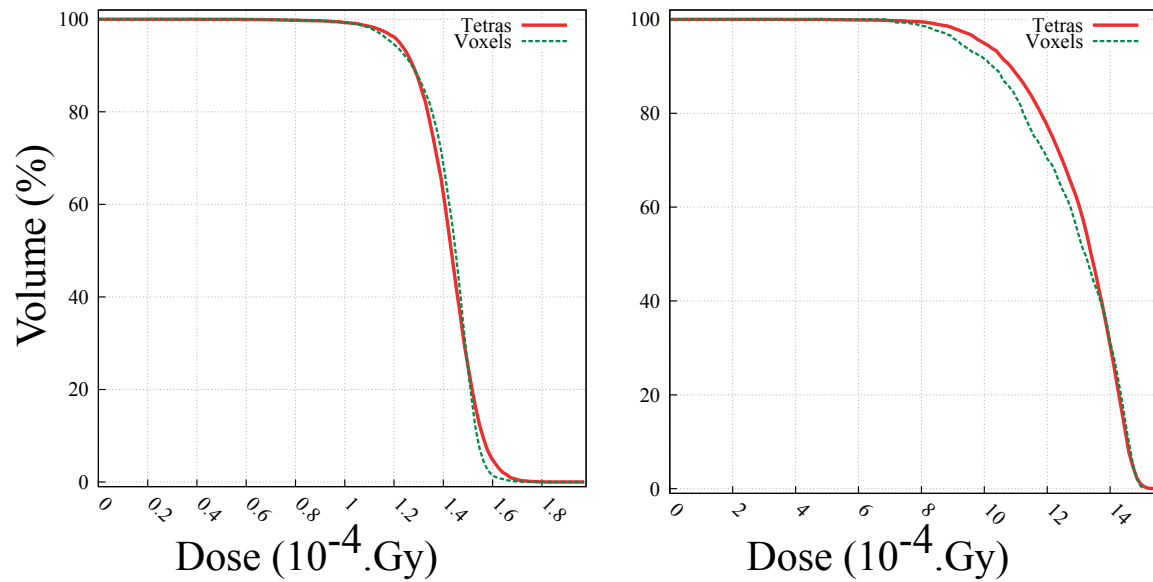


Figure 2.7.4: Cumulative dose volume histogram (CDVH) deposited in the tumor. Left : no motion, right : with motion.

2.7.4 DISCUSSION AND CONCLUSION

We have presented in this study a comparison between tetrahedral model and conventional voxel-based structures, using a thoracic 4D-CT data of a patient case. An implementation of the deformable tetrahedral model was done using the Geant4 Monte Carlo code in order to simulate particle-matter interactions. We have shown that the deformable tetrahedral model gives accurate 4D dose distribution with respect to the voxel-based structure. The use of this model can significantly improve the accuracy of dose calculations when organ motion is important since it respects the mass conservation principle. Besides, it can be directly used together with biomechanical models based on FEM. Finally, an experimental validation based on a physical breathing phantom would draw a definite conclusion, regarding the performance of our method to be used in clinical cases. Furthermore, dose accuracy can be improved by refining the mesh and using more elements. However, the simulation time will increase accordingly. In the next section, we define a multiresolution tetrahedral model to study the effect of the number of tetrahedrons on the final dose as well as the calculation time needed for the simulation.

2.8 MULTIREOLUTION TETRAHEDRAL MODEL CREATION

In this section, we will investigate the effect of the number of tetrahedrons in the mesh on the dose distribution of Monte Carlo dose calculations, considering CM and MCM density mapping methods. The main purpose is to find the optimized number of elements to have an accurate dose distribution and also to reduce both loading and simulation times. This is achieved by constructing a Multiresolution tetrahedral model that defines multiple levels of detail employing a user-specified element volume constraint. Furthermore, we perform proton beam irradiation tests on a lung geometry to quantify the performance of MCM and CM methods in Monte Carlo dose computations using the Geant4 platform. Note that several authors in [166] and [167] have simplified the patient geometry in the conventional voxel-based structures in Geant4 to create accelerated structures hence by defining sub-regions.

2.8.1 MULTIREOLUTION TETRAHEDRAL MODEL

Several image-to-mesh approaches have been proposed in the literature to generate tetrahedral meshes from the image. Chernikov and Chrisochoids [168] [169] present an algorithm for tetrahedral image-to-mesh conversion. It allows for guaranteed bounds on the smallest dihedral angle and on the distance between the boundaries of the mesh and different tissues. The proposed mesh decimation procedure named Lattice Decimation (LD I2M) first generates a high quality refined octree-based mesh then, coarsens it to a lower number of elements with a vertex removal operation by respecting the required bounds. This method has the advantage of generating a small number of elements while maintaining tetrahedral element quality. The method has been evaluated using real medical images of abdomen and brain, containing 75 and 149 tissues, respectively. Multiple fidelity bounds were applied to investigate mesh size and running time comparing to tetgen and Cgal. Final results proved that LD solves the small dihedral angle problem. However the number of elements is quietly the same as the one of tetgen mesh, and much bigger than the CGal one. With regards to the execution time, although, LD is better than tetgen, CGal shows that it is much faster using the appropriate optimization algorithms. Even though this method produce good results, the user still not have the control of the organs surfaces. Since, the method uses only a labeled image of segmented organs as input. Fang and Boas [170] have developed a toolbox for tetrahedral mesh generation from binary and gray-scale medical images. It includes several available free

mesh processing tools and libraries. The mesh generator is based on the Delaunay method, therefore it inherits its drawbacks, like having very small dihedral angles. The region boundaries are represented using the iso-surfaces constructed from the input image. In the case where there are multiple regions, it is difficult for a surface meshing algorithm to produce a topologically correct mesh free from self-intersections and overlapping regions. Besides, it generates a lot of faces that require repairing and simplification. Courchesne et al. [171][172] propose an algorithm to generate a patient-specific tetrahedral mesh directly from the image data. They have built a metric to control the mesh adaptation process. This method creates an anisotropic mesh that doesn't ensure element quality, and it is not suitable for biomechanical simulations of Lung cancer and also for density mapping. The use of these methods creates an adaptive tetrahedral mesh where small elements are in high gradient regions. However, the presence of a lot of tissues with different density values in the thorax tends towards producing small tetrahedrons in the entire geometry. Besides, we found that it is equivalent to a uniform meshing with volume constraints. Next, we will present our approach to create tetrahedral meshes with different level of details.

Tetrahedral model generation process: Fig. 2.8.1 depicts the flowchart of the creation of the multi-resolution tetrahedral model. The same method was used in previous simulations.

The first step is the processing of CT data. In this context, images are firstly preprocessed by thresholding the image intensities. Next, the organs of interest are segmented using the *snake evolution* method based on active contours. Using the *marching cubes* technique, triangular surface meshes corresponding to organs and tumor are extracted. Further on, they are converted into tetrahedral meshes using Tetgen software [173],[158] based on the Delaunay technique. Finally, the mass densities are mapped to the tetrahedral meshes either on the element or on the vertices, depending on the used density method.

Tetrahedralization and generation of different Levels of detail (LODs): : Once the organs of the patient are segmented (figure.2.6.1), the constrained Delaunay tetrahedralization method (CDT) is used to tetrahedralize the surface of the mesh. This approach can generate meshes with different resolutions by applying an upper bound β on the volume of the elements. Therefore, the algorithm ensure that all the tetrahedra of the generated mesh have a volume bellow β . Thus, starting from a refine mesh having the same resolution of the CT-image, the levels of detail are obtained by up-

sizing the mesh elements volume gradually until reaching the mesh with the minimum number of elements. The following formula defines the bound β_i used in a given resolution i as:

$$\beta_i = 2^i \times v \quad , \quad i \geq 2 \quad (2.10)$$

where v is the voxel volume.

It should be noted that the lower the i value the more elements are in the mesh. To calculate the compression rate of the reference voxel-based volume (3D CT-scan) with respect to a tetrahedral mesh of a given level of detail, we define the *voxel – to – tetrahedron ratio* (VTR). Which is the ratio between the number of voxels and tetrahedra defining the organ.

Geometry configuration: A first investigation of the effect of the resolution of the mesh on dose distribution is done on a lung geometry containing a tumor. The tetrahedral meshes were generated by considering the surface of the tumor as a hole inside the lung surface (see figure 2.8.2). This allows the separation between the two organs while respecting their surfaces. In addition, two scenarios were tested by defining two single-field beams in opposite directions. Each with an adapted collimator and range compensator. The target being the tumor, in the first one, the particles travel in the direction posterior-anterior and the second one in the anterior-posterior direction. In the latter configuration, the beam penetrates a more heterogeneous medium composed of the lung, bronchial tree, and tumor tissues as well as air. The Geant4 (Gometry ANd Tracking) [143] toolkit was used in this work for Monte Carlo simulations and dose calculations. A second investigation was furthermore performed on a patient case (see figure 2.8.3) to confirm our findings using multiple regions.

Results and discussion: To evaluate the dose in every resolution of the tetrahedral mesh, we use the gamma tool (or γ tool) [174]. This tool allows quantifying the resemblance between a given dose distribution with respect to a reference dose distribution. It provides a gamma value map where the values are calculated for each reference point using the entire evaluated distribution.

For a reference point P_r , the gamma value is:

$$\begin{cases} \gamma(P_r) = \min_{P_e} \Gamma(P_e, P_r) \forall P_e \\ \Gamma(P_e, P_r) = \sqrt{\frac{|P_e - P_r|^2}{\Delta d^2} + \frac{\delta^2(P_r, P_e)}{\Delta D^2}} \end{cases} \quad (2.11)$$

With $|P_e - P_r|$ is the euclidean distance between evaluated and reference dose points and $\delta(P_r, P_e) = D_e(P_e) - D_r(P_r)$ the difference between evaluated dose $D_e(P_e)$ at position P_e and the reference $D_r(P_r)$ at position P_r . ΔD represents the dose difference criterion while Δd is the Distance-To-Agreement (DTA) criterion. This distance refers to the distance allowed from the position of the dose value in the evaluated distribution to the location of the closest value in the reference distribution. The gamma pass rate represents the percentage of voxels that pass the gamma test. Figure 2.8.4 shows the effect of the mesh resolution on the gamma pass rate of the lung geometry. Thus for the two particle beams. In the first beam configuration (i.e., beam 1), the value of the gamma pass rate is stable over the resolution and doesn't undergo significant changes. This stability is related to the small distance between the outer surface of the lung and the tumor: this close distance, constraints the algorithm of tetrahedralization to create small elements in this region and causes a precise density distribution. However, for the second beam configuration (i.e., beam 2), the value of the gamma pass rate is proportional to the number of tetrahedral elements used in the mesh. This behavior was confirmed in the patient case geometry in which the gamma pass rate goes from 99% to approximately 94% for VTR values higher than 30. As a conclusion, we demonstrated that our density mapping method (MCM) need a VTR lower than 20 to have a gamma pass rate higher than 95%. Even though the principle of mass conservation is respected for all the level of details of the mesh, the value of the gamma pass rate is not constant.

Furthermore, the relationship between the total time needed for the entire simulation and the number of tetrahedrons is illustrated in figure 2.8.6. The total time is defined as the sum of the loading time and the simulation time. The former is the time needed to load the geometry into the Monte Carlo code, and The latter represents the simulation time of the interaction between the geometry and the particle beam. The final results show that the simulation time is constant and almost independent of the number of tetrahedrons. Contrary to the simulation time, the loading time is proportional to the number of elements in the mesh and can reach two hours for a mesh with 350K tetrahedrons.

As a conclusion, to obtain accurate dose distributions with MCM method, we need fine tetrahedral meshes. However, the high number of tetrahedrons can quickly be time-consuming. On the other hand, we can also assume that respecting the principle of mass conservation with MCM in coarse meshes doesn't ensure high gamma pass rates.

To solve this problem, we have studied the impact of the water equivalent path length on the dose. In the next chapter, we will introduce a new approach that defines the density of the tetrahedral elements according to the direction of the beam.

2.9 CONCLUSION

In this chapter, we described our four-dimensional dose calculation method based on the principle of mass conservation, as well as its implementation on the Geant4 platform. We have shown that tetrahedral meshes give accurate dose maps as conventional voxel-based structures in breathing simulation. Furthermore, we have created a multi-resolution tetrahedral mesh to study the impact of the number of tetrahedron elements on the dose. Our results proved that fine tetrahedral meshes with a high number of elements are required to obtain acceptable gamma pass rates. Besides, we concluded that in most cases, the dose accuracy is proportional to the level of detail of the mesh.

However, if we want to minimize the number of tetrahedrons and reduce time computation, we need a new approach that ensures the precision of the water equivalent path length of the traversed materials. Thus, in the next chapter, we will introduce a new method in which we will minimize the error of the water equivalent path length in the direction of the treatment beam.

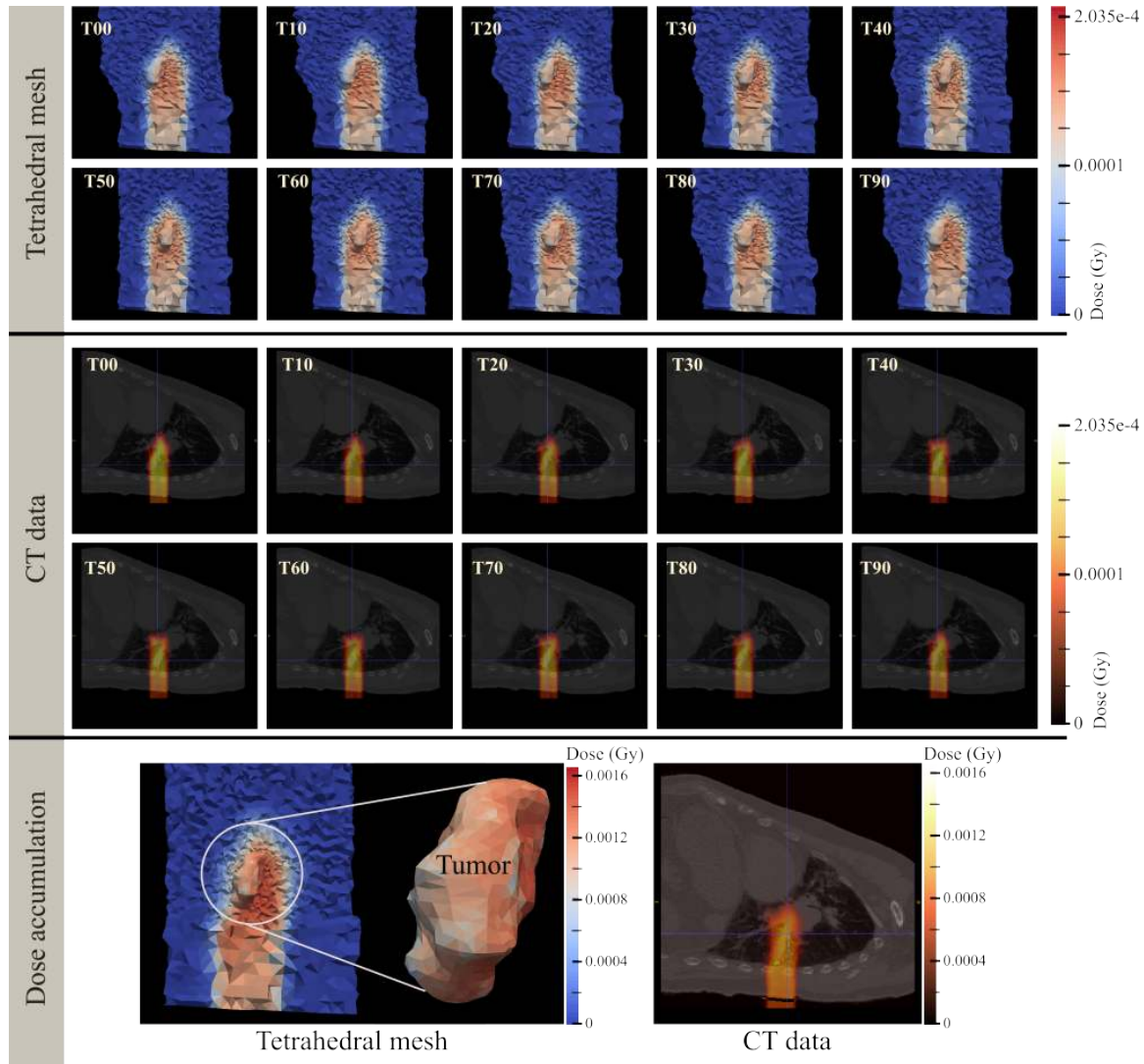


Figure 2.7.5: Dose distributions of Monte Carlo simulations. Top: tetrahedral model. middle: sagittal view of voxel grid. Bottom: 4D Dose distribution (left: accumulated dose in tetrahedral mesh. right : accumulated dose in CT data for all phases.

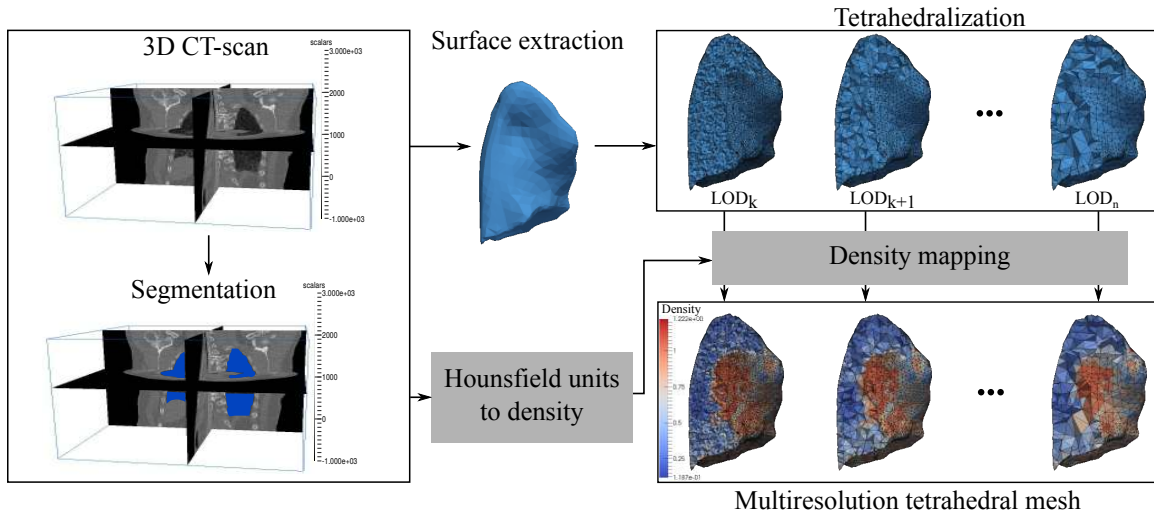


Figure 2.8.1: Flowchart of tetrahedral model construction: from 3D-CT to multiresolution tetrahedral model. The CT images are first converted into voxelized mass density maps which are then mapped to the tetrahedral elements of the meshes.

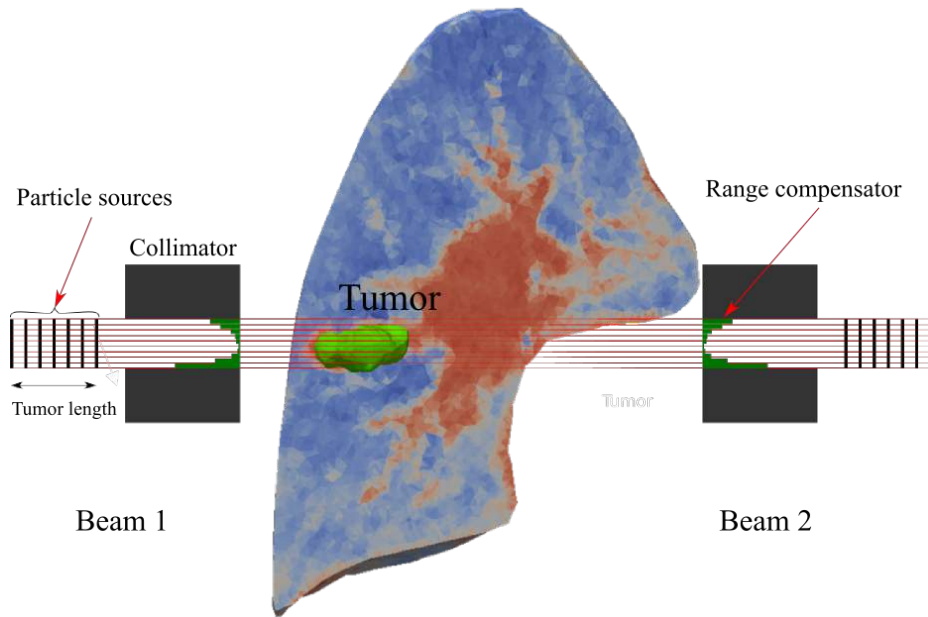


Figure 2.8.2: Tps configuration for lung. Two single filed passive beams were used in opposite directions, each with its own range compensator and collimator.

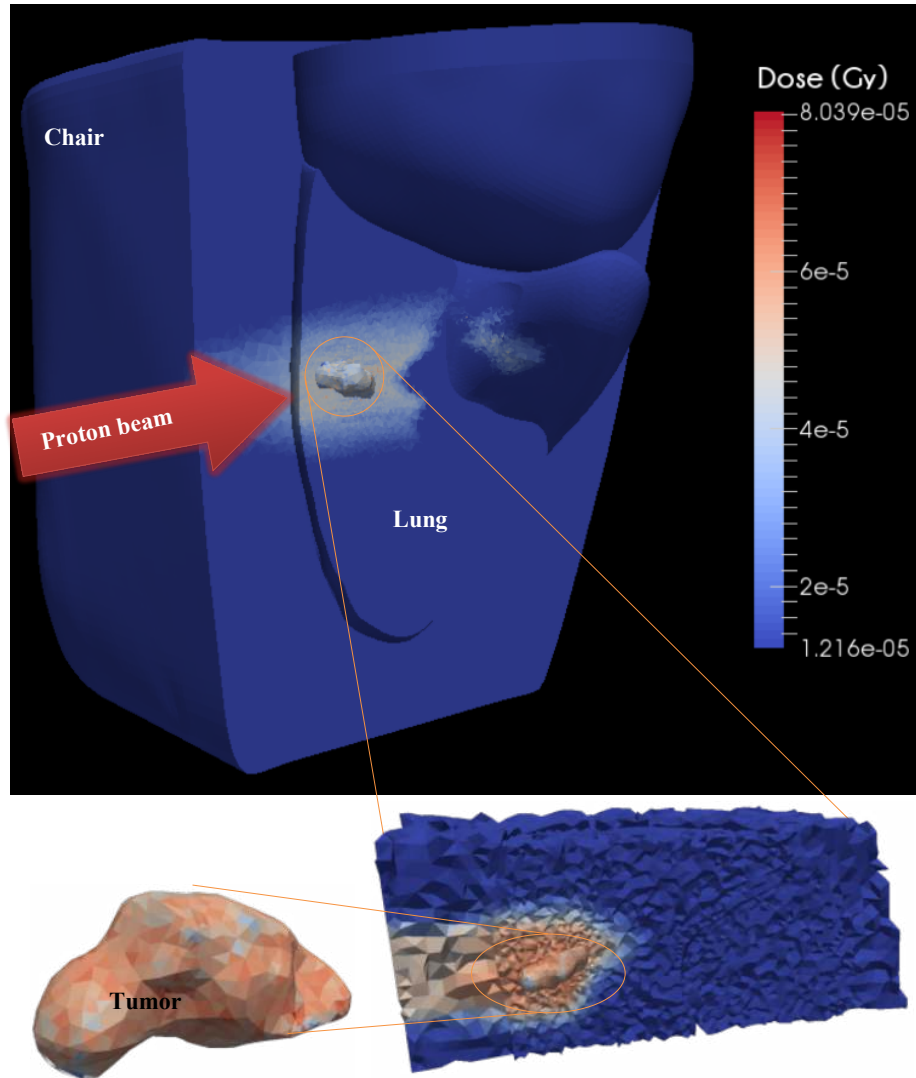


Figure 2.8.3: A thorax geometry representing a patient case used for the multiresolution study. The proton beam is directed toward the tumor and the dose is saved in the tetrahedral elements of the mesh.

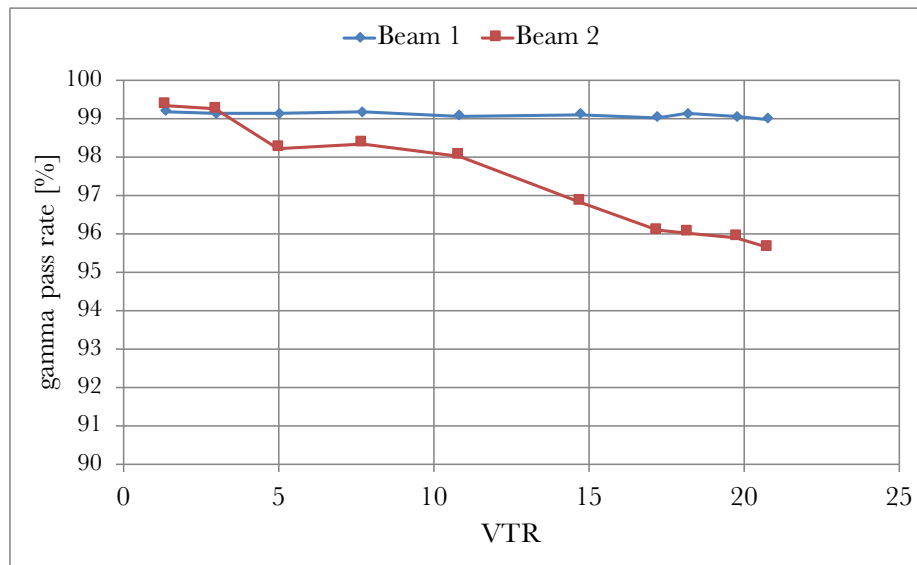


Figure 2.8.4: Gamma pass rate vs the voxel-to-tetrahedron ratio using a dta equal to $3mm$ and a dose tolerance of 3% . Beam 1 and Beam 2 are the proton beams used in the lung case illustrated in figure 2.8.2.

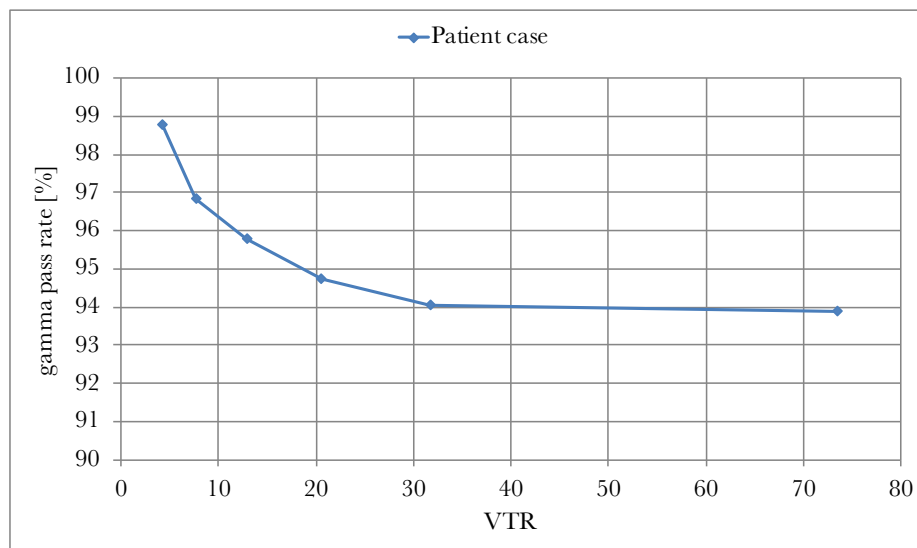
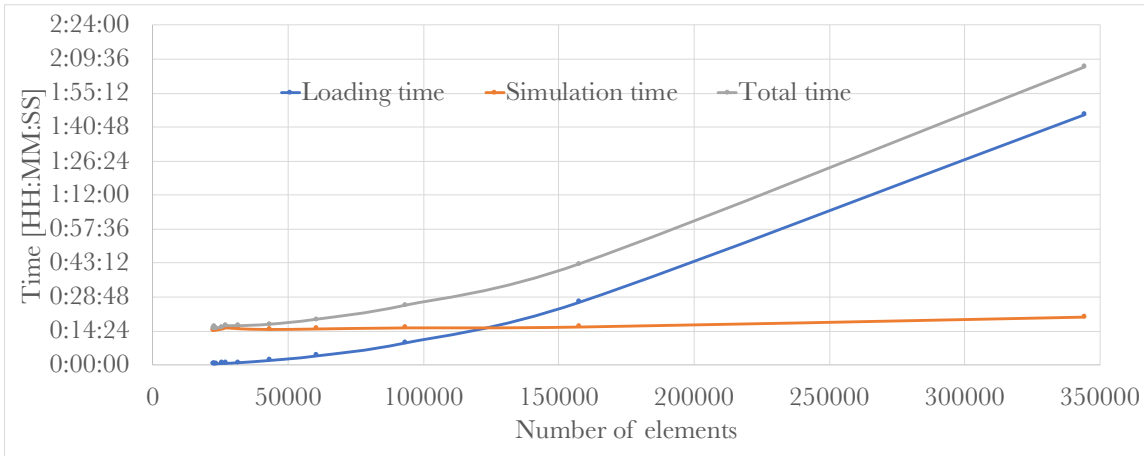
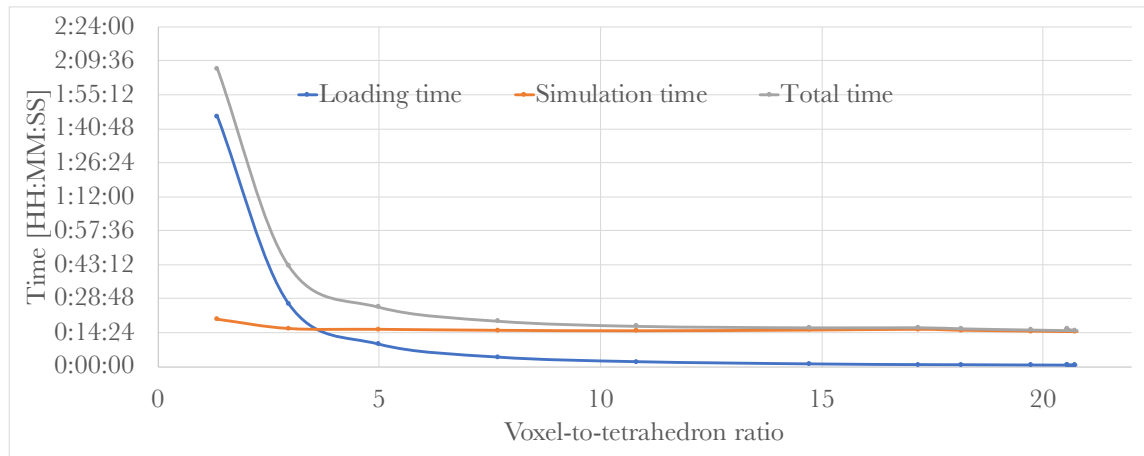


Figure 2.8.5: Gamma pass rate vs the voxel-to-tetrahedron ratio for the patient case simulation. For the gamma evaluation a dta equal to $3mm$ and a dose tolerance of 3% have been used.



(a)



(b)

Figure 2.8.6: Relation between computation time and the resolution of the tetrahedral mesh. (a) Number of tetrahedrons versus calculation time. (b) Voxel-to-tetrahedron ratio versus calculation time. Loading time is the time needed to load all the tetrahedral elements to the system. Simulation time is the time taken by the Monte Carlo code to calculate the interactions between the particle beam and the matter. The total time is the sum of loading time and simulation time. These values were calculated using 10^5 proton particles fired at the multiresolution lung geometry.

Good judgment comes from experience, and a lot of that comes from bad judgment.

Will Rogers

3

Particle-beam-dependent optimization for dose calculation

3.1 INTRODUCTION

In this chapter, we define a new methodology to calculate dose in tetrahedral geometries. As proved in the previous chapter, respecting the principle of mass conservation in the hole geometry when calculating the densities of tetrahedral elements is not sufficient to ensure coherent dose distributions when using coarse meshes. We have also shown that this outcome is caused by the non-compliance of the water equivalent path length calculated using the modeled tissues and the reference WEPL defined on the CT-scan data. Our main contribution in the field consists of defining a new dose calculation method that doesn't depend on the resolution of the mesh and aim at reducing the complexity of the geometry while maintaining a precise dose map. The objective is to reduce both memory consumption and simulation time in Monte Carlo simulations by decreas-

ing the number of tetrahedrons in the mesh. Our approach takes advantage of the direction of the radiation beam to minimize the error of the water equivalent path length of the matter before the tumor, thus between the images designated as the gold standard and the density distribution calculated using our method. In the following sections, we will first discuss the conclusions of our work, then we will finish with our article published in the peer-reviewed medical journal: *Physics in Medicine and Biology*. The article contains the methods, the results, and the discussion of the results obtained with our dose calculation technique.

3.2 CONCLUSION

The results of this study showed that by minimizing the error of the water equivalent path length in the direction of the beam, an accurate dose distribution could be obtained. Therefore, by applying our beam-dependant algorithm on a coarse tetrahedral mesh, we generate more faithful dose map inside the tumor volume compared to conventional density mapping methods. This outcome is the consequence of the generated effective density map used in the Monte Carlo simulation, that allows reducing the mean error of the WEPL by 9.62 mm in the case of the multi-layer phantom and 1.94 mm for the thorax geometry. As a conclusion, the time needed to simulate and load coarse tetrahedral geometries can be 25 % shorter than the time required in both fine tetrahedral meshes and voxel-based models. The creation of patient-specific tetrahedral phantoms can take less time by adopting our approach since the definition of the density map doesn't mainly rely on the resolution of the mesh. Furthermore, our target-oriented dose calculation method can be extended to handle more organ volumes other than the tumor, such as organs at risk if more dose precision is needed in those regions. In the next chapter, we will discuss a motion compensated version of our algorithm that takes into account the density variation over different breathing phases and also tissue deformation.

3.3 THE ARTICLE

Particle-beam-dependent optimization for Monte Carlo simulation in hadrontherapy using tetrahedral geometries

Yazid Touileb^{1,2}, Hamid Ladjal^{1,2}, Michael Beuve², Behzad Shariat¹

¹ Univeristé de Lyon, Univeristé Claude Bernard Lyon 1, LIRIS, UMR 5205 F-69622, France

² Univeristé de Lyon, Univeristé Claude Bernard Lyon 1, IPNL, UMR 5822 F-69622, France.

E-mail: yazid.touileb@liris.cnrs.fr, hamid.ladjal@liris.cnrs.fr, m.beuve@ipnl.in2p3.fr, bshariat@liris.cnrs.fr

Abstract.

The use of tetrahedral-based phantoms in conjunction with Monte Carlo dose calculation techniques has shown high capabilities in radiation therapy. However, the generation of a precise dose distribution can be very time-consuming since a fine tetrahedral mesh is required. In this work, we propose a new method that defines the density distribution of patient-specific tetrahedral phantoms, based upon the CT-scans and the direction of the particle beam. The final purpose is to coarsen the tetrahedral mesh to improve computational performance in Monte Carlo simulations while guaranteeing a precise dose distribution in the target volume. Contrarily to the state of the art methods that calculate the density value of a tetrahedron, locally based only on the CT-scans, our approach takes also into account the direction of the beam to minimize the error of the water equivalent thickness of the tetrahedrons before the tumor volume. In this study, the experiments carried out on a multi-layer computational phantom, and a thorax geometry, show that by applying our method on a coarse mesh, we offer a better dose distribution inside the tumor compared to other density mapping methods, in the same level of detail. This is due to the reduction of the water equivalent path length error from 9.65 mm to 0.62 mm in the case the multi-layer phantom, and from 2.42 mm to 0.48 mm for the thorax geometry. Moreover, a similar dose coverage is obtained with refined tetrahedral meshes. As a consequence of the reduction of the number of tetrahedrons, computational time is found to be 25% shorter than both the refined tetrahedral mesh and the voxel-based structure in most cases. Using a coarse tetrahedral mesh to have accurate dose distributions on a given target is feasible as long as the water equivalent path length in the direction of the beam is respected.

Keywords: particle therapy, dosimetry, tetrahedral meshes, Monte Carlo simulation

1 Introduction

Oncological hadron therapy offers a better dose coverage compared to conventional megavolt photon therapy in the treatment of deep-seated local tumors. The particularity of heavy charged particles like protons resides in the fact that they deposit most of their energy at the end of their range, creating the Bragg Peak. This property guarantees a precise irradiation of the target volume and less damage to healthy tissues. The position of the Bragg Peak depends on the beam energy as well as the density and the chemical composition of the traversed mediums. These latter parameters are computed using the Hounsfield Unit (HU) numbers of the CT scan voxels. Current treatment planning systems and dose deposit simulation techniques use voxel representation of tissues. However, a new geometric representation based on tetrahedrons has several advantages compared to voxels. It ensures not only a compact representation of the human body, that can contain structures with different levels of detail, but also a better description of organs compared to voxel-based geometries. At the same time, it has shown high capabilities in deformable anatomy and respiratory motion representation and simulation (Ishikawa et al. 2009, Manescu et al. 2012, Manescu et al. 2014, Han et al. 2015, Touileb et al. 2016). Consequently, tetrahedral geometries are attracting considerable interest in heavy-ion tumor therapy, due to the multiple advantages that they could offer when coupled with Monte Carlo dose calculation technique.

Tetrahedral geometries were first introduced as acceleration structures for surface-based models in Monte Carlo transport codes (Barker, Bird, Serco & Cooper 2008, Barker, Bird & Thetford 2008, Fang 2010, Shen & Wang 2010, Fonseca et al. 2014). In addition to the fact that tetrahedral meshes allow a better approximation of the smooth surfaces, they allow to describe the movement and density distribution of internal tissues easily. Authors in (Poole et al. 2012a, Poole et al. 2012b) have used the tetrahedral mesh generated from a closed tessellated surface to accelerate the geometrical navigation in Geant4 Monte Carlo code (Agostinelli et al. 2003, Allison et al. 2006, Allison et al. 2016). They demonstrated that the navigation time is reduced by two orders of magnitude since the computations are performed only on local tetrahedrons rather than the entire tessellated surface. The same approach was used by (Yeom et al. 2014) to simplify the geometry of a polygonal computational human phantom named PSRK-Man (Chan Hyeong et al. 2011) to create the equivalent tetrahedral-based phantom. They reported a reduction of the computation time by a factor varying from 150 to 832, depending on the particles and their energy. Nevertheless, the simulation time reduction compared to the voxels was less significant and varies from 0.8 to 6.8 times with protons. In a recent study conducted by (Furuta et al. 2017), the authors confronted their implementation of tetrahedral meshes with voxel-based structures using the Monte Carlo code PHITS (Sato et al. 2013). They showed that the computation time of the particle transport simulation using the PSRK-Man tetrahedral version (Yeom et al. 2014) is about four times less than the time required by the voxel grid representation. However, even if the transport calculation time is proven to be shorter in most cases, tetrahedral meshes

still take more time in the geometry loading before performing Monte Carlo simulations (Poole et al. 2012b, Furuta et al. 2017). In fact, for tetrahedrons, the function of the loading time with respect to the number of elements is found to be exponential, but linear for voxels and surface based meshes.

Since the current scanner technology is based on voxel structures providing a unique density value for each voxel, the definition of the densities for the tetrahedral geometries requires mapping algorithms that calculate a density value per tetrahedron from CT-scan data. To use tetrahedral geometries in more realistic clinical applications with patient-specific tetrahedral phantoms, authors in (Ishikawa et al. 2009, Manescu et al. 2012, Manescu et al. 2014, Han et al. 2015, Touileb et al. 2016) have proposed several approaches to map densities from CT-scans to tetrahedral geometries. In (Ishikawa et al. 2009) authors have defined the density value of a tetrahedron as the density of the voxel containing the centroid of the tetrahedron. This method will be referred to as the centroid mapping method (CM) throughout this paper. Moreover, we in (Manescu et al. 2012, Manescu et al. 2014) have proposed to map the densities to the nodes of the tetrahedral mesh instead of its elements, as in finite element analysis. This has the advantage of obtaining a density value for each point inside the mesh with interpolation, and more importantly, preserving the tissues mass since the method is based on the mass conservation principle. Furthermore, we introduced a new technique called mass conservation mapping method (MCM) (Touileb et al. 2016) in which the mass of a tetrahedron is defined as the sum of all the intersecting voxels masses, and the unique density of the tetrahedron is computed as the mass of the tetrahedron per volume. Despite the fact that the mass conservation mapping method (MCM) has shown more accurate dose distributions than the centroid method (CM), its precision depends on the density heterogeneity of the mapped tissues and also to the number of tetrahedrons representing the mesh. The relatively larger volume of tetrahedrons leads to an averaging of the density values of the tetrahedral mesh and consequently to an incorrect dose distribution. Then, on the one hand, it is necessary to have a fine mesh for the precision, and on the other a coarse mesh for the computation time. Moreover, these methods tend to focus on the local density values of the tetrahedrons and ignore the integral of the densities along the beam path laying before the target. This integral is known as the radiological thickness, and it is commonly expressed in terms of water equivalent path length (WEPL). It is used by physicists to calculate the thickness of a water volume in which the ions lose the same amount of energy as they pass through a given tissue. Evidently, the use of CM or MCM with coarser meshes engenders wrong water equivalent path length when compared to WEPL computed using the original CT-images. To overcome this problem, in this paper, we introduce a technique called effective density mapping (EFFD) to minimize the WEPL error in the direction of the beam. This approach not only takes into account the tissues information derived from CT-scans, but also the particle beam parameters, to optimize the dose distribution in a given target while using a coarse tetrahedral mesh. Our final aim is twofold: first, to reconcile the two above mentioned constraints (i.e., time and

precision); and second, adding more freedom in the creation process of patient-specific phantoms with coarse meshes. The paper is organized as follows: first, we describe in detail the water equivalent path length (WEPL) adapted to tetrahedral geometry and then make a mathematical formulation of our proposed scheme. Furthermore, we perform experimentations using a proton beam on a multi-layer phantom as well as a real patient’s thoracic geometry to quantify the performance of our method in Monte Carlo dose computations using Geant4 code. Finally, we give some concluding remarks and the directions for future works.

2 Materials and methods

The knowledge about the density values and the chemical composition of all tetrahedrons is essential for Monte Carlo dose computations. These parameters are calculated using an algorithm that maps the densities from a CT-image to the tetrahedral mesh. Our method consists of calculating an effective density distribution only for the tetrahedrons that intersect the beam. Contrary to MCM and CM that are methods based only on the local approximation of the density in a given tetrahedron and ignore the integral of the density along the beam path, our approach uses this integral to calculate a density map that minimizes the error of the water equivalent path length (WEPL). In this section we will first present the concept of the WEPL, then we formulate the problem to calculate the effective density distribution. Furthermore, the evaluation strategy of our approach is presented alongside the geometries used for the validation.

2.1 Effective Density calculation

2.1.1. Water equivalent path length: The dose distribution inside a given target depends strongly on the density of the tissues traversed by the ion beam and more precisely on the water equivalent path length (WEPL) (sometimes called radiological or water equivalent thickness (WET) (Rietzel et al. 2007, Paganetti 2016). It is an empirical concept that describes the range of ions in matter and is defined as the length of water causing the same energy loss, as it would lose when going through the tissues. The idea is to have the same particle attenuation for the product ($t_{mat} \times \rho_{mat}$) of a given material mat with a thickness t_{mat} and a density ρ_{mat} as the product ($t_w \times \rho_w$) related to water. Therefore, for a single radiation ray r , the WEPL is the integral of the mass densities along the path of the particle and it is defined as follow :

$$WEPL = \int_L \rho(r) dl \quad (1)$$

Where $\rho(r)$ is the linear density function defined on r . To illustrate this concept in 2D, in Figure 1a we associate a line L to the radiation ray. This line depicts the distance between the entrance of the body and the tumor, and it is represented by successive line segments (i.e., $[P1, P2]$ and $[P2, P3]$) describing the thickness of the traversed mediums.

The water equivalent path length of L is the sum of the products $\overline{P1P2} \times \rho(\text{medium1})$ and $\overline{P2P3} \times \rho(\text{medium2})$.

In fact, the mentioned formula in Equation 1 is a simplification and an approximation of the water equivalent path length expression defined in (Newhauser 2001) as :

$WEPL = t_w = t_m \frac{\rho_m \overline{S_m}}{\rho_w \overline{S_w}}$, where t_w and t_m are the thicknesses of water and the target material, respectively. ρ_w and ρ_m are the mass densities of water and the material, respectively. Finally, $\overline{S_w}$ and $\overline{S_m}$ are the mean values of mass stopping power for water and the material, respectively.

The precise calculation of the mean stopping powers of the materials is computationally intensive using iterative numerical methods (Newhauser et al. 2007), and it is therefore not very suitable for some clinical applications (Zhang & Newhauser 2009) particularly for our work since the primary goal is to reduce simulation time. Thus, in this study, the mean stopping powers of the materials are not taken into account. Besides, the density of the water is considered equal to 1 g/cm^3 . Consequently, we obtain the following formula: $WEPL = t_m \rho_m$ for a unique material, and furthermore, we define the WEPL of a medium with multiple materials as the accumulation of all the contributions of their WEPL. The use of our approximate method based on a simple deterministic formula exploits the fact that most thorax tissues have a stopping power ratio close to 1 (between 0.95 and 1.05 (Schaffner & Pedroni 1998)).

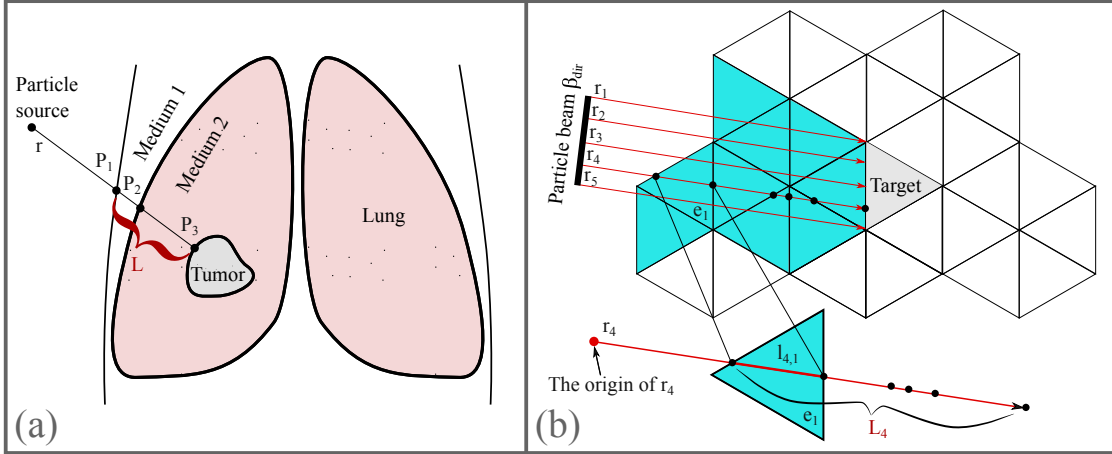


Figure 1: Water equivalent path length (WEPL). (a) L represents the polyline of the ray r . $WEPL(L) = \overline{P1P2} \times \rho(\text{medium1}) + \overline{P2P3} \times \rho(\text{medium2})$. (b) Blue triangles represent the set $\mathcal{I}_{\beta_{dir}}$ of all the tetrahedrons that intersect the beam β_{dir} . The segment $l_{4,1}$ depicts the intersection between the ray r_4 (i.e., the line L_4) and the triangle e_1 .

2.1.2. Effective density map creation process : Starting from the tetrahedral mesh, we first map the densities from the CT-images using the mass conservation mapping method (MCM), then, we only recalculate the density values of the elements that intersect the

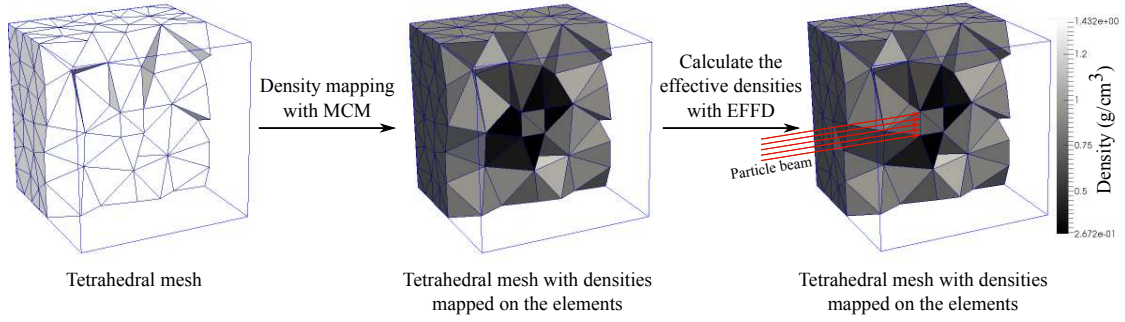


Figure 2: Flowchart of effective density map creation. Notice that the density values of the elements that intersect the beam are changed after the EFFD.

beam using our method called the effective density method (EFFD). Figure 2 illustrates the flowchart of the creation of the effective density map. The effective densities are the density values calculated using our method (EFFD) to replace the values previously calculated with MCM. The mass conservation mapping method is used since it produces better results than CM and also to define the densities of tetrahedrons that do not intersect the beam. It will also be used further to provide an initial guess in the optimization process.

2.1.3. Formulation of the Problem : In this study, we use a straight-line path estimation method to represent the particle trajectory in which we consider the beam β_{dir} as a set of radiation rays extending from the particle source in the direction dir (see Figure 1b). The origins of the rays can be chosen either with equispaced or random sampling methods and they are defined on the surface of the parallel projection of the tumor on the plane of the particle source.

Since we want to respect only the WEPL of the tissues before the tumor, we define for every ray r_i a polyline L_i that goes from the exterior surface to the tumor site.

Given a tetrahedralization \mathcal{T} of a domain \mathcal{D} representing a medium \mathcal{M} , we define the set of all the elements in intersection with \mathcal{T} as:

$\mathcal{I}_{\beta_{dir}} = \left\{ \bigcup_{k=0}^n e_k \mid e_k \in \mathcal{T} \cap \beta_{dir} \right\}$, where $\beta_{dir} = \left\{ \bigcup_{i=0}^m L_i \right\}$, n is the number of elements of \mathcal{T} that intersect β_{dir} , m is the number of radiation rays representing β_{dir} and e_k is a tetrahedron in intersection with the beam β_{dir} .

Based on Equation 1 we define the water equivalent path length of a given polyline L_i as :

$$WEPL(L_i) = \int_{L_i} \rho(r_i) dl \quad (2)$$

Knowing that the polyline L_i is characterised by a sequence of line segments $(l_{i,1}, \dots, l_{i,s})$ representing the intersection with $\mathcal{I}_{\beta_{dir}}$ (see Figure 1b), we redefine the WEPL as follow:

$$WEPL(L_i) = \sum_{j=0}^s \rho_{eff}(e_j) \times l_{i,j} \quad (3)$$

Where s is the number of elements of $\mathcal{I}_{\beta_{dir}}$ that intersect L_i , e_j is a tetrahedron from $\mathcal{I}_{\beta_{dir}}$ that intersects L_i and ρ_{eff} is the effective density function defined on $\mathcal{I}_{\beta_{dir}}$ as:

$$\rho_{eff}: \begin{cases} \mathcal{I}_{\beta_{dir}} \rightarrow \mathbb{R} \\ e_j \mapsto \rho_{eff}(e_j) \end{cases}$$

ρ_{eff} represents the biased values of densities that aims to replace the genuine function ρ_{mcm} (calculated with the mass conservation mapping method) on $\mathcal{I}_{\beta_{dir}}$. The aim of this work is to calculate ρ_{eff} for the elements e_k of $\mathcal{I}_{\beta_{dir}}$. It is worth mentioning that the density ρ_{eff} is only defined on $\mathcal{I}_{\beta_{dir}}$ contrary to ρ_{mcm} that is defined on all the domain \mathcal{D} . The main idea is to define the ρ_{eff} by minimizing the WEPL error between the reference density map ρ_{CT} of the 3D CT image and the effective density $WEPL_{eff}$. Then, replace ρ_{mcm} by ρ_{eff} in $\mathcal{I}_{\beta_{dir}}$. Therefore, we define our linear system as follow: $Ax = b$

$$\text{Where } A = \begin{pmatrix} l_{1,1} & l_{1,2} & \cdots & l_{1,n} \\ l_{2,1} & l_{2,2} & \cdots & l_{2,n} \\ \vdots & \vdots & \ddots & \vdots \\ l_{m,1} & l_{m,2} & \cdots & l_{m,n} \end{pmatrix}, x = \begin{pmatrix} \rho_{eff}(e_1) \\ \rho_{eff}(e_2) \\ \vdots \\ \rho_{eff}(e_n) \end{pmatrix} \text{ and } b = \begin{pmatrix} WEPL_1 \\ WEPL_2 \\ \vdots \\ WEPL_m \end{pmatrix}$$

l_{ij} : is the length of the line segment of the intersection between the line L_i and an element e_j . $WEPL_i$ is the water equivalent path length calculated using the reference CT image. Solving this system outputs the vector x of the effective density values of ρ_{eff} that need to be assigned to each tetrahedron of the mesh.

The fact that $m > n$ makes the system overdetermined since we have more rays than elements in the intersection with the beam. This implies that there is no unique solution that satisfies this equation system. Additionally, we need to ensure that the resulted densities are in the range of human tissues densities (i.e., between 0 gm^3 and 2.79 gm^3). To solve a sparse overdetermined linear system with linear constraints we have calculated an optimized solution using a constrained quadratic programming approach of the form (Cornuejols & Tütüncü 2006):

$$\text{QP} \left| \begin{array}{l} \text{minimize } \frac{1}{2}x^T Hx + c^T x \\ \text{subject to: } Ax = b \\ lb \leq x \leq ub \end{array} \right.$$

H: the quadratic matrix ($n \times n$) defined as $H = A^T A$, x: the vector of decision variables ($n \times 1$) that represents the unknown-density-values vector of ρ_{eff} , c: vector of linear objective function coefficients ($n \times 1$), defined as $c = -A^T b$, and finally lb and ub represents respectively the lower and the upper bounds applied to density values. Besides, an initial guessing of the solution x_0 containing the densities calculated using ρ_{mcm} is given to the solver to improve the convergence of the solution. Furthermore,

in order to solve the optimization problem, we used the interior-point-convex algorithm described in (Gould & Toint 2004, Altman & Gondzio 1999) since it is suited for sparse quadratic programs and also for its faster optimization time compared to other methods.

2.2 Evaluation strategy and criteria

We define two case studies in order to quantify the performance of our proposed scheme, a multi-layer phantom (MLP) and a thorax geometry. The strategy employed to generate the tetrahedral mesh consists of using only the external surface of the phantom and the tumor (i.e., the target) in the tetrahedralization algorithm. This approach applies fewer constraints on the algorithm and can be used to decrease the number of elements significantly. It also provides more possibilities to the user to control the volume of the tetrahedrons. By adopting our density mapping method (EFFD) for a coarse mesh, we will investigate its performance comparing to the centroid mapping method (CM) and the mass conservation mapping method (MCM) using tetrahedral meshes with multiple resolutions. More specifically, we evaluate the water equivalent path length (WEPL) then the dose accuracy with respect to the voxel-based representation which is considered as our ground truth. Finally, the computation time will be investigated for all scenarios.

2.2.1. Water equivalent path length accuracy: To study the accuracy of the water equivalent path length of the particle beam, we define the mean absolute error of WEPL (MAEW), the mean error of WEPL (MEW) and the mean relative error of WEPL (MREW) as: $MAEW = \frac{\sum_{i=0}^m |WEPL_i(CT) - WEPL_i(\mathcal{T})|}{m}$, $MEW = \frac{\sum_{i=0}^m WEPL_i(CT) - WEPL_i(\mathcal{T})}{m}$ and $MREW = \frac{\sum_{i=0}^m |WEPL_i(CT) - WEPL_i(\mathcal{T})| / WEPL_i(CT)}{m}$. Where $WEPL_i(CT)$ and $WEPL_i(\mathcal{T})$ are the water equivalent path length of the line L_i calculated using the CT image and the tetrahedral mesh \mathcal{T} , respectively. m is the number of lines representing the beam. To have a more precise depiction of the WEPL errors, we also define the errors histogram of all the lines.

2.2.2. Dose distribution: To investigate dose homogeneity and uniformity in the target volume, we converted dose distributions into 2D cumulative dose-volume histograms (CDVH). These curves give the percentage of volume that receives more than a certain amount of dose within a defined volume or organ. Besides, they allow to define parameters like maximum dose (D_{max}), minimum dose (D_{min}) and mean dose (D_{mean}) alongside with homogeneity index $HI = \frac{D_5}{D_{95}}$, where D_5 and D_{95} are respectively the minimum dose of 5% and 95% of the target volume. The ideal value of HI is 1, and it increases as the distribution becomes less homogeneous (Kataria et al. 2012). Furthermore, gamma index distributions (Low et al. 1998) were also considered to highlight the regions where the dose deviations are concentrated.

2.2.3. Computational performance: The computation speed is expressed by the structure loading time (t_L) and the simulation time (t_S). The former is the time needed to define the materials and to load the geometry by creating a single *G4Tet* object for every tetrahedron in Geant4, add it to a *G4AssemblyVolume*, then make an imprint of it in the user detector geometry. This time is correlated to the number of the elements of the tetrahedral mesh. On the other hand, the simulation time depicts the time required to simulate the transport of all the particles in Monte Carlo code. In this work, the simulations were carried out on a desktop personal computer with an Intel Core i5 3.2 GHz CPU and a 16 Gb RAM.

2.3 Geometries of interest and simulation setups

2.3.1. Multi-layer phantom: The multi-layer phantom (MLP) is defined as a cube containing four concentric, homogeneous cubic shells of tissue (see Figure 3): Tumor, lung, bone, and muscle tissues from the inside to the outside of the phantom. The composition and the mass density of the used materials are taken from the International Commission on Radiation Units and measurements (White et al. 1992). The inner cube is considered as the target, and it has a tumor density of 0.96 g/cm^3 . The voxel-based structure of the MLP consists of $224 \times 224 \times 224$ voxels with the resolution of $1 \times 1 \times 1 \text{ mm}^3$. Since that the primary source of tissues properties is the voxel-based structure (in which voxel values represent the density of the tissues in the multi-layer phantom), we use our previously published method (Touileb et al. 2016) to create the tetrahedral geometry and its corresponding density map. Therefore, we tetrahedralize the volume between the external surface of the phantom and the inner cube (i.e., the target) using the Tetgen software (Si 2010, Si & Gärtner 2015). The latter is based on the constrained Delaunay tetrahedralization method (CDT) that can generate meshes with different resolutions by applying an upper bound on the volume of the tetrahedrons. Finally, the mass densities are mapped from the voxels to the elements of the tetrahedral meshes. Hence, we create a single density value per tetrahedron that is used for Monte Carlo particle transport simulations. Two different density mapping methods are investigated in this study along with our method (i.e., EFFD) to test their respective performances: Mass conservation mapping (MCM) and centroid mapping (CM). Furthermore, Figure 4a illustrates the configurations used for the MLP in which three levels of detail are used for MCM and CM and a coarse resolution for the EFFD. Moreover, the corresponding histograms of the volume of tetrahedrons are plotted in Figure 4b. For Geant4 simulations, a passive scattering system was used to generate a spread-out Bragg peak (SOBP) that covers the entire target volume. Hence, six virtual proton sources with an energy of 270 MeV were placed inside a water envelope at different depths to shift their range (see Figure 4c). Moreover, the sources are weighted proportionally to the relative number of protons to generate the desired SOBP. This simplified beam simulation replaces the range modulator wheel containing absorbers of variable thickness that modulates the depth penetration of the beam. Finally, the same

particle beam configuration is maintained through all the simulations regardless of the structure of the phantom. To show the efficiency of our approach and for the sake of computational cost, we chose only 49 (7×7) rays, uniformly distributed on the source surface. In this case, the absolute error of WEPL was 0.62 mm, improving significantly the error calculated with both CM and MCM methods (see. Table 1). Additionally, Figures 5a and 5b illustrate, respectively, the absolute error of WEPL versus the number of rays, and the behavior of the absolute error of WEPL over the time needed to calculate the intersection of the rays with the mesh and to define the equation system.

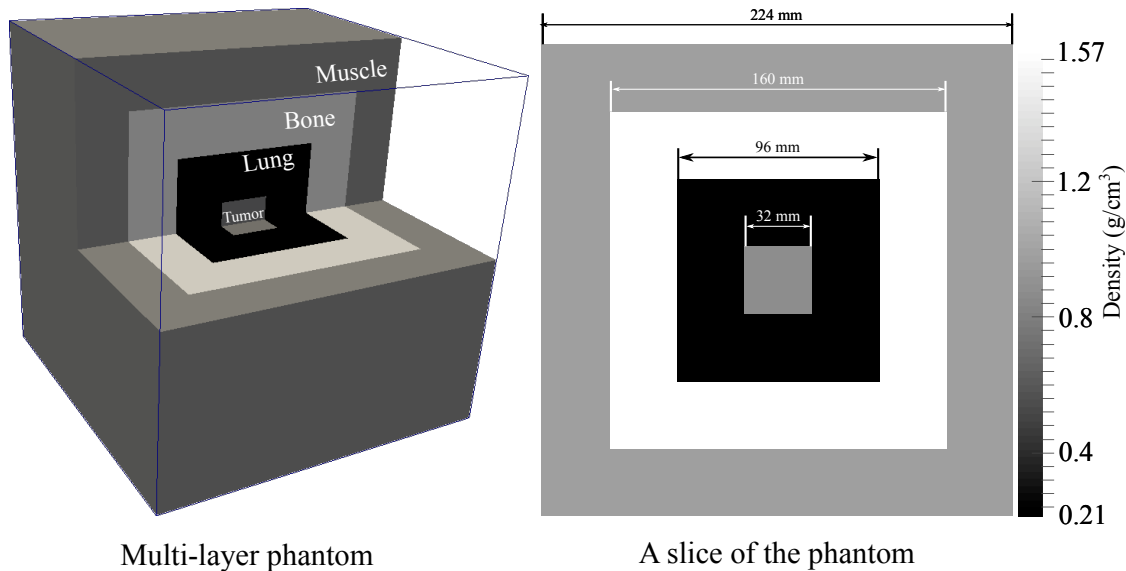
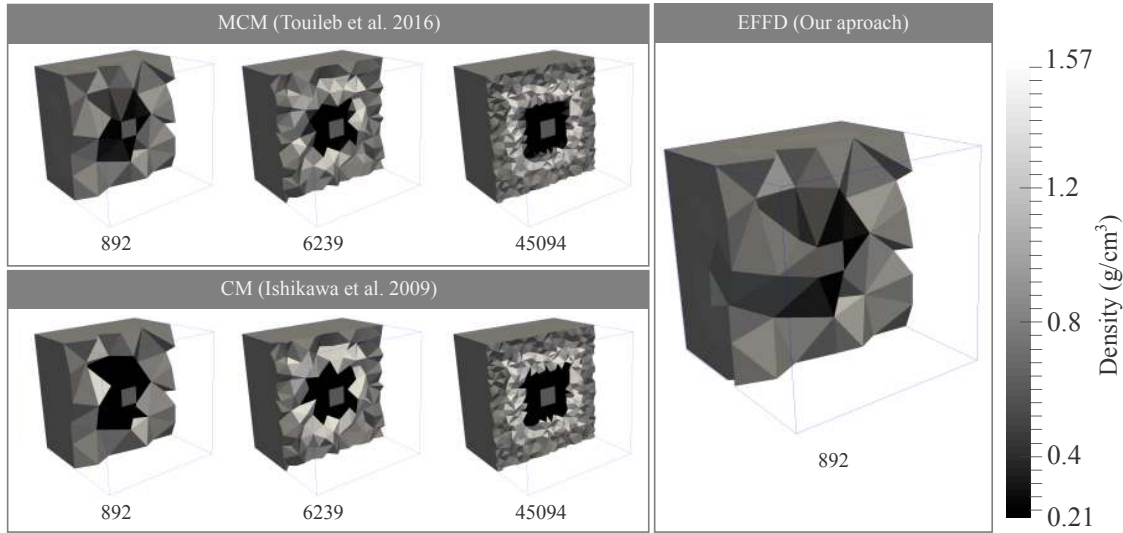
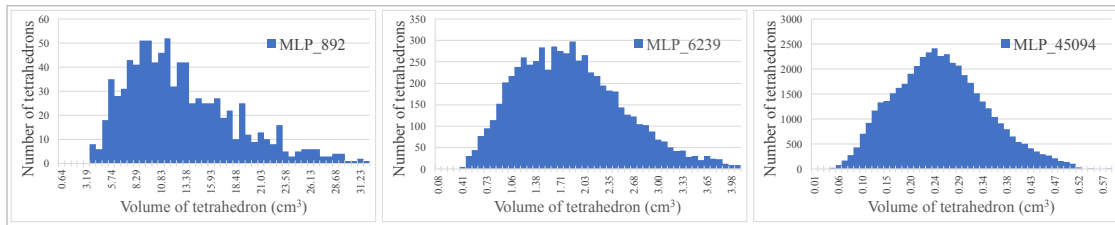


Figure 3: The Multi-layer phantom (MLP). Four different homogeneous shells of tissue are used : tumor, lung, bone and muscle (from the inside to the outside). The density values and the material composition of these tissues are issued from (White et al. 1992).

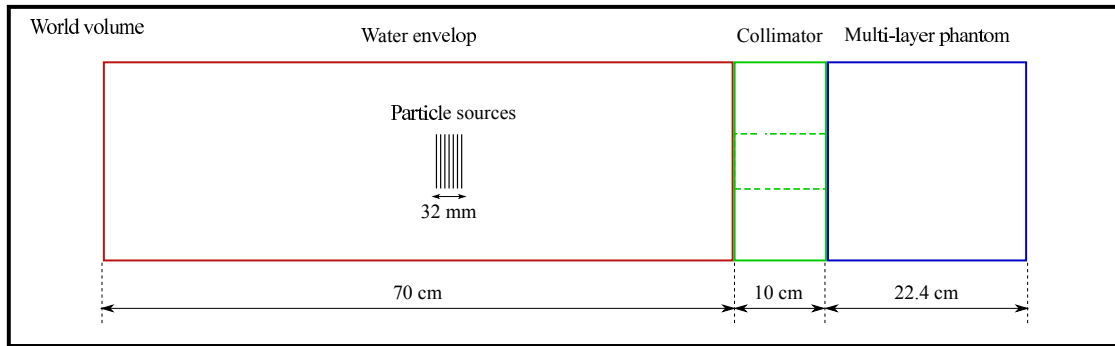
2.3.2. Human thorax geometry: We have equally considered a real patient case with a CT-scan issued from the dir-lab database (Castillo et al. 2010). The voxel resolution of the CT images is $0.97 \times 2.5 \times 0.97 \text{ mm}^3$ and their number is $512 \times 128 \times 378$. They are represented by a voxel map of linear X-ray attenuation coefficients of different tissues, in which voxel values are scaled such that the linear X-ray attenuation coefficient of air equals -1000 and that of water equals zero. This scale is the Hounsfield scale with the HU unit. Authors in (Schneider et al. 2000) present a method to convert Hounsfield values into tissue parameters (mass density and chemical composition) needed for dose calculations in particle therapy. The flowchart of the creation of the patient-specific tetrahedral model is depicted in Figure 6. The images are firstly preprocessed by thresholding the image intensities, then the organs of interest are segmented using the *snake evolution* method (Kass et al. 1988) based on active contours. Further on, these surfaces are converted into tetrahedral meshes using the same approach described in section 2.3.1.



(a)



(b)



(c)

Figure 4: Multi-layer phantom tetrahedral (MLP) (a) MLP configurations used in Monte Carlo simulations. The tetrahedral model is constructed using the surface of the tumor and the external surface of the phantom. Three levels of detail are used for the mass conservation mapping method (MCM) and the centroid method (CM) with 892, 6239 and 45094 tetrahedrons, respectively. One level of detail with 892 tetrahedrons is used for EFFD. (b) histograms of the volume of tetrahedrons used in MLP with 892, 6239 and 45094 tetrahedrons. (c) The configuration of the detectors for Geant4 simulation. The same configuration is used for voxel and tetrahedral representations.

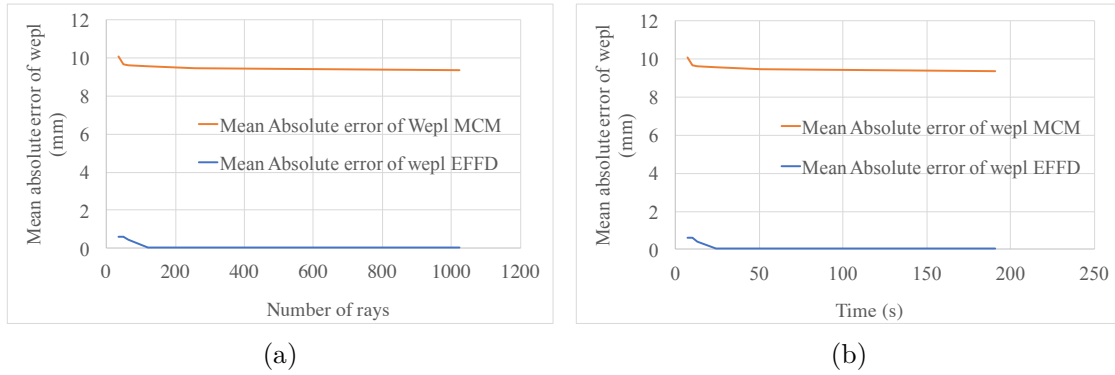


Figure 5: (a) Mean absolute error of WEPL versus the number of rays calculated for the MLP (with 892 tetrahedrons) using both MCM and EFFD. (b) Mean absolute error of WEPL versus the time needed to calculate the intersection of the rays with the mesh and to define the equation system.

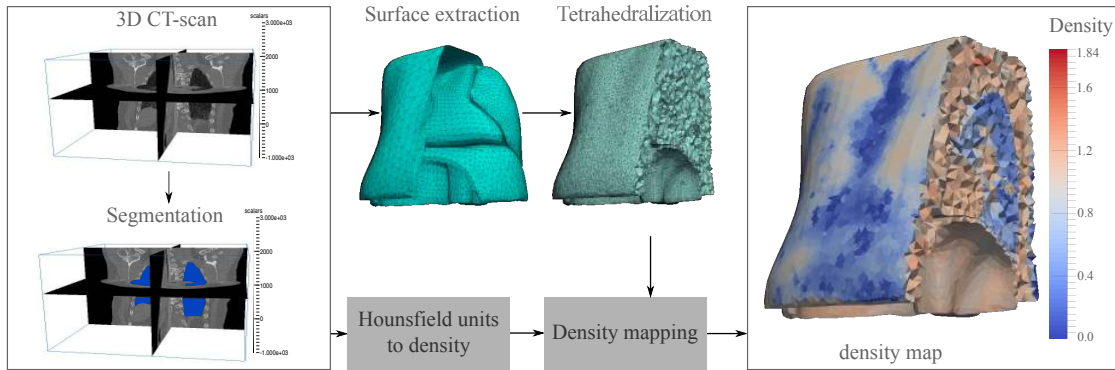
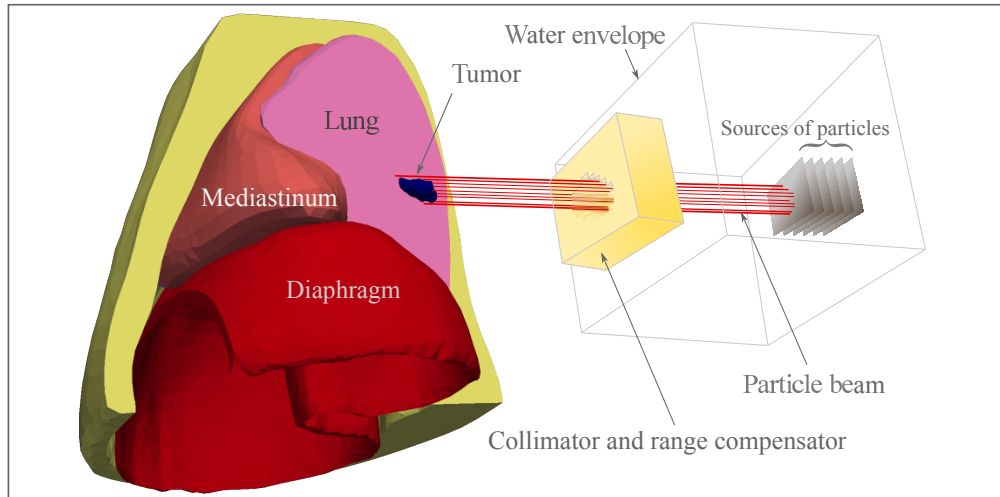
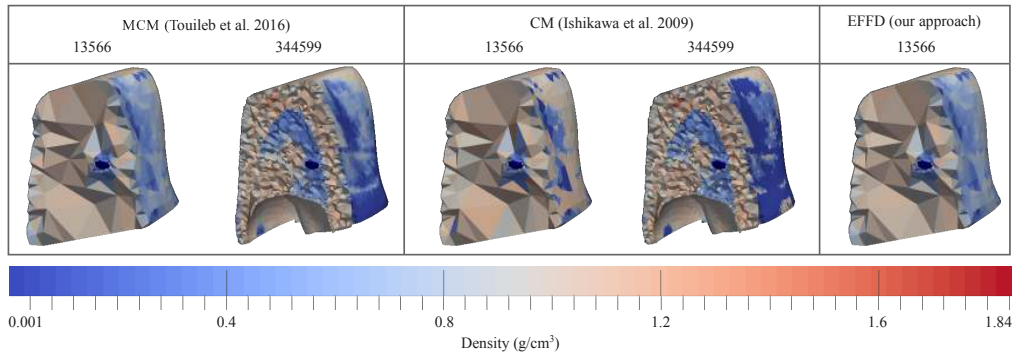


Figure 6: Flowchart of tetrahedral model construction: from 3D-CT to tetrahedral model. The CT images are first converted into voxelized mass density maps which are then mapped to the tetrahedral elements of the meshes.

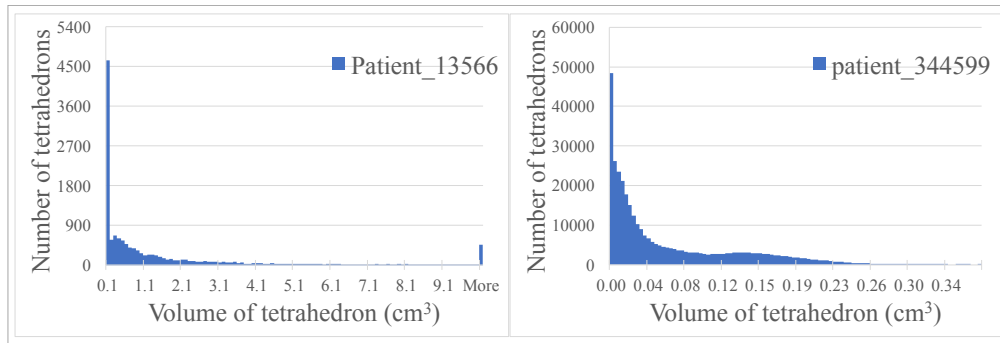
To take into account the shape of the tumor in hadrontherapy beam line simulation and to improve the efficiency of treatment delivery, we have defined a patient-specific range compensator and a multileaf collimator (see Figure 7a). These devices are used in passive scattering to shape the beam and to minimize the delivery dose in organs at risk (OAR). Moreover, a spread-out Bragg peak (SOBP) is achieved by using six particle sources placed inside a water box to shift their range, each one of them generates a Bragg Peak with a different number of particles. In a similar way to the MLP, we compare the EFFD method applied to a coarse mesh (constructed only with the tumor and the external surfaces) to the mass conservation method (MCM) and the centroid method (CM) by using both the same coarse mesh and a finer mesh. The latter is created by segmenting not only the tumor but also the lungs, the diaphragm, and the mediastinum. Figure 7b illustrates the configurations used for Monte Carlo simulations for the patient case for both the coarse mesh with 13566 tetrahedrons and the fine mesh



(a)



(b)



(c)

Figure 7: Thorax geometry. (a) The passive scattering beam line configuration used for Monte Carlo simulation of the thorax geometry. (b) tetrahedral configurations used for dose evaluation. The coarser meshes with 13k tetrahedrons are constructed using only the segmentation tumor volume and the surface of the thorax. However, the refined meshes with 344k are constructed using the segmentation of the diaphragm, the mediastinum, the lungs, the tumor and the external surface. (c) histograms of the volume of tetrahedrons used in the patient case with 13566 and 344599 tetrahedrons.

with 344599 tetrahedrons. Furthermore, the corresponding histograms of the volume of tetrahedrons are illustrated in Figure 7c. The particle beam used for the patient case is represented by 1243 randomly arranged lines distributed on the surface of the particle source. This strategy of choosing the position of the lines is adopted since it is simpler to implement and it is more suited for nonuniform shapes as in the case of the tumor. Besides, the number of lines has been chosen as it generates a reasonable mean absolute error of WEPL (i.e., 0.48 mm) and presents some gain in computation time. We would also like to point out that increasing the number of lines will eventually decrease the error.

2.3.3. Geant4 configuration details: In this work, all the Monte Carlo dose calculation results relative to the proton beams, have been obtained using The geant4.9.5.P02 version and the *QGSP_BIC_EMY* reference Physics Lists. The latter has been designed for any applications required higher accuracy of electrons, hadrons, and ion tracking. Additionally, it is recommended for use in medical applications. For the range cut of all particles in all regions, a cut-off value of 0.1 mm was used alongside a step size limit of 0.1 mm to ensure a precise simulation. These values were chosen as they are below the thickness of the mean volume of all the tetrahedrons. We would also like to point out that, the simulation time can be further improved if a production threshold of 1 mm is used (as recommended in (Zahra et al. 2010)). However, the accuracy regarding spatial dose distribution will not be ensured for all the tetrahedral geometry.

3 Results and discussion

As stated in section 2.2, our primary purpose is to investigate the performance of the effective density mapping method by evaluating the water equivalent path length accuracy and analyzing its impact on dose distribution. In the case of the multi-layer phantom, we used a particle beam containing 49 lines that intersect a total of 28 tetrahedrons to construct our effective density map on a tetrahedral mesh with 892 elements. Table 1 presents the mean absolute error of WEPL (MAEW) generated using; first, MCM and CM methods applied to three different mesh resolutions (892, 6239 and 45094), then, EFFD approach only on the coarser mesh (i.e., 892). The results show that the MAEW of all the lines has been reduced to 0.62 mm using the EFFD compared to the other methods, where the minimum error that can be obtained is 1.41 mm using MCM on the finest mesh with 45094 elements. For the same resolution as used for EFFD (i.e., 892), the mean absolute errors are approximately 9 mm and 16 mm for MCM and CM, respectively. Besides, the distribution of the absolute errors of WEPL of individual lines is depicted in Figure 8a. A similar behavior was observed with the thorax geometry in which the MAEW was decreased to 0.48 mm using the EFFD with a tetrahedral mesh containing only 13566 elements (see table 1). In this case, the effective density was calculated for 754 tetrahedrons that intersect the beam represented by 1243 lines. Moreover, the histogram of these lines is illustrated in Figure 9a as well as the

histograms generated using the MCM and the CM methods for both the coarse mesh with 13566 tetrahedrons and the fine mesh with 344591 elements. The histogram of the EFFD tends to have a similar distribution, as the fine meshes of MCM and CM in which most of the values are concentrated between 0 and 1.5 mm.

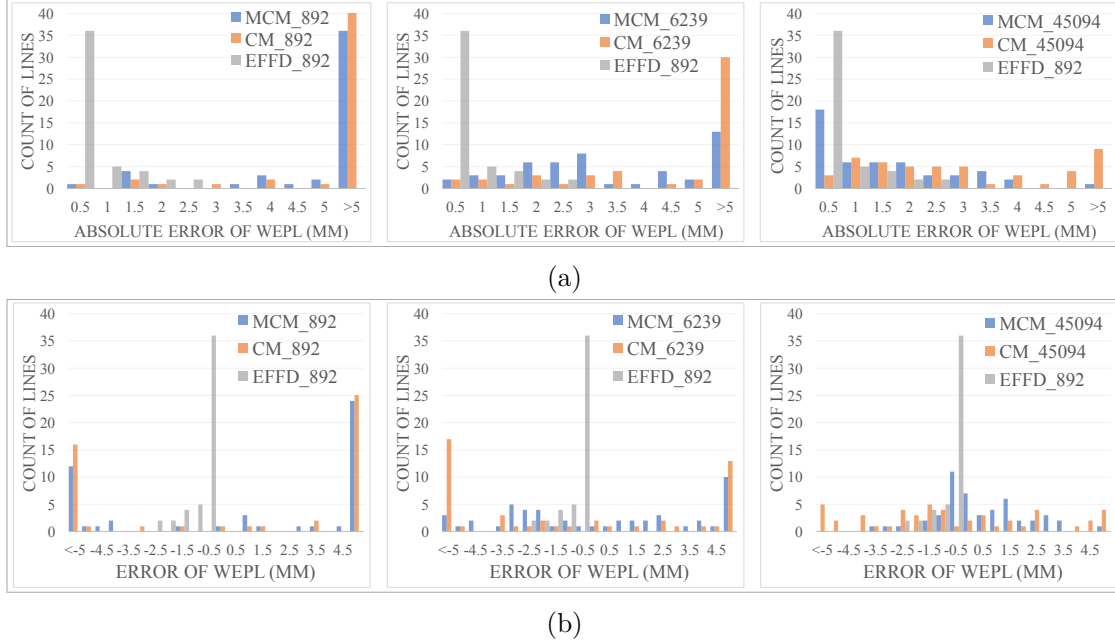


Figure 8: Histograms of WEPL errors calculated using the multi-layer phantom. Histograms of the absolute error (a) and the error (b) of WEPL for 49 lines representing the beam. Three resolutions of the tetrahedral mesh (i.e., 892, 6239 and 45094) are used alongside the centroid method (CM) and the mass conservation method (MCM).

As regards dose accuracy, table 2 shows the statistical analysis of the 3D dose maps of tetrahedral meshes obtained for different simulations. Even though the analysis of the mean dose did not show a significant difference between different simulations since the global mass of the target is more or less respected, the HI is found to be different and correlated to the MAEW. Consequently, the EFFD distribution shares approximately the same HI as the voxel-based structure and the fine meshes of MCM and CM. However, in the case of coarser meshes, it behaves better compared to MCM or CM techniques. Furthermore, the CDVH of the gross target volume of the thorax geometry presented in Figure 10 gives a more clear depiction of the homogeneity of the deposited dose and shows how the histogram of EFFD has almost the same shape as the reference voxel-based phantom. To outline the dose distributions, a series of isodose lines were generated in figures 11 and 12 for a sagittal and an axial slices, respectively. Additionally, gamma distributions calculated using a gamma criteria of 3% and 3 mm, are illustrated in Figure 12 for an axial slice.

It can reasonably be suggested that the sign of the mean error of WEPL (see table. 1) indicates if the Spread Out Bragg peak has shifted forward or backward relative to its

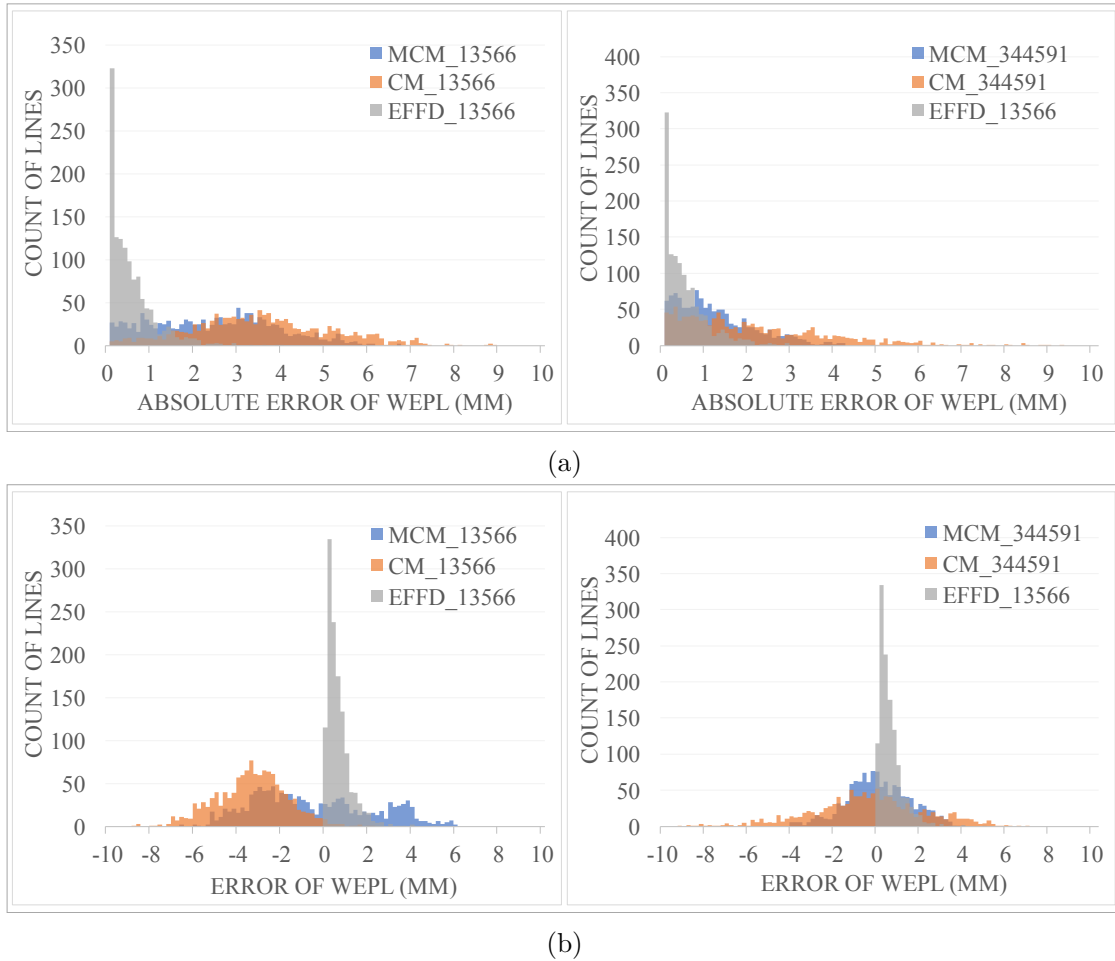


Figure 9: Histograms of WEPL errors for the patient case using 1243 lines representing the beam. (a) and (b) are respectively the histograms of the absolute error and the error of WEPL of the tetrahedral meshes containing 13566 and 344591, respectively.

original position calculated using the reference voxel-based structure. For instance, as the MEW of the MCM is positive and equal to 2.89 mm , in the MLP with 892 elements, the beam will go further away from the target. Besides, a shift in the 90% isoline is perceived before reaching the target in the case of MCM and CM for 13566 tetrahedral meshes. It indicates that the beam started to deposit the dose before reaching the tumor. It also confirms our findings on the direction of the shift as a function of the sign of the MEW.

Figures 8b and 9b illustrate the Mean error of WEPL for both the multi-layer phantom and the thorax geometry. Further analysis on the tetrahedral meshes showed that the relative error of the mass of the tetrahedral mesh compared to the voxel-based structure is about 0.02% in EFFD. This negligible value is about the same for all mesh resolutions using MCM or CM. Overall, the WEPL gives a more relevant tool for comparing density mapping methods.

Phantom	Density mapping algorithm	Number of tetrahedrons	Mean absolute error of WEPL (mm)	Mean error of WEPL (mm)	Mean relative error of WEPL (%)	
Multi-layer phantom	MCM	892	9.65	2.89	10.59	
		6239	3.83	1.16	4.21	
		45094	1.41	0.72	1.55	
	CM	892	16.57	3.09	18.2	
		6239	7.97	-0.36	8.75	
		45094	2.86	-0.59	3.14	
	EFFD	892	0.62	-0.62	0.74	
		MCM	13566	2.42	-0.66	5.29
			344599	1.18	-0.05	2.59
Thorax geometry	CM	13566	3.48	-3.46	7.73	
		344599	2.07	-0.53	4.52	
	EFFD	13566	0.48	0.48	1.05	

Table 1: Mean absolute error of WEPL (MAEW), mean error of WEPL (MEW) and mean relative error of WEPL (MREW) of the Multi-layer phantom and the thorax geometry using MCM (Touileb et al. 2016), CM (Ishikawa et al. 2009) and EFFD (our approach) algorithms.

Table 3 summarizes the computation times obtained for the Monte Carlo simulations carried out on the Multi-layer phantom and the thorax geometry using 12 million protons with an energy of 270 *MeV*. We denote the simulation, the loading and the total computation times by t_S , t_L and t_T , respectively (see definitions in 2.2.3). First, our experiments confirm that the t_S of all tetrahedral geometries is less than the t_S of the voxel-based structure. Nevertheless, the t_T can in some cases be more due to the higher value of the t_L , in particular for the finer thorax tetrahedral mesh with 344k elements where its t_L exceeds the t_L of the reference by an hour and a half. The use of the EFFD with the coarser mesh divides this time (i.e., t_L) by a factor of six hundred resulting with a t_L of 9 seconds and a total time of six hours. The use of fewer elements also decreases the t_S significantly; it can be reduced to two hours and a half in the case of the MLP, and to forty minutes for the thorax geometry. It is worth mentioning that the significant difference in the simulation time between the two reference voxel-based models is because the tumor in the multi-layer phantom is deeper than the one in the thorax geometry. They are respectively located at a depth of 96mm and 40 mm. Therefore, more geometrical and physical steps are needed to calculate the energy deposition for the Multi-layer phantom.

Although our approach has shown promising results, it is necessary to point out that

Phantom	Density mapping algorithm	Number of elements	D_{mean}	D_{min}	D_{max}	HI
Voxel-based MLP	-	1123942	35.19	28.69	42.21	1.18
MLP tetrahedral mesh	MCM	892	33.76	2.36	42.23	1.38
		6239	34.96	26.47	43.60	1.24
		45094	35.18	26.08	43.26	1.22
	CM	892	30.80	0.87	43.77	2.65
		6239	33.85	8.22	43.91	1.35
		45094	35.17	25.85	44.07	1.23
	EFFD	892	35.78	25.31	45.80	1.23
Voxel-based thorax phantom	-	11025375	54.83	41.37	62.20	1.27
Thorax tetrahedral mesh	MCM	13566	55.0	41.37	62.0	1.22
		344599	54.97	41.62	64.46	1.27
	CM	13566	54.97	34.45	69.77	1.22
		344599	54.16	43.09	63.98	1.27
		EFFD	13566	54.10	41.78	63.49

Table 2: Evaluation of dose distribution in the tumor volume of the multi-layer phantom and the thorax geometry. D_{min} , D_{max} , D_{mean} are respectively the minimum, the maximum and the mean dose deposited. HI is the Homogeneity index.

when the number of tetrahedrons is high, the creation of the system and the calculation of the solution can be very time-consuming. This issue can be addressed by using line-tetrahedron intersection acceleration algorithms like in (Marmitt & Slusallek 2006). It will also be interesting to investigate if our method will maintain the same outcomes on a more heterogeneous medium that involves a significant mix of bone tissues. Even though, at least for the thorax, it seems that the results are accurate and satisfying for dose calculations.

To take full advantage of tetrahedral geometries, a motion compensated version of this algorithm can be investigated; we believe that it can significantly reduce computation time in 4D simulations. As stated in (Han et al. 2015), their 4D tetrahedral phantom performs 40 times slower than the voxel 4D implementation. This statement indicates that there is still room for improvement in deformation simulations.

Finally, we believe that our region-of-interest method can not only produce accurate results in dose calculations but also provides a patient-specific phantom construction method that can simplify the treatment planning in a real clinical environment.

Phantom	Density mapping algorithm	Number of elements	Loading time (s)	Simulation time (s)	Total time (HH:MM:SS)
Voxel-based MLP	-	11239424	377.079	48490.1	13:34:27
MLP tetrahedral mesh	MCM	892	0.0156	23538	6:32:18
		6239	0.4652	27831.6	7:43:52
		45094	34.2065	32096.5	8:55:31
	CM	892	0.0155	23579	6:32:59
		6239	0.2817	26936.4	7:28:57
		45094	34.7164	32345.8	8:59:41
	EFFD	892	0.01471	23182.9	6:26:23
Voxel-based thorax phantom	-	11025375	313.853	27408.9	7:42:03
Thorax tetrahedral mesh	MCM	13566	9.67524	21582.4	5:59:52
		344599	5769.45	23294.4	8:04:24
		45094	34.2065	32096.5	8:55:31
	CM	13566	8.23905	21426.1	5:57:14
		344599	6362.28	23829.8	8:23:12
		45094	34.2065	32096.5	8:55:31
	EFFD	13566	9.86269	21768	6:02:58

Table 3: Loading and simulation time of the Multi-layer phantom (MLP) and the thorax geometry using 12×10^6 protons in Monte Carlo simulations. Time is reported in seconds (s) or in hours:minutes:seconds (HH:MM:SS).

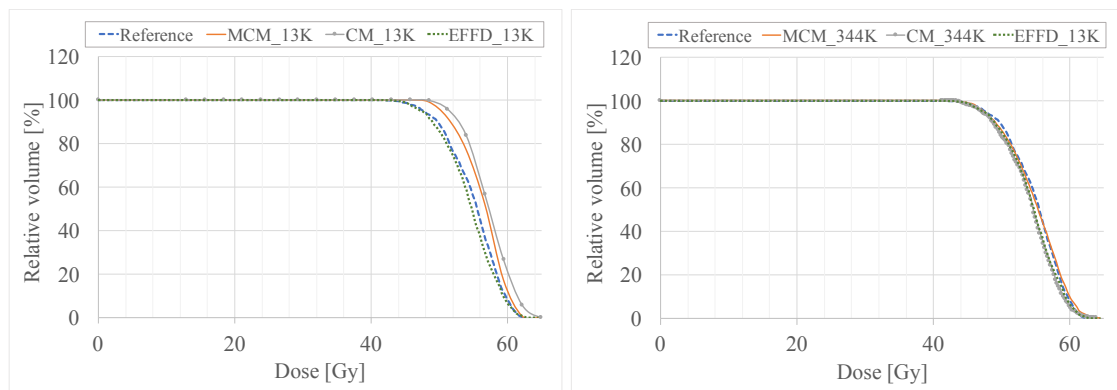


Figure 10: Cumulative dose volume histogram of the gross tumor volume (GTV) of the thorax geometry using MCM, CM and EFFD. Left: coarse mesh with 13k tetrahedrons is used. Right: a refined mesh with 344k is used for MCM Touileb et al. 2016, CM Ishikawa et al. 2009.

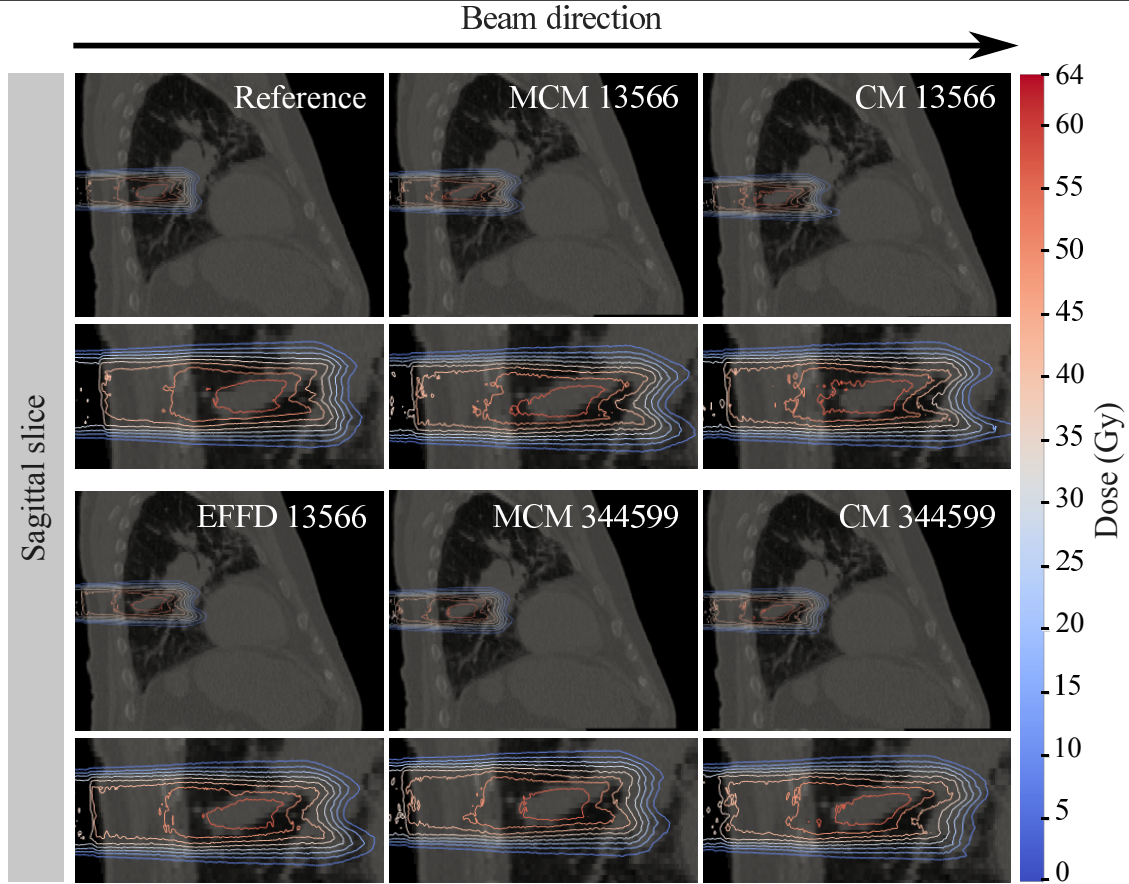


Figure 11: IsoDose of a sagittal slice of patient case . Isolines are from the inside to the outside: 90%, 78%, 68%, 57%, 46%, 36%, 25% and 15% of dose max.

4 Conclusion

In this paper, we have presented a new method for dose computations using tetrahedral geometries, which employs particle beam parameters (i.e., direction and shape) in the density mapping algorithm. Thus, by calculating an effective density map that minimizes the error of the water equivalent path length of the beam rays. This approach aims at providing a precise dose distribution in a given target using a simplified geometry, resulting in a significant decrease of tetrahedral elements. Monte Carlo transport simulations with 270 MeV proton particle beam, were performed for a cubic multi-layer phantom and a thorax geometry. Furthermore, the computational performance and dose accuracy were examined for both cases in comparison to the voxel-based phantom constructed with the CT-images. The use of our target-oriented technique in dose computations can reduce both the transport and the loading time of tetrahedral geometries since in clinical practice; the physicians are interested in a limited set of organs at risk and the tumor. This work can be extended and optimized to handle more volumes other than the tumor, like the organs at risk (OAR). Besides, a motion

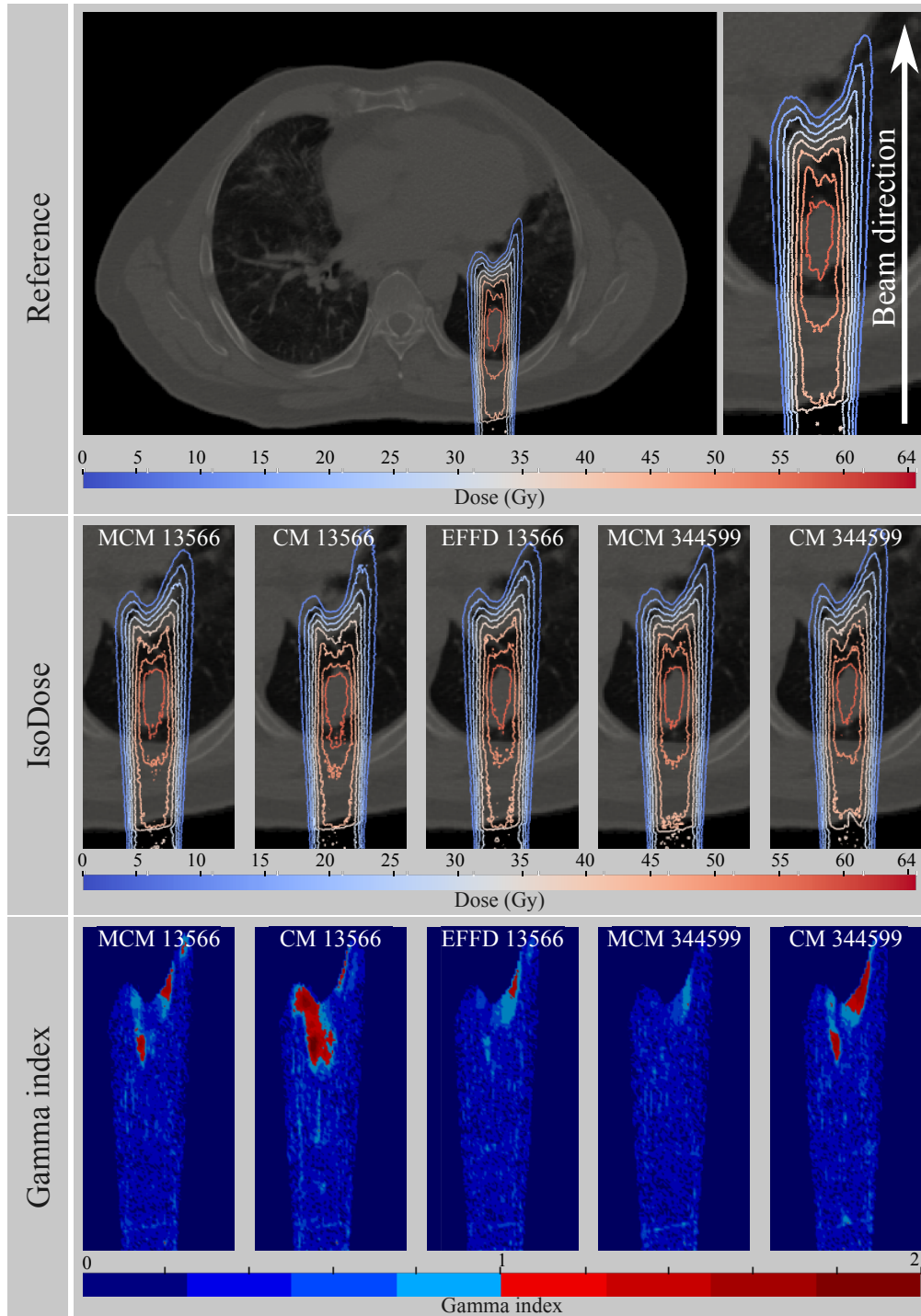


Figure 12: IsoDose and gamma index evaluation (DTA=3 mm and dose tolerance = 3%) of an axial slice of the patient case. Isolines are from the inside to the outside: 90%, 78%, 68%, 57%, 46%, 36%, 25% and 15% of dose max. The regions that fail the criteria in the gamma evaluation are clearly identified where gamma index > 1.

compensated version can be investigated to take into account the deformation of the phantom and the density variation over the breathing phases in the case of lung cancer. The creation of patient-specific tetrahedral phantoms can take less time by adopting our approach since the definition of the density map doesn't mainly rely on the resolution of the mesh.

Acknowledgments

This research is supported by LABEX PRIMES (ANR-11-LABX-0063), within the program Investissements d'Avenir(ANR-11-IDEX- 0007) and by France Hadron, and by ClaRys project CNRS, defis Imaging.

References

- Agostinelli S, Allison J, Amako K & Others 2003. Geant4 – a simulation toolkit *Nucl. Instruments Methods Phys. Res. A* **506**(506), 250–303.
- Allison J, Amako K, Apostolakis J, Araujo H, Dubois P A, Asai M, Barrand G, Capra R, Chauvie S, Chytracsek R & Others 2006. Geant4 developments and applications *IEEE Trans. Nucl. Sci.* **53**(1), 270–278.
- Allison J, Amako K, Apostolakis J, Arce P, Asai, M and Aso T, Bagli E, Bagulya A, Banerjee S, Barrand G & Others 2016. Recent developments in Geant4 *Nucl. Instruments Methods Phys. Res. Sect. A Accel. Spectrometers, Detect. Assoc. Equip.* **835**, 186–225.
- Altman A & Gondzio J 1999. Regularized symmetric indefinite systems in interior point methods for linear and quadratic optimization *Optim. Methods Softw.* **11**(1-4), 275–302.
- Barker T, Bird A, Serco R T & Cooper A 2008. Use of Tetrahedral Mesh Geometry to import a converted CAD file for Shielding and Criticality calculations with MONK and MCBEND *Proc. 11th Int. Conf. Radiat. Shield. 14th Top. Meet. Radiat. Prot. Shield. (RPS-2008), USA* .
- Barker T, Bird A & Thetford R 2008. CAD import for MONK and MCBEND by converting to Tetrahedral Mesh format *Representations* **99**, 570–571.
- Castillo E, Castillo R, Martinez J, Shenoy M & Guerrero T 2010. Four-dimensional deformable image registration using trajectory modeling *Phys. Med. Biol.* **55**(1), 305–327.
- Chan Hyeong K, Jong Hwi J, Wesley E B, Kun-Woo C & Sung Bae H 2011. A polygon-surface reference Korean male phantom (PSRK-Man) and its direct implementation in Geant4 Monte Carlo simulation. *Phys. Med. Biol.* **56**(10), 3137–3161.
- Cornuejols G & Tütüncü R 2006. *Optimization methods in finance* Cambridge University Press.
- Fang Q 2010. Mesh-based Monte Carlo method using fast ray-tracing in Plucker coordinates *Biomed Opt Express* **1**(1), 165–175.
- Fonseca G P, Landry G, White S, D'Amours M, Yoriyaz H, Beaulieu L, Reniers B & Verhaegen F 2014. The use of tetrahedral mesh geometries in Monte Carlo simulation of applicator based brachytherapy dose distributions. *Phys. Med. Biol.* **59**(19), 5921–35.
- Furuta T, Sato T, Han M C, Yeom Y S, Kim C H, Brown J L & Bolch W E 2017. Implementation of tetrahedral-mesh geometry in Monte Carlo radiation transport code PHITS *Phys. Med. Biol.* **62**(12).
- Gould N & Toint P L 2004. Preprocessing for quadratic programming *Math. Program.* **100**(1), 95–132.
- Han M C, Yeom Y S, Kim C H, Kim S & Sohn J W 2015. New approach based on tetrahedral-mesh geometry for accurate 4D Monte Carlo patient-dose calculation. *Phys. Med. Biol.* **60**(4), 1601.
- Ishikawa K L, Takagi S, Matthys K & Wada S 2009 4D Monte Carlo Dose Calculations for Particle Therapy Combined with the Spring Network Model of Lung Motion in 'World Congr. Med. Phys. Biomed. Eng. Sept. 7-12, 2009, Munich, Ger.' Springer Springer Berlin Heidelberg pp. 183–186.

- Kass M, Witkin A & Terzopoulos D 1988. Snakes: Active contour models *Int. J. Comput. Vis.* **1**(4), 321–331.
- Kataria T, Sharma K, Subramani V, Karrthick K P & Bisht S S 2012. Homogeneity Index: An objective tool for assessment of conformal radiation treatments. *J. Med. Phys.* **37**(4), 207–13.
- Low D A, Harms W B, Mutic S & Purdy J A 1998. A technique for the quantitative evaluation of dose distributions *Med. Phys.* **25**(5), 656–661.
- Manescu P, Azencot J, Beuve M, Ladjal H & Saad J 2012. Material density mapping on deformable 3D models of human organs **6**(Paris V), 125–134.
- Manescu P, Ladjal H, Azencot J, Beuve M, Testa E & Shariat B 2014. Four-dimensional radiotherapeutic dose calculation using biomechanical respiratory motion description *Int. J. Comput. Assist. Radiol. Surg.* **9**(3), 449–457.
- Marmitt G & Slusallek P 2006. Fast ray traversal of tetrahedral and hexahedral meshes for direct volume rendering *Proc. Eighth Jt. Eurographics / IEEE VGTC Conf. Vis.* pp. 235–242.
- Newhauser W 2001. Dosimetry for the gantry beams at the northeast proton therapy center *Dimens. Geom. relationships Massachusetts Gen. Hosp. Rep. HD-112*.
- Newhauser W, Fontenot J, Koch N, Dong L, Lee A, Zheng Y, Waters L & Mohan R 2007. Monte Carlo simulations of the dosimetric impact of radiopaque fiducial markers for proton radiotherapy of the prostate *Phys. Med. Biol.* **52**(11), 2937–2952.
- Paganetti H 2016. *Proton therapy physics* CRC Press.
- Poole C M, Cornelius I, Trapp J V & Langton C M 2012a. A CAD interface for GEANT4 *Australas. Phys. Eng. Sci. Med.* **35**(3), 329–334.
- Poole C M, Cornelius I, Trapp J V & Langton C M 2012b. Fast tessellated solid navigation in GEANT4 *IEEE Trans. Nucl. Sci.* **59**(4 PART 3), 1695–1701.
- Rietzel E, Schardt D & Haberer T 2007. Range accuracy in carbon ion treatment planning based on CT-calibration with real tissue samples *Radiat. Oncol.* **2**(1), 14.
- Sato T, Niita K, Matsuda N, Hashimoto S, Iwamoto Y, Noda S, Ogawa T, Iwase H, Nakashima H, Fukahori T, Okumura K, Kai T, Chiba S, Furuta T & Sihver L 2013. Particle and Heavy Ion Transport code System, PHITS, version 2.52 *J. Nucl. Sci. Technol.* **50**(9), 913–923.
- Schaffner B & Pedroni E 1998. The precision of proton range calculations in proton radiotherapy treatment planning: experimental verification of the relation between CT-HU and proton stopping power *Phys. Med. Biol.* **43**(6), 1579–1592.
- Schneider W, Bortfeld T & Schlegel W 2000. Correlation between CT numbers and tissue parameters needed for Monte Carlo simulations of clinical dose distributions *Phys. Med. Biol.* **45**(2), 459–478.
- Shen H & Wang G 2010. A tetrahedron-based inhomogeneous Monte Carlo optical simulator. *Phys. Med. Biol.* **55**(4), 947–962.
- Si H 2010. A quality tetrahedral mesh generator and a 3d delaunay triangulator.
- Si H & Gärtner K 2015. Meshing Piecewise Linear Complexes by Constrained Delaunay Tetrahedralizations *Proc. 14th Int. Meshing Roundtable* **41**(2), 147–163.
- Touileb Y, Manescu P & Ladjal H 2016. Motion-Induced Monte Carlo Dose Calculation Using Deformable Tetrahedral Meshes *IEEE Int. Symp. Biomed. Imaging (IEEE ISBI)* pp. 1257–1260.
- White D R, Griffith R V & Wilson I J 1992. Report 46 *J. Int. Comm. Radiat. Units Meas.* **os24**(1), NP.
- Yeom Y S, Jeong J H, Han M C & Kim C H 2014. Tetrahedral-mesh-based computational human phantom for fast Monte Carlo dose calculations. *Phys. Med. Biol.* **59**(12), 3173–3185.
- Zahra N, Frisson T, Grevillot L, Lautesse P & Sarrut D 2010 ‘Influence of Geant4 parameters on dose distribution and computation time for carbon ion therapy simulation’.
- Zhang R & Newhauser W D 2009. Calculation of water equivalent thickness of materials of arbitrary density, elemental composition and thickness in proton beam irradiation *Phys. Med. Biol.* **54**(6), 1383–1395.

Permanence, perseverance and persistence in spite of all obstacles, discouragements, and impossibilities: It is this, that in all things distinguishes the strong soul from the weak.

Thomas Carlyle

4

Motion compensation of WEPL for 4D dose calculations

4.1 INTRODUCTION

Radiotherapeutic dosimetry aims at determining the quantity of energy deposited in the tumor volume and the surrounding tissues as a result of an external beam radiation therapy. In the case of hadrontherapy, accurate dosimetry is needed for treatment planning and verification. The estimation of dose distribution is calculated using computer simulations that require the modeling of the anatomical features of the patient's body. As shown in the previous chapters, we have developed a tetrahedral model that model human anatomy and estimate the dose by defining the density information and the material composition in the elements. Then we have further improved the model by introducing a beam-dependent density mapping method that calculates the density values of the elements by minimizing the error of the water equivalent path length in the direction of the beam.

However, this method has been only established in a static configuration where the movement is not taken into account. Unfortunately, in the case of lung tumors, the continuous density changes due to respiratory motion affect the ranges of ions which can lead to inaccurate dose calculations. These deformations need to be considered when calculating the dose distribution in a motion-induced simulation. To obtain accurate four-dimensional dose calculations, the Monte Carlo simulations have to be coupled with a motion estimation method and the dose has to be accumulated over time. In this chapter, we will investigate the extension of the WEPL algorithm to compensate for the movement in dose calculations. First, we will introduce a method to incorporate the stopping power in the formulae of the WEPL to obtain a more precise effective density map compared to the simplified version defined in the previous chapter. Then, we will measure range uncertainties related to both methods compared to an experimental value calculated using the Monte Carlo code. Then, we will present a method for the updating of the density values for each tetrahedral element over time. Finally, we will compare our tetrahedral based algorithm results to the gold standard voxel-based structure using a 4D multi-layer phantom (4DMLP). Furthermore, possible future directions are presented.

4.2 CALCULATION OF WATER EQUIVALENT THICKNESS IN PROTON BEAM IRRADIATION

As stated in the previous chapter, the Water equivalent path length (also known as the water equivalent thickness (WET)) is defined as the mass thickness of liquid water described in ($g.cm^2$) that causes a particle beam to lose the same amount of energy as the beam would lose by traversing a certain depth of a material [175][176][177] [178][178][179][180].

In the previous chapter, we have used a simple deterministic formula to estimate the value of the water equivalent path length in the algorithm of the effective density calculation. However, we have ignored the value of the mean stopping power of both water and the material by making the assumption that most thorax tissues have a stopping power ratio ($\frac{\overline{S_m}}{\overline{S_w}}$) close to 1 in the following equation reported by Zhang and Newhauser [177]:

$$WEPL = t_w = t_m \frac{\rho_m \overline{S_m}}{\rho_w \overline{S_w}} \quad (4.1)$$

where t_w and t_m are the thicknesses of water and the target material, respectively. ρ_w and ρ_m are the mass densities of water and the material, respectively. Finally, $\overline{S_w}$ and $\overline{S_m}$ are the mean values of mass stopping power for water and the material, respectively.

We will refer to our simplified version of the WEPL as the WEPL simplified or $WEPL_{simplified}$ in the rest of the document, and we define it in the following equation as:

$$WEPL_{simplified} = t_w = t_m \frac{\rho_m}{\rho_w} \quad (4.2)$$

Another parameter that could be alternatively used beside the WEPL(or WET) to specify the particle range, is the water equivalent ratio (WER) [181], which is the ratio of WET to the material mass thickness in [$g.cm^{-2}$] and defined as t_w/t_m . This parameter has the advantage to be nearly constant at different proton energies for a specific material [182]. This ratio is also considered as the relative stopping power (RSP).

In this section, we will consider the stopping power ratio between the material and the water to calculate the water equivalent thickness and study its effect on the beam range and dose distribution in comparison of our previous method.

Several methods for calculating WET in proton beams were suggested in the literature [175] [82] [183]. Nevertheless, these methods use either a time-consuming iterative numerical method or fast and approximate techniques of unknown accuracy. Authors in [176][177] introduced analytical formulas based on theoretical range-energy relations, that are supposed to achieve 1 mm uncertainty in WET in the case of proton fields. However, their method only takes into account a limited number of target materials and thickness and also considers only energies inferior to 250 MeV. However, in clinical practice, the treatment planning systems for proton therapy require a CT calibration curve relating the Hounsfield units to the relative stopping power of the materials to calculate the WET. The most common technique to the calibration is the stoichiometric approach [184] that has the advantage of being straightforward and well-defined. We will adopt this method to calculate the RSP of different materials in the CT-images since it requires less computation time and also for its accepted accuracy.

4.3 CT HU-TO-STOPPING POWER CALIBRATION

The Calibrated computer tomographic data are the primary input for hadrontherapy treatment planning systems that handle tissues inhomogeneities effects. The beam range required for patient treatment is calculated by converting the CT HU numbers to particle stopping power values using an HU-to-SPR calibration curve (see figure 4.3.1). This stoichiometric calibration method is designed to estimate the water equivalent thickness and to determine the particle range for various human tissues. Three separate linear fits were done for three main categories: adipose tissues, the organs, and muscles, and finally, bone structures. It is expected that the range of the particles in the human anatomy can be controlled to better than $\pm 1.1\%$ of the water equivalent range in soft tissue and to $\pm 1.8\%$ in bone structures in which it translates to a precision that varies from 1 to 3 mm [185]. The resulted WEPL is referred to as the $WEPL_{st}$ (i.e., stoichiometric water equivalent path length). Furthermore, to evaluate the $WEPL_{st}$, we have calculated the experimental WEPL using Geant4 Monte Carlo code and a Multi-layer phantom. The experimental value will be considered as the reference to estimate the difference in the beam range for both the $WEPL_{simplified}$ and the $WEPL_{st}$. In the following sections, we will first present the Multi-layer phantom geometry and material composition than we will discuss in detail the calculation of the range of the beam and its validation.

4.4 MULTI-LAYER PHANTOM (MLP) CASE

The Multi-layer phantom will be used for the validation of the WEPL calculation as well as in the deformation simulation. In the same way as the Multi-layer phantom of the previous chapter, we will use four layers of matters, including tumor, lung, bone, and muscle tissues from the inside to the outside. The density values and the corresponding HU numbers are depicted in table 4.5.1. The only difference relies on the thickness of the layers and the proportions of the phantom (see figure 4.4.1). These values were chosen to obtain integer proportions in the voxel-based structure, even in the deformation of the geometry.

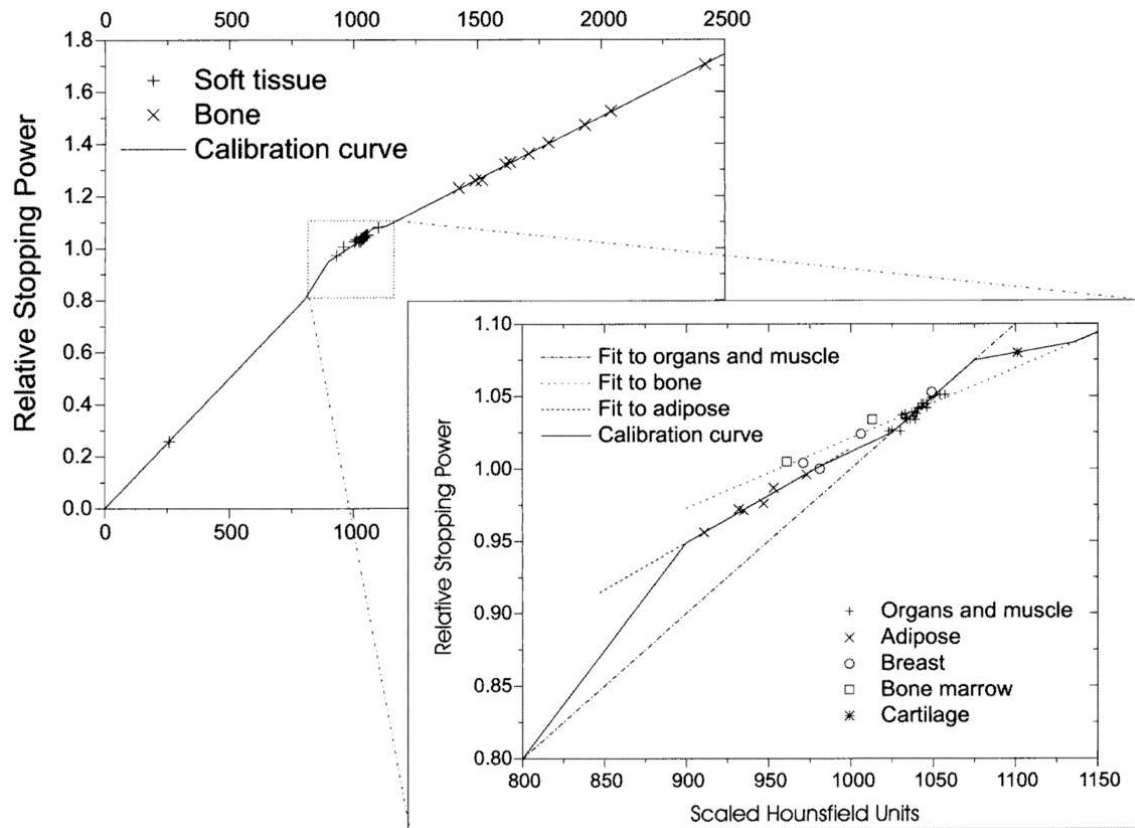


Figure 4.3.1: HU-to-relative stopping power for different human tissues. Image from [185].

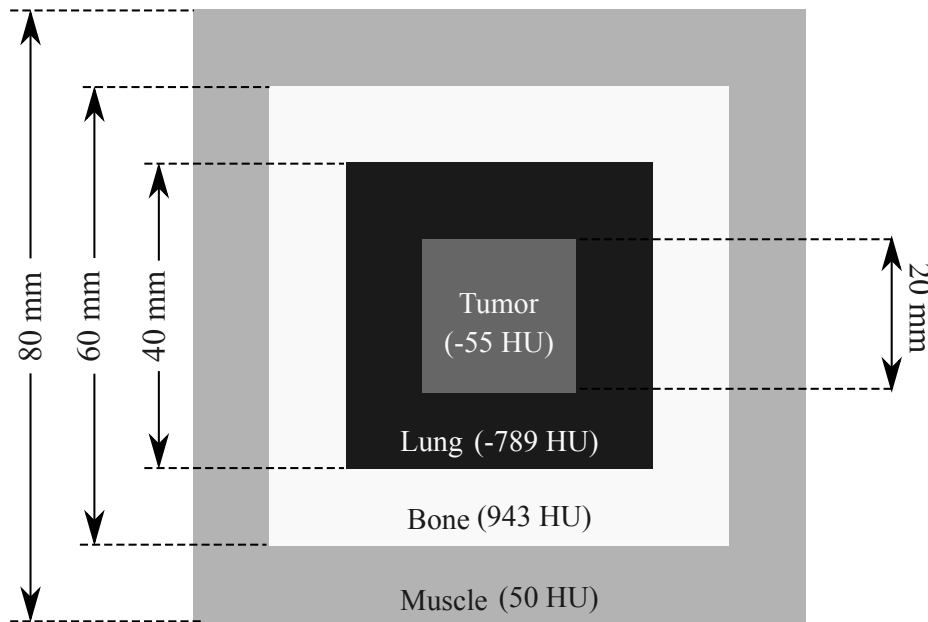


Figure 4.4.1: The geometrical configuration of the 4D multi layer phantom (4DMLP) with four layers of matter.

4.5 EXPERIMENTAL CALCULATION OF THE WEPL

A precise estimation of the water equivalent path length is essential for the algorithm of the creation of the effective density. Therefore, in this section, we will first calculate the experimental WEPL and then compare it to the simplified WEPL value used in the previous chapter and the value computed using the stoichiometric method. To define the experimental water equivalent path length, we will calculate the difference between the beam range obtained with a water volume, and the beam resulted using the geometry volume alongside the water volume. In the case of the multi-layer phantom, we will have the configuration depicted in figure 4.5.1, in which we will only extract the tissues that are before the central cube, representing the tumor.

The clinical proton range is defined as the depth distal of 80% of the maximum dose in a pristine Bragg Peak value ($R_{80\%}$) in which 50% of the protons stopped independently of the energy spread of the beam [177] [186] [25] [187] [188]. The particle range is dependent on particle energy, type and the material of an absorber. If a slab of thickness t_m of a non-water material is placed in front of a liquid water phantom that generates a range $R_{80\%}$, it will produce a range of $R_{80\%}^{Shifted}$ using the same

Layer	Materials	HU	Density ($g.cm^{-3}$)
0	Adipose tissue (Tumor)	-55	0.967
1	Lung tissue (Lung inhale)	-789	0.217
2	Marrow bone (Bone)	943	1.575
3	Soft tissue (Muscle)	50	1.061

Table 4.5.1: Materials, density considered in the 4DMulti-layer phantom (4DMLP). Data adapted from ICRU Report 49

Energy (MeV)	50 (low energy)	90 (medium energy)	250 (high energy)
$WEPL_{G_4}$ (mm)		28.20	
$WEPL_{simplified}$ (mm)		28.53	
$WEPL_{st}$ (mm)		27.95	
Absolute Relative Error of $WEPL_{simplified}$ (%)		1.17	
Absolute Relative Error of $WEPL_{st}$ (%)		0.94	

Table 4.5.2: Errors of the wepl calculated between the reference WEPL($WEPL_{G_4}$) and the $WEPL_{simplified}$ and the $WEPL_{st}$ using three different energies. These values are calculated on the layers before the tumor of the 4DMLP (figure 4.5.1). The $WEPL_{G_4}$ reference value is the difference between the WET calculated using only the Water phantom and by adding the 4DMLP matters that are before the tumor (see figure 4.5.2)

monoenergetic proton beam. Thus, WEPL here is defined as:

$$WEPL = t_w = R_{80\%} - R_{80\%}^{Shifted} \quad (4.3)$$

We will use the experimental $WEPL$ as the reference value to evaluate the $WEPL_{simplified}$ and the $WEPL_{st}$ for a geometry setup in the MC simulations. We obtained, as a result, the same value of thickness using three different initial beam energies: low, medium, and high energy (i.e., 50, 90 and 230 MeV respectively). The two Bragg peaks are presented in figure 4.5.2. Moreover, even though the absolute relative error of the both the $WEPL_{simplified}$ and the $WEPL_{st}$ don't exceed 2%, the stoichiometric WEPL reduce the error to 0.94% (as depicted in table 4.5.2). In the following sections, we will evaluate the impact of this difference of range on the dose distribution of the tetrahedral mesh.

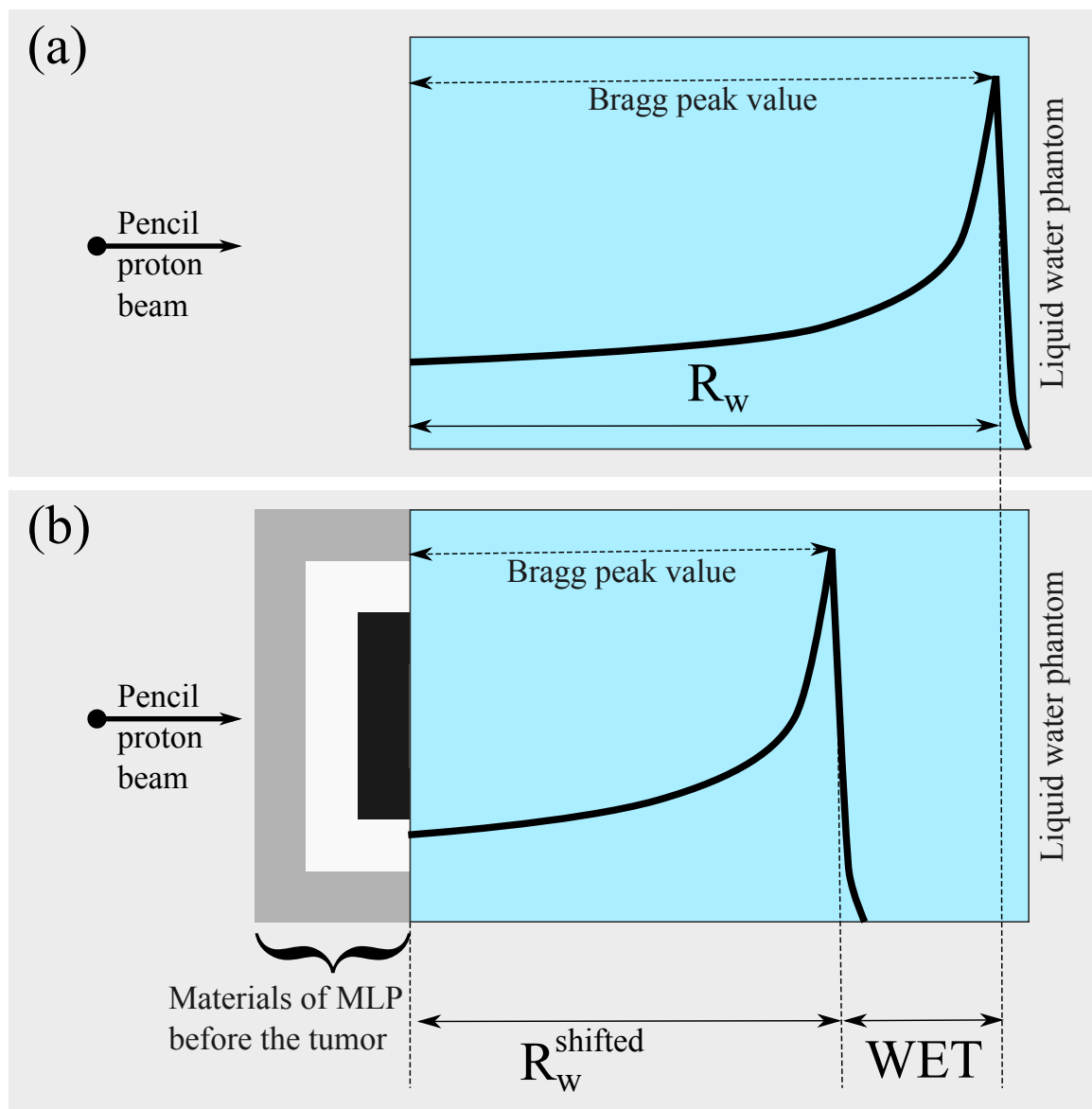


Figure 4.5.1: (a) Depth dose curve including the Bragg peak and proton range (R_w) in a water phantom. (b) the part of the MLP before the tumor volume is added in front of the water phantom. $R_w^{shifted}$ is produced and the WET is defined as the difference between the ranges $R_w - R_w^{shifted}$.

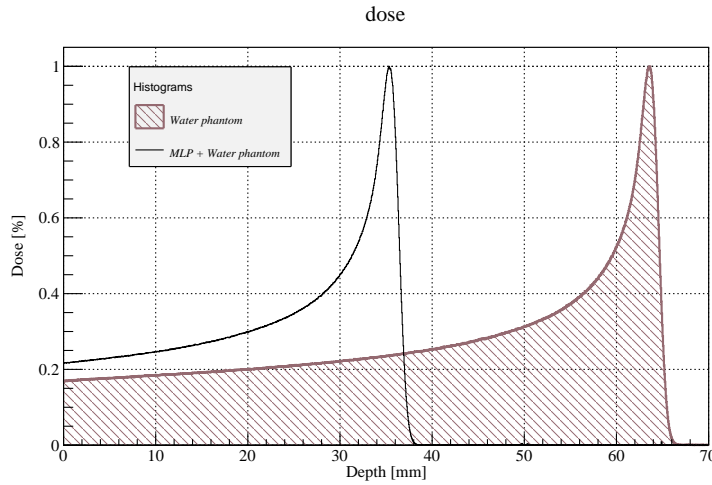


Figure 4.5.2: The normalized dose-versus-depth profiles for the simulated liquide water phantom and the integration of the materials of the MLP that are before the tumor volume. These curves were produced using a 90 MeV beam to calculate the WET of the Materials of MLP described in figure 4.5.1. The WET will serve as a reference and it is equal to 28.2 mm.

4.6 EFFECTIVE DENSITY CALCULATION USING STOICHIOMETRIC WEPL

Before the simulation of the particle-matter interactions with the tetrahedral mesh, the density values inside every tetrahedral element need to be defined using a density mapping algorithm. In chapter two, we have established a mass conservation mapping algorithm named MCM that respects the principle of mass conservation. Then, we have defined another algorithm that works on coarse meshes to reduce simulation time. This algorithm is the effective density mapping (or EFFD), and it minimizes the error of $WEPL_{simplified}$ in the direction of the beam and generates biased density values in the tetrahedral elements that intersect the beam. In this section, we will use the same algorithm to alter the density values of the intersected elements. The only difference resides in the fact that instead of calculating the densities in the system of equation, we will calculate the stopping power and furthermore calculate the mass density accordingly. The stoichiometric WEPL is defined as :

$$WEPL_{st} = t_w = t_m \frac{\rho_m \overline{S_m}}{\rho_w \overline{S_w}} = t_m \rho_s \quad (4.4)$$

with ρ_s the stopping power ratio (SPR) between the matter and the water.

Since we want to respect only the $WEPL_{st}$ of only the mediums before the tumor, we define for every ray r_i of the beam a polyline L_i that goes from the exterior surface of the geometry to the tumor site.

Given a tetrahedralization \mathcal{T} of a domain \mathcal{D} representing a medium \mathcal{M} , we define the set of all the elements in intersection with \mathcal{T} as:

$\mathcal{I}_{\beta_{dir}} = \left\{ \bigcup_{k=0}^n e_k \mid e_k \in \mathcal{T} \cap \beta_{dir} \right\}$, where $\beta_{dir} = \left\{ \bigcup_{i=0}^m L_i \right\}$, n is the number of elements of \mathcal{T} that intersect β_{dir} , m is the number of radiation rays representing β_{dir} and e_k is a tetrahedron in intersection with the beam β_{dir} .

The $WEPL_{st}$ of a given polyline of the beam L_i is given as follow:

$$WEPL_{st} = \int_L \rho_s(r) dl \quad (4.5)$$

Knowing that the polyline L_i is characterised by a sequence of line segments $(l_{i,1}, \dots, l_{i,q})$ representing the intersection with $\mathcal{I}_{\beta_{dir}}$. We define the water equivalent path length of a given polyline L_i as :

$$WEPL_{st}(L_i) = \int_{L_i} \rho_s(r_i) dl \quad (4.6)$$

The $WEPL_{st}$ is redefined as :

$$WEPL_{st}(L_i) = \sum_{j=0}^q \rho_s^{eff}(e_j) \times l_{i,j} \quad (4.7)$$

Where q is the number of elements of $\mathcal{I}_{\beta_{dir}}$ that intersect L_i , e_j is a tetrahedron from $\mathcal{I}_{\beta_{dir}}$ that intersects L_i and ρ_s^{eff} is the relative stopping power function defined on $\mathcal{I}_{\beta_{dir}}$ as:

$$\rho_s^{eff} : \begin{cases} \mathcal{I}_{\beta_{dir}} \rightarrow \mathbb{R} \\ e_j \mapsto \rho_s^{eff}(e_j) \end{cases}$$

ρ_s^{eff} represents the biased values of SPR to calculate for the tetrahedral elements in the direction of the beam. To define the ρ_s^{eff} we minimize the error of the $WEPL_{st}$ between the voxel-based geometry and the $WEPL_{eff}$. Furthermore, to calculate the unknown ρ_s^{eff} we obtain the following linear system:

$$Ax = b$$

$$\text{Where } A = \begin{pmatrix} l_{1,1} & l_{1,2} & \cdots & l_{1,n} \\ l_{2,1} & l_{2,2} & \cdots & l_{2,n} \\ \vdots & \vdots & \ddots & \vdots \\ l_{m,1} & l_{m,2} & \cdots & l_{m,n} \end{pmatrix}, \mathbf{x} = \begin{pmatrix} \rho_s^{\text{eff}}(e_1) \\ \rho_s^{\text{eff}}(e_2) \\ \vdots \\ \rho_s^{\text{eff}}(e_n) \end{pmatrix} \text{ and } \mathbf{b} = \begin{pmatrix} \text{WEPL}_{st}^1 \\ \text{WEPL}_{st}^2 \\ \vdots \\ \text{WEPL}_{st}^m \end{pmatrix}$$

l_{ij} : is the length of the line segment of the intersection between the line L_i and an element e_j . WEPL_{st}^i is the water equivalent path length calculated using the reference CT image with the stoichiometric method. Solving this system outputs the vector \mathbf{x} of the effective stopping power values of ρ_s^{eff} that need to be assigned to each tetrahedron of the mesh. To solve this sparse over-determined linear system, we have calculated an optimized solution using a constrained quadratic programming method of the form:

$$\text{QP} \left\{ \begin{array}{l} \text{minimize } \frac{1}{2} \mathbf{x}^T \mathbf{H} \mathbf{x} + \mathbf{c}^T \mathbf{x} \\ \text{subject to: } \mathbf{A} \mathbf{x} = \mathbf{b} \\ \mathbf{lb} \leq \mathbf{x} \leq \mathbf{ub} \end{array} \right.$$

\mathbf{H} : the quadratic matrix ($n \times n$) defined as $\mathbf{H} = \mathbf{A}^T \mathbf{A}$, \mathbf{x} : the vector of decision variables ($n \times 1$) that represents the unknown-density-values vector of ρ_s^{eff} , \mathbf{c} : vector of linear objective function coefficients ($n \times 1$), defined as $\mathbf{c} = -\mathbf{A}^T \mathbf{b}$, and finally \mathbf{lb} and \mathbf{ub} represents respectively the lower and the upper bounds applied to density values. Moreover, the the interior-point-convex algorithm described in ([189], [190]) have been used to solve the problem since it is suited for sparse quadratic programs and also for its faster optimization time compared to other methods.

Now as the effective relative stopping power ρ_s^{eff} is calculated for every elements in $\mathcal{I}_{\beta_{dir}}$, the next step consists of converting the stopping power values into their corresponding mass density values to be used in the Monte Carlo simulation code. For this purpose, we have defined a corresponding curve based on Schneider et al. works on conversion of CT-number to relative stopping power [184] and CT-number calibration to density values [153]. This curve is depicted in figure 4.6.1

4.7 EVALUATION AND RESULT

In this section, we present an application of the deformable tetrahedral-based dose calculation method previously described in this chapter to moving organs such as the multi-layer phantom.

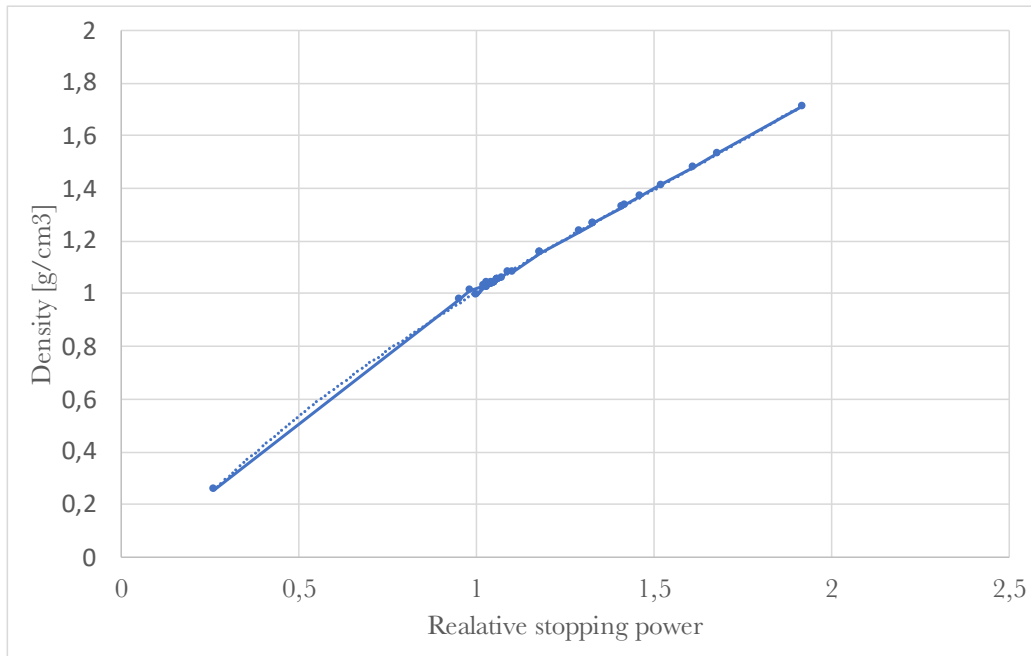


Figure 4.6.1: Mass density values vs relative stopping power.

We start by presenting the simulation setup used to simulate a passive proton beam, then we evaluate the dose distribution using the cumulative dose volume histogram (CDVH) and gamma index. Finally, We conclude by presenting the disadvantages of the method and future improvements.

4.7.1 SIMULATION SETUP

To simulate the deformation of the Multi-layer phantom, we have applied a scaling factor to the vertices of the tetrahedral mesh. All the volumes were scaled with 1.2, 1.25 and 1.2 for $step_1$, $step_2$, and $step_3$, respectively. Nevertheless, we have maintained the tumor volume unchanged throughout the deformation since we aim at studying the impact of the density variation of the tissues before the tumor volume on the dose distribution of the target. The length of the cubes of the MLP and their densities are represented in table 4.7.1. It is worth mentioning that the values of the relative stopping power ρ_s are calculated using the curve illustrated in figure 4.3.1. For particle simulation, we have used a 90 MeV passive beam with sigma energy spread of 0.2%, a step size limit of 0.05 mm and a cut-off value of 0.1 mm. These values were chosen to have accurate results as they are

below the thickness of the mean volume of all the tetrahedrons. Moreover, to cover the target volume in depth, we have used six squared particle sources, as shown in figure 4.7.1. Each of them is placed inside the water volume and generates a BP with a given intensity. The resulted SOBP is furthermore collimated and flattened using a ripple filter.

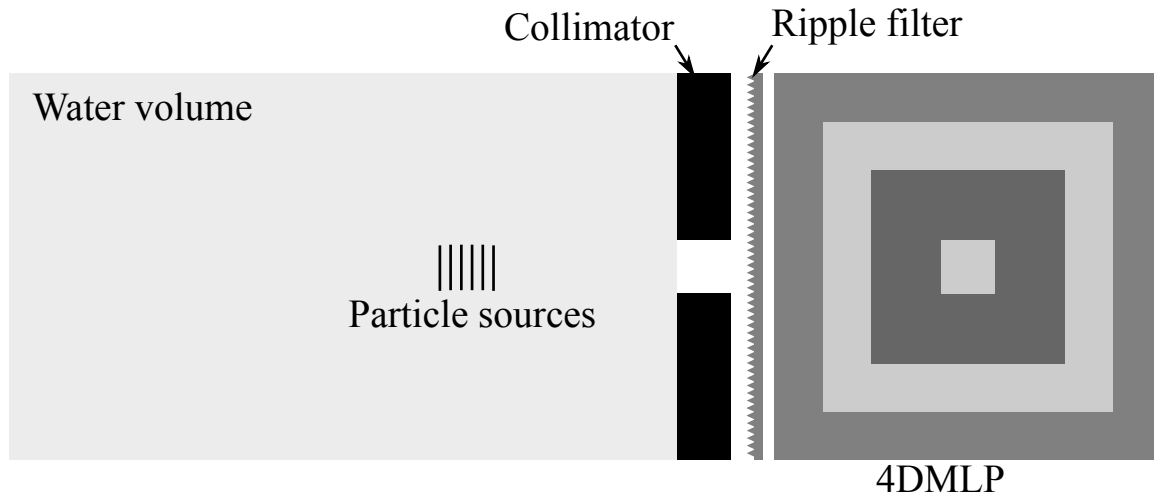


Figure 4.7.1: Geant4 simulation setup of the 4D MLP. The same configuration is used for every step of scaling. A ripple filter was used to flatten the Spread-Out Bragg Peak (SOBP).

4.7.2 4D DOSE EVALUATION

To evaluate the dose map of the tetrahedral mesh generated using the $WEPL_{st}$, we use the voxel-based structure as our gold standard. Moreover, we have also simulated the tetrahedral models created using other density mapping algorithms, including the centroid method (CM), the mass conservation method (MCM), and the EFFF method using the $WEPL_{simplified}$. The purpose is to assess the dose distribution inside the target volume using the 4D multi-layer phantom. The metrics that are used for evaluation are the Cumulative dose-volume histograms (CDVH) and the gamma index evaluation (γ). The former will give an overview of the target coverage and the homogeneity of the dose over the entire volume, while the latter illustrates the difference between the calculated dose and a reference dose map. In the gamma evaluation, a distance-to-agreement criterion of 3 mm and a 3% dose difference in agreement with clinical standards were used for all dose comparisons.

		Cube 0	Cube 1	Cube 2	Cube 3
Step 0	Cube length [mm]	20	40	60	80
	Density [g.cm ⁻³]	0.967	0.217	1.575	1.061
	HU	-55	-789	943	50
	HU calibrated	945	211	1943	1050
	SPR (ρ_s)	1.0076	0.211	1.5098	1.0728
Step 1	Cube length [mm]	20	48	72	96
	Density [g.cm ⁻³]	0.967	0.11	0.911	0.614
	HU	-55	-894	-116	-405
	HU calibrated	945	106	884	595
	SPR (ρ_s)	1.0076	0.106	0.884	0.595
Step 2	Cube length [mm]	20	60	90	120
	Density [g.cm ⁻³]	0.967	0.058	0.466	0.314
	HU	-55	-945	-548	-696
	HU calibrated	945	55	452	304
	SPR (ρ_s)	1.0076	0.055	0.452	0.304
Step 3	Cube length [mm]	20	72	108	144
	Density [g.cm ⁻³]	0.967	0.033	0.27	0.1819
	HU	-55	-968	-739	-825
	HU calibrated	945	32	261	175
	SPR (ρ_s)	1.0076	0.032	0.261	0.175

Table 4.7.1: 4DMLP deformation parameters including cube length, mass density, HU, HU calibrated and the relative stopping power in each simulation step.

Figure 4.7.2(a) shows different CDVHs inside the tumor volume (i.e.; $cube_o$) for the static simulation or $step_o$. We can notice that the centroid method (CM) gives the worst results which were expected since the density value of a tetrahedron element is defined using the density of the voxel that contains its centroid. As for MCM and EFFD using $WEPL_{simplified}$, even though the dose distribution is slightly better in EFFD both methods demonstrate similar outcomes. However, we can clearly state that correcting the WEPL in the EFFD method gives a similar dose homogeneity compared to the voxel-based dose map. The same observation applies to the CDVHs of the accumulated dose maps shown in figure 4.7.2(b). Even though the difference between the $WEPL_{simplified}$ and the $WEPL_{st}$ is less than $1mm$, it has an impact on the dose distribution. Furthermore, more precise information regarding the dose are illustrated in table 4.7.2. Statistical information including D_{mean} , D_{min} , D_{max} are calculated for all the used density mapping algorithms. The more interesting value corresponds to the homogeneity index HI which is defined as the ratio between the minimum dose in 5% of the target volume (i.e.; D_5) and the minimum dose in 95% of the target volume (i.e.; D_{95}). The value of HI increase as the dose distribution becomes less homogeneous and an optimal value is an HI value of 1. Furthermore, we confirm with the obtained HI values that EFFD with $WEPL_{st}$ has effectively enhanced the homogeneity of the dose in the target with a relative error of HI less than 1% in both the static and the deformation induced simulations. Besides, the gamma index distributions are presented in figure 4.7.3. As for the gamma evaluation, more than 99% of the values in the gamma map of the tumor are lower than 1 in $step_o$ and the entire simulation, which indicates an excellent agreement between the dose distributions of the EFFD with WEPL corrected and the voxel reference. Additionally, we obtained the gamma values of 95% and 98% for CM and MCM, respectively.

As a conclusion, even though both EFFD methods give very reliable results, EFFD with corrected WEPL inherit the same flaws of the simplified one which is related to the decision of calculating a coherent dose inside a target while ignoring the rest of the tissues. This result is stated in figure 4.7.3, where we can see the difference between EFFD-based methods and the reference in the regions outside the target volume. The values calculated on the entire geometry shows that in static we have a gamma index values of 96.95%, 98.31%, 93.86% and 94.41% for CM, MCM, EFFD with $WEPL_{simplified}$ and EFFD with $WEPL_{st}$, respectively. In the end, it is up to the user to choose between a target-oriented method that only emphasizes a specific region of the geometry and ignore the dose in the remaining tissues. and a method like MCM where a significant number

of the tetrahedron is required to produce a good dose accuracy. It will be interesting to study in the future a multi-target version of the EFFD method where the therapist can define several volumes of interest and ignore the rest of the geometry.

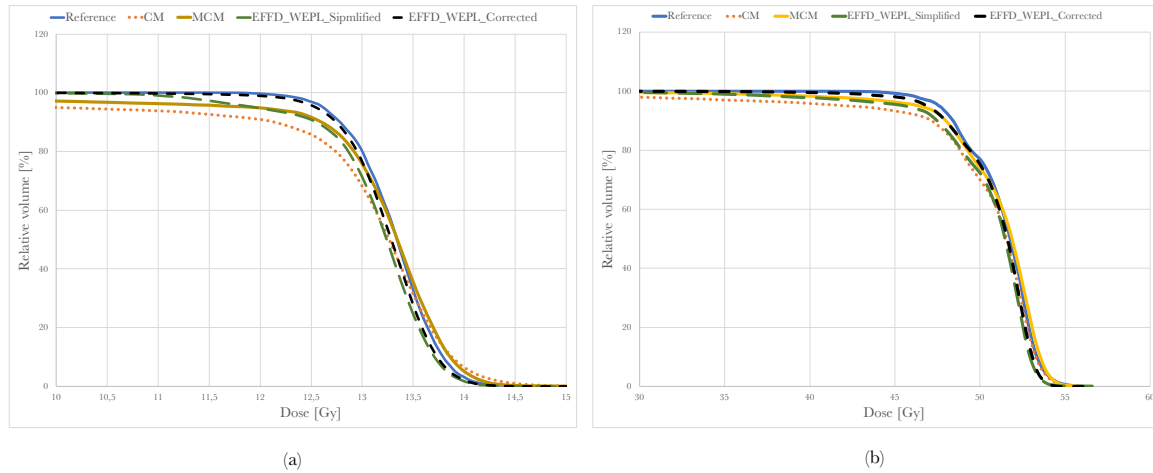


Figure 4.7.2: Cumulative dose volume histogram of the (a) static simulation and the (b) dose accumulation of motion simulation.

	Density mapping algorithm	D_{mean} [Gy]	D_{min} [Gy]	D_{max} [Gy]	HI	Relative error of HI [%]
Static	Voxel-based 4DMLP	13.2952	11.17	14.8263	1.10145	-
	CM	12.8041	0.75932	15.1921	1.40721	27.76
	MCM	13.0566	1.74914	14.9133	1.16916	6.15
	$EFFD_WEPL_{simplified}$	13.0712	7.53829	14.6021	1.16051	5.36
	$EFFD_WEPL_{corrected}$	13.1788	8.40928	14.58	1.10373	0.21
4D	Voxel-based 4DMLP	51.2268	40.9837	56.1509	1.12751	-
	CM	49.8246	4.60465	55.8406	1.27016	12.65
	MCM	50.7342	17.0481	55.7874	1.16772	3.57
	$EFFD_WEPL_{simplified}$	50.2388	23.3868	55.0002	1.16686	3.49
	$EFFD_WEPL_{corrected}$	50.7039	29.8808	55.1559	1.13809	0.94

Table 4.7.2: Evaluation of dose distribution in the tumor volume of the 4D multi-layer phantom for $step_0$ and 4D simulation. D_{min} , D_{max} , D_{mean} are respectively the minimum, the maximum and the mean dose deposited. HI is the Homogeneity index.

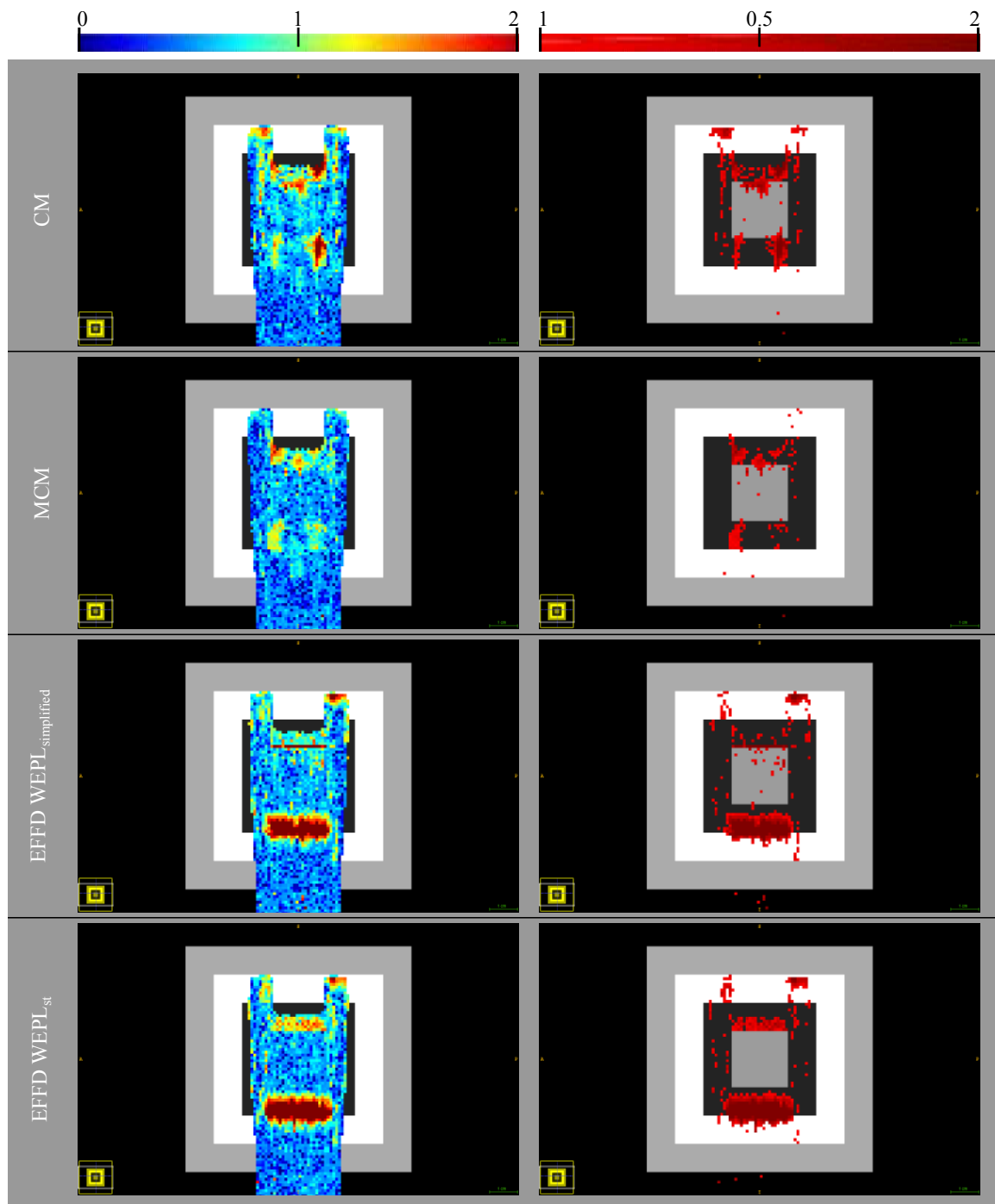


Figure 4.7.3: Axial slices of the 4DMLP gamma index evaluation of CM, MCM, EFFD with $WEPL_{simplified}$ and EFFD with $WEPL_{st}$ of deformation-induced simulations. A Dose to agreement (DTA) of 3 mm and dose tolerance of 3% were used in all the simulations. The regions that fail the criteria in the gamma evaluation are clearly identified where gamma index is > 1 . Right: a second scale was used to isolate the regions that fail the test.

4.8 CONCLUSION

In this chapter, an improvement version of the effective density mapping algorithm has been presented. We have used a stoichiometric method to estimate the water equivalent path length of the tissues before the tumor to calculate the stopping power of the materials of the tetrahedral elements. Afterward, we have converted the stopping power onto density values to be used in the Monte Carlo simulation. Once the density map is improved, we have emulated a deformation field by applying a scaling factor on the Multi-layer phantom. The density values were updated by respecting the principle of mass conservation and that by respecting the mass of the elements in each simulation step. Final results have shown that our model gives better dose homogeneity in the tumor volume than the CM and MCM methods. Moreover, the correction of the WEPL formula has improved dose homogeneity in the tumor volume compared to the simplified version defined in the previous chapter. However, in the other tissues outside the tumor, the dose accuracy is not necessarily respected since by essence our method is optimized to the target volume only and ignore the density values of the elements in the that intersect the beam. It will be interesting to extend our algorithm to incorporate more than one target volume to optimize the density values in the direction of the beam.

Success is not final, failure is not fatal: it is the courage to continue that counts.

Winston Churchill

5

General conclusions and future perspectives

Oncological hadron therapy represents a promising alternative solution to the ubiquitous conventional megavolt photon therapy especially for the treatment of deep-seated local tumors. This technique uses heavy-charged particles like protons or carbon ions to irradiate the tumors. The particularity of heavy-ion particles resides in the fact that they deposit most of their energy at the end of their range creating the Bragg Peak. This property guarantees precise irradiation of the target volume and less damage to healthy tissues. Nevertheless, since the range of particles depends on the density and the chemical composition of the traversed tissues, hadron therapy is very sensitive to tissues deformation and patient set-up during the treatment. Therefore, respiratory-induced organ motion constitutes one of the most difficult challenges of treatment planning in Hadrontherapy, and it represents a significant source of uncertainty in the estimation of dose. The complexity of organ deformations during respiration and the non-reproducibility of the breathing patterns make existing image-based dose calculation techniques prone to errors. This fact pushed many research labs to develop biomechanical models that use finite element analysis. Among these labs, our team,

in collaboration with IPNL laboratory, have developed in the past decade, a biomechanical model of the respiratory system that is driven by both ribcage motion and diaphragm contraction. The final goal is to monitor the model using external surrogates.

However, even though biomechanical models can accurately estimate the deformations and the position of organs during the treatment, they don't give a precise material density information of the simulated tissues. To address this problem, our team has defined a continuous representation of physical quantities based on the principle of mass conservation. This description aims at calculating physical quantities like mass density or the dose on the vertices of the tetrahedral mesh by ensuring the continuity of the represented function. Furthermore, the value of the function can be calculated at any point inside the tetrahedral mesh using a linear interpolation of the values in the vertices. Nevertheless, despite the encouraging outcome of this method, the tetrahedral mesh is only used to accumulate the dose, and the user is constrained to voxelize the tetrahedral mesh to simulate the interaction between the particle beam and the matter.

In this Ph.D. project, we have demonstrated a 4D dose calculation method based only on tetrahedral geometries where each volume is represented with a tetrahedral mesh that deforms with time. Besides, the internal movement is described using vertex displacement, hence making tissue tracking implicit.

The first part of our project consists of defining a four-dimensional dose calculation method based on the principle of mass conservation. The main idea is to create a tetrahedral model that doesn't only represents the geometry of the internal anatomy, but also the density and the chemical composition of the tissues of organs. Additionally, the model has to ensure the deformation of the anatomy while conserving the mass of all individual tetrahedron. To create the time-dependent density map required for the Monte Carlo dose calculations, we have proposed a method for density mapping that map density information issued from CT-images to the tetrahedral mesh. Furthermore, we accumulate the dose overtime on the tetrahedrons to create a dose map. As a result, we have demonstrated that tetrahedral geometries give accurate dose distributions as voxel-based geometries in the case of thorax-geometries. Moreover, to confirm our findings, we have studied the impact of the resolution of the tetrahedral mesh on the accuracy of dose distribution. We concluded that a fine tetrahedral mesh has to be used to obtain acceptable outcomes. Since the accuracy of the density mapping algorithm depends on the number of tetrahedrons, particularly in highly heterogeneous structures like the lung. Another problem arises with the relatively ex-

cessive number of tetrahedrons, which is the considerable time required to load the geometry and to simulate the passage of particles in the Monte Carlo simulation. To address this problem, we have defined another dose calculation method that guarantees an accurate dose distribution while reducing the number of elements in the mesh. The main idea is to minimize the error of the water equivalent path length in the direction of the particle beam instead of respecting the principle of mass conservation. We first demonstrated that respecting the mass in the hole geometry when calculating the density values is not enough to guarantee a coherent dose in coarse meshes. Then, we showed that if the water equivalent path length of the tissues in the trajectory of the beam is respected, we can use fewer tetrahedrons to represent the patient. As for Monte Carlo simulations, we generate an effective density map that is dependent on the direction of the beam. This map has reduced the error of the water equivalent path length by 2 *mm* in the case of a patient geometry. Additionally, it leads to a calculation time shorter than the quarter time needed for other density mapping algorithms for the same dose accuracy.

In the last part of our work, we extend the effective density algorithm to incorporate the deformation of organs. Moreover, we use a more precise description of the water equivalent path length that takes into account the stopping power of different materials. We conclude that by applying our beam-dependant algorithm on a tetrahedral mesh with fewer elements, we generate a reliable dose distribution inside the target volume in both static and motion-compensated simulations. However, this target-oriented approach ensures dose accuracy only in the target volume and neglects the other organs. It will be interesting to develop a version of this algorithm that takes into account multiple regions of interest in the future. We could also study the impact of using carbon ion or other hadrons on the outcomes of our tetrahedral-based dose calculation.



Linear interpolation

A.1 LINEAR DENSITY VARIATION

PUNCTUAL DENSITY In a n -dimensional space, let there be $p+1$ points of $\mathfrak{R}^n : \{ A_0, A_1, \dots, A_p \}$. The convex hull $C(A)$ of these points is given by:

$$C(A) = \left\{ M = \sum_{i=0}^p \lambda_i \cdot A_i \mid \lambda_i \geq 0, (i = 0, 1, \dots, p), \sum_{i=0}^p \lambda_i = 1 \right\} \quad (\text{A.1})$$

In other words, λ_i are the barycentric coordinates of the point M with respect to the polyhedra defined by the points A_i .

For every vertex A_i of the polyhedra we associate a positive density value $\rho_i = \rho(A_i)$. Then, for

every point $M \in C(A)$ we define the punctual density $\rho : C(A) \rightarrow \mathfrak{R}$:

$$M = \sum_{i=0}^p \lambda_i \cdot A_i \longrightarrow \rho(M) = \sum_{i=0}^p \lambda_i \cdot \rho_i \quad (\text{A.2})$$

MASS CALCULATION Integrating density (radioactivity density) over a domain equals to finding the mass (number of disintegrations) of that domain. For example, in a 1-dimensional space the domain of integration is a line segment (linear mass).



Figure A.1.1: 1-D case : line segment AB

Let $M \in [AB]$ (Figure 1). The position of M can be written using barycentric coordinates as follows:

$$M = M(t) = t \cdot B + (1 - t) \cdot A \quad (\text{A.3})$$

According to (3) we obtain :

$$\rho(M) = t \cdot \rho_B + (1 - t) \cdot \rho_A \quad (\text{A.4})$$

Let $J = [\frac{\partial M}{\partial t}]$; $\Delta = |\det(J)| = |AB|$. If we integrate on $[AB]$ we get:

$$Mass_{AB} = \int_{M \in [AB]} \rho(M) \cdot dM = \int \Delta \cdot \rho(M(t)) \cdot dt = AB \cdot \int \rho(M(t)) \cdot dt.$$

Finally we obtain:

$$Mass_{AB} = |AB| \cdot \frac{\rho_A + \rho_B}{2} \quad (\text{A.5})$$

Next, we're going to analyse the case of a 3-D space (Figure 2). In this case, as discussed before, the basic shape is the tetrahedron and we're going to calculate its mass by integrating the punctual density defined in the previous section.

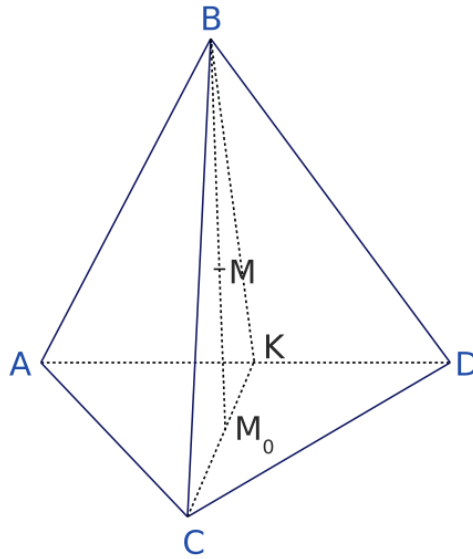


Figure A.1.2: 3-D case : Volume of the tetrahedron $ABCD = \frac{1}{6} |\det(\vec{AB}, \vec{AC}, \vec{AD})|$

M and $d(M)$ can be expressed according to equation (3) ($p = 3$), but for integrating purposes, we're going to express them according to equation (4). So,

$$M \in [AM_0] \Rightarrow M = \theta \cdot M_0 + (1 - \theta) \cdot A, \quad 0 \leq \theta \leq 1.$$

$$M_0 \in [KC] \Rightarrow M_0 = t \cdot C + (1 - t) \cdot K, \quad 0 \leq t \leq 1.$$

$$K \in [BD] \Rightarrow K = \tau \cdot D + (1 - \tau) \cdot B, \quad 0 \leq \tau \leq 1.$$

And, according to (5), we can express the punctual density of M as follows:

$$\rho(M) = (1 - \theta) \cdot \rho_A + \theta(1 - \tau)(1 - t) \cdot \rho_B + \theta \cdot t \cdot \rho_C + \theta \cdot \tau(1 - \tau) \cdot \rho_D \quad (\text{A.6})$$

Let $J = \begin{bmatrix} \frac{\partial M}{\partial \tau} & \frac{\partial M}{\partial t} & \frac{\partial M}{\partial t} \end{bmatrix} = V \cdot \Theta$ with $V = \begin{bmatrix} \vec{BD} & \vec{BC} & \vec{BA} \end{bmatrix}$ and $\det(V) = 6 \cdot \text{Vol}(ABCD)$.

$$\Theta = \begin{bmatrix} \theta(1-t) & -\tau\theta & \tau(a-\tau) \\ 0 & \theta & t \\ 0 & 0 & 1 \end{bmatrix}.$$

with $\det(\Theta) = \theta^2(1-\theta)$. We put $\Delta^2 = \det(J^t J) = [\det(V) \cdot \det(\Theta)]^2$. Integrating the density inside the tetrahedron (ABCD) gives:

$$\text{Mass}_{ABCD} = \int_{M \in (ABCD)} \rho(M) \cdot dM = \int \int \int \Delta \cdot \rho(M(\tau, \theta, t)) \cdot d\theta \cdot dt \cdot d\tau.$$

$$\text{Mass}_{ABCD} = |\det(V)| \cdot \int \int \int \theta^2(1-\theta) \cdot \rho(M(\tau, \theta, t)) \cdot d\theta \cdot dt \cdot d\tau = |\det(V)| \cdot \frac{\rho_A + \rho_B + \rho_C + \rho_D}{24}.$$

Finally we obtain:

$$\text{Mass}_{ABCD} = \text{Vol}(ABCD) \cdot \frac{\rho_A + \rho_B + \rho_C + \rho_D}{4} \quad (\text{A.7})$$

A.2 LINEAR INTERPOLATION RESAMPLING (LR)

The intensity varies linearly between grid positions. Unlike nearest neighbor interpolation, the interpolated intensity is spatially continuous. However, the intensity gradient will be discontinuous at grid positions.

A.3 RESAMPLING USING NEAREST NEIGHBOR INTERPOLATION (NN)

In the nearest neighbor interpolation, the value of the nearest voxel is taken. That is, it assumes that the image intensity is piecewise constant with jumps mid-way between grid positions. This interpolation scheme is cheap as it does not require any floating point computations.

Listing of figures

1.1.1	Depth dose distribution for photons and monoenergetic Bragg curves for carbon ions and protons [18].	5
1.1.2	Treatment plans of esophageal cancer using proton therapy (left) and X-rays/IMRT (right). Proton therapy limits the radiation delivered outside the target and reduces the likelihood of lung complications. The conformity to the target volume is precise in the two cases. However, the dose of surrounding organs is minimized when using protons. Source Seattle cancer care alliance, Proton therapy center 2017 and [21].	6
1.1.3	In a typical treatment plan for proton therapy, the spread out Bragg peak (SOBP, dashed blue line) is the therapeutic radiation distribution. The SOBP is the sum of several individual Bragg peaks (thin blue lines) at staggered depths. The depth-dose plot of an X-ray beam (red line) is provided for comparison. The pink area represents additional doses of X-ray radiotherapy—which can damage normal tissues and cause secondary cancers, especially of the skin	6
1.1.4	Schematic of a fully a passive beam shaping system in Hadrontherapy. Figure redrawn from [20].	8
1.1.5	Schematic of the GSI raster-scan system. Figure redrawn from [23].	8
1.2.1	Fluctuations in respiratory motion patterns registered at close time intervals. The curves represent the patient surface displacement in the superior-inferior, anterior-posterior and medial-lateral dimensions. In (a) the patterns are almost identical but in (b) there are no respiratory distinguishable patterns [34].	11
1.2.2	Effect of target motion on a circular phantom. The tumor is centered and it is represented by the gray circle. The thin black circle indicates a 10-mm 3D geometric expansion of the tumor into the planning target volume (a) The dashed lines are isodose lines (50%, 80%, 90%, 95%, 100% of the maximum dose) for a single passive proton beam. (b) Isodose lines for a 10 mm displacement of the tumor with respect to the treatment beam. [25].	12

1.2.3	Impact of density on the beam range. Depth-dose profiles of a photon beam and a proton SOBP, dashed lines represent the profile generated after adding a higher density material (gray rectangle from 5 to 7 cm) in the trajectory of the used beams. [25].	13
1.2.4	Range fluctuations expressed in water equivalent path length overlapped on the 4D-CT images. Image from [39].	14
1.3.1	Graphical representation of the volumes of interest, as defined in ICRU Reports No. 50 and 62.	16
2.3.1	The result of a deformable image registration algorithm applied on a phantom. The deformed grid represents the transformed pixels of the source image using the deformed vector field (DVF).	25
2.3.2	(a) Biomechanical model of the thorax including lungs, rib cage, and diaphragm. (b) Physiological compliance calculated for lung for five patients. Image taken from [118].	27
2.5.1	Notation used for tetrahedrons. T_j and T_{j+1} are two adjacent tetrahedrons.	33
2.5.2	Tetrahedral mesh deformation from the time step t to $t + 1$. Deforming the tetrahedron T_j using vertex displacement.	34
2.6.1	Flowchart of tetrahedral model construction: from 3D-CT to tetrahedral density map. Each organ is described by a tetrahedral mesh obtained from 3D CT images. The CT images are first converted into voxelized mass density maps which are then mapped to the tetrahedral elements of the meshes.	37
2.6.2	Density mapping methods, f is a linear interpolation function. Left: Continuous Mass Conservation Mapping (CMCM). Center: Mass Conservation Mapping (MCM). Right: Centroid Mapping (CM).	38
2.6.3	Tetrahedral density map generation. The mass of a tetrahedral element equals the sum of the masses of volumes of intersection between the tetrahedron and the grid of voxels. Example of applying equation (2.6) in a 2D space: $m(T_k) = m(I_k^1) + m(I_k^2) + m(I_k^4) + m(I_k^5) + m(I_k^6) + m(I_k^8) + m(I_k^9)$ for the MCM method. In the case of the Centroid Method: $m(T_k) = m(V_5)$	39
2.6.4	Deformable tetrahedron implementation using Geant4	41
2.6.5	Beam shaping with range compensator and multileaf collimator. In this particular example we have 10 RC lines.	43
2.6.6	Range compensator and S.O.B.P constructor	45
2.7.1	Sphere simulation setup in Geant4. 10 disk sources particles are placed inside the water envelop to generate the SOBP. A cylindrical collimator is used to adapt the passive beam to the inner concentric sphere (tumor).	46

2.7.2	Energy profile of static simulation for the three geometric configurations : Geant4 primitives, tetrahedral mesh and voxelized map.	47
2.7.3	Flow chart of 4D dose accumulation in respiratory motion-induced simulation.	49
2.7.4	Cumulative dose volume histogram (CDVH) deposited in the tumor. Left : no motion, right : with motion.	50
2.7.5	Dose distributions of Monte Carlo simulations. Top: tetrahedral model. middle: sagittal view of voxel grid. Bottom: 4D Dose distribution (left: accumulated dose in tetrahedral mesh. right : accumulated dose in CT data for all phases.	56
2.8.1	Flowchart of tetrahedral model construction: from 3D-CT to multiresolution tetrahedral model. The CT images are first converted into voxelized mass density maps which are then mapped to the tetrahedral elements of the meshes.	57
2.8.2	Tps configuration for lung. Two single filed passive beams were used in opposite directions, each with its own range compensator and collimator.	57
2.8.3	A thorax geometry representing a patient case used for the multiresolution study. The proton beam is directed toward the tumor and the dose is saved in the tetrahedral elements of the mesh.	58
2.8.4	Gamma pass rate vs the voxel-to-tetrahedron ratio using a dta equal to 3mm and a dose tolerance of 3%. Beam 1 and Beam 2 are the proton beams used in the lung case illustrated in figure 2.8.2.	59
2.8.5	Gamma pass rate vs the voxel-to-tetrahedron ratio for the patient case simulation. For the gamma evaluation a dta equal to 3mm and a dose tolerance of 3% have been used.	59
2.8.6	Relation between computation time and the resolution of the tetrahedral mesh. (a) Number of tetrahedrons versus calculation time. (b) Voxel-to-tetrahedron ratio versus calculation time. Loading time is the time needed to load all the tetrahedral elements to the system. Simulation time is the time taken by the Monte Carlo code to calculate the interactions between the particle beam and the matter. The total time is the sum of loading time and simulation time. These values were calculated using 10^5 proton particles fired at the multiresolution lung geometry.	60
4.3.1	HU-to-relative stopping power for different human tissues. Image from [185].	90
4.4.1	The geometrical configuration of the 4D multi layer phantom (4DMLP) with four layers of matter.	91
4.5.1	(a) Depth dose curve including the Bragg peak and proton range (R_w) in a water phantom. (b) the part of the MLP before the tumor volume is added in front of the water phantom. $R_w^{shifted}$ is produced and the WET is defined as the difference between the ranges $R_w - R_w^{shifted}$	93

4.5.2	The normalized dose-versus-depth profiles for the simulated liquide water phantom and the integration of the materials of the MLP that are before the tumor volume. These curves were produced using a 90 MeV beam to calculate the WET of the Materials of MLP described in figure 4.5.1. The WET will serve as a reference and it is equal to 28.2 mm.	94
4.6.1	Mass density values vs relative stopping power.	97
4.7.1	Geant4 simulation setup of the 4D MLP. The same configuration is used for every step of scaling. A ripple filter was used to flatten the Spread-Out Bragg Peak (SOBP).	98
4.7.2	Cumulative dose volume histogram of the (a) static simulation and the (b) dose accumulation of motion simulation.	101
4.7.3	Axial slices of the 4DMLP gamma index evaluation of CM, MCM, EFFD with $WEPL_{simplified}$ and EFFD with $WEPL_{st}$ of deformation-induced simulations. A Dose to agreement (DTA) of 3 mm and dose tolerance of 3% were used in all the simulations. The regions that fail the criteria in the gamma evaluation are clearly identified where gamma index is > 1 . Right: a second scale was used to isolate the regions that fail the test.	102
A.1.1.1	1-D case : line segment AB	108
A.1.1.2	3-D case : Volume of the tetrahedron $ABCD = \frac{1}{6} det(\vec{AB}, \vec{AC}, \vec{AD}) $	109

List of Tables

2.7.1	Dose relative error of voxels and tetras comparing to gold standard of spheres simulation. DED: dose relative error, LR : Linear resampling, NN: nearest neighborhood. LR and NN are two different methods used for interpolation (see Appendix A.2 and A.3).	48
2.7.2	Evaluation of dose distribution in tumor volume. D_{min} , D_{max} , D_{mean} are respectively the minimum, the maximum and the mean dose deposited. HI (Homogeneity index).	48
4.5.1	Materials, density considered in the 4DMulti-layer phantom (4DMLP). Data adapted from ICRU Report 49	92
4.5.2	Errors of the wepl calculated between the reference WEPL($WEPL_{G_4}$) and the $WEPL_{simplified}$ and the $WEPL_{st}$ using three different energies. These values are calculated on the layers before the tumor of the 4DMLP (figure 4.5.1). The $WEPL_{G_4}$ reference value is the difference between the WET calculated using only the Water phantom and by adding the 4DMLP matters that are before the tumor (see figure 4.5.2)	92
4.7.1	4DMLP deformation parameters including cube length, mass density, HU, HU calibrated and the relative stopping power in each simulation step.	99
4.7.2	Evaluation of dose distribution in the tumor volume of the 4D multi-layer phantom for $step_o$ and 4D simulation. D_{min} , D_{max} , D_{mean} are respectively the minimum, the maximum and the mean dose deposited. HI is the Homogeneity index. . . .	101

References

- [1] BWKP Stewart and Christopher P Wild. World cancer report 2014. *World Health Organization*, 505, 2014. URL <http://www.thehealthwell.info/node/725845>.
- [2] J. Izewska and International Atomic Energy Agency. *Setting up a radiotherapy programme : clinical, medical physics, radiation protection, and safety aspects*. International Atomic Energy Agency, 2008. ISBN 920101807X.
- [3] Alain Gerbault. The GEC ESTRO handbook of brachytherapy. 2002. URL <https://www.estro.org/binaries/content/assets/estro/about/gec-estro/handbook-of-brachytherapy/aa-final-introduction.pdf>.
- [4] John Buscombe and Shaunak Navalkissoor. Molecular radiotherapy. *Clinical Medicine*, 12(4):381–386, 2012. URL <http://www.clinmed.rcpjournals.org/content/12/4/381.short>.
- [5] Rajamanickam Baskar, Kuo Ann Lee, Richard Yeo, and Kheng-Wei Yeoh. Cancer and radiation therapy: current advances and future directions. *International journal of medical sciences*, 9(3):193–9, 2012. ISSN 1449-1907. doi: 10.7150/ijms.3635. URL <http://www.ncbi.nlm.nih.gov/pubmed/22408567><http://www.pubmedcentral.nih.gov/articlerender.fcgi?artid=PMC3298009>.
- [6] Stephen P Jackson and Jiri Bartek. The DNA-damage response in human biology and disease. *Nature*, 461(7267):1071, 2009. URL <https://www.nature.com/articles/nature08467>.
- [7] Adrian C Begg, Fiona Stewart, and Conchita Vens. Strategies to improve radiotherapy with targeted drugs. *Nature Reviews Cancer*, 11(4):239, 2011. URL <https://www.nature.com/articles/nrc3007>.
- [8] Leopold Freund. Ein mit Röntgenstrahlen behandelter Fall von Naevus pigmentosus piliferus. *Wiener Medizinische Wochenschrift*, 47:428–434, 1897.

- [9] Wilhelm Conrad Röntgen. Ueber eine neue Art von Strahlen. *Sitzung: Sitzungsberichte der Physikalisch-medicinischen Gesellschaft zu Würzburg*, 30(1):132–141, 1895.
- [10] Hansson Nils, Martin Michael, and Heiner Fangerau. The Nobel Prize runner-up Leopold Freund and the origin of radiotherapy. *Radiotherapy and Oncology*, 119(3): 552, 2016. URL [http://www.thegreenjournal.com/article/S0167-8140\(16\)31067-2/abstract](http://www.thegreenjournal.com/article/S0167-8140(16)31067-2/abstract).
- [11] Manuel Lederman. The early history of radiotherapy: 1895–1939. *International Journal of Radiation Oncology* Biology* Physics*, 7(5):639–648, 1981.
- [12] Henry S Kaplan. Basic principles in radiation oncology. *Cancer*, 39(S2):689–693, 1977.
- [13] James M. Slater. From X-Rays to Ion Beams: A Short History of Radiation Therapy. pages 3–16. Springer, Berlin, Heidelberg, 2012. doi: 10.1007/978-3-642-21414-1_1. URL http://link.springer.com/10.1007/978-3-642-21414-1_{_}1.
- [14] Robert R. Wilson. Radiological Use of Fast Protons. *Radiology*, 47(5):487–491, nov 1946. ISSN 0033-8419. doi: 10.1148/47.5.487. URL <http://pubs.rsna.org/doi/10.1148/47.5.487>.
- [15] Ugo Amaldi. History of hadrontherapy in the world and Italian developments. *Rivista Medica*, 14(1), 2008.
- [16] Olivia Kelada. The potential advantages and disadvantages of cancer therapy using charged particles compared with megavoltage x-rays. *Particle Therapy Cancer Research Institute*, 2011.
- [17] William Henry Bragg and R Kleeman. XXXIX. On the α particles of radium, and their loss of range in passing through various atoms and molecules. *The London, Edinburgh, and Dublin Philosophical Magazine and Journal of Science*, 10(57):318–340, 1905.
- [18] Emmanouil Fokas, Gerhard Kraft, Hanxiang An, and Rita Engenhardt-Cabillic. Ion beam radiobiology and cancer: time to update ourselves. *Biochimica et Biophysica Acta (BBA)-Reviews on Cancer*, 1796(2):216–229, 2009. URL <https://www.sciencedirect.com/science/article/pii/S0304419X09000523>.
- [19] Daniela Schulz-Ertner and Hirohiko Tsujii. Particle radiation therapy using proton and heavier ion beams. *Journal of clinical oncology*, 25(8):953–964, 2007. URL <https://pdfs.semanticscholar.org/15e5/b640506be38db74bfbfb7640e8c3baf89f2a.pdf>.

- [20] Dieter Schardt, Thilo Elsässer, and Daniela Schulz-Ertner. Heavy-ion tumor therapy: Physical and radiobiological benefits. *Reviews of Modern Physics*, 82(1):383–425, feb 2010. ISSN 00346861. doi: 10.1103/RevModPhys.82.383. URL <http://link.aps.org/doi/10.1103/RevModPhys.82.383>.
- [21] Yue-Can Zeng, Shilpa Vyas, Quang Dang, Lindsay Schultz, Stephen R Bowen, Veena Shankaran, Farhood Farjah, Brant K Oelschlager, Smith Apisarnthanarax, and Jing Zeng. Proton therapy posterior beam approach with pencil beam scanning for esophageal cancer : Clinical outcome, dosimetry, and feasibility. *Strahlentherapie und Onkologie*, 192(12):913–921, dec 2016. ISSN 1439-099X. doi: 10.1007/s00066-016-1034-4. URL <http://link.springer.com/10.1007/s00066-016-1034-4><http://www.ncbi.nlm.nih.gov/pubmed/27596221>.
- [22] S E McGowan, N G Burnet, and A J Lomax. Treatment planning optimisation in proton therapy. *The British Journal of Radiology*, 86(1021):20120288–20120288, jan 2013. ISSN 0007-1285. doi: 10.1259/bjr.20120288. URL <http://www.birpublications.org/doi/10.1259/bjr.20120288>.
- [23] Michael Kramer. Swift ions in radiotherapy—Treatment planning with TRiP98. *Nuclear Instruments and Methods in Physics Research Section B: Beam Interactions with Materials and Atoms*, 267(6):989—992, 2009. URL <https://www.sciencedirect.com/science/article/pii/S0168583X09002456>.
- [24] Antony J. Lomax, Thomas Bortfeld, Gudrun Goitein, Juergen Debus, Christine Dykstra, Pierre Alain Tercier, Philippe A. Coucke, and Rene O. Mirimanoff. A treatment planning inter-comparison of proton and intensity modulated photon radiotherapy. *Radiotherapy and Oncology*, 51(3):257–271, 1999. ISSN 01678140. doi: 10.1016/S0167-8140(99)00036-5. URL <https://www.sciencedirect.com/science/article/pii/S0167814099000365>.
- [25] Harald Paganetti. *Proton therapy physics*. CRC Press, 2016.
- [26] DTL Langen, KM and Jones. Organ motion and its management. *International Journal of Radiation Oncology* Biology* Physics*, 50(1):265—278, 2001. doi: 10.1109/ICIF.2008.4632383. URL <https://www.sciencedirect.com/science/article/pii/S0360301601014535>.
- [27] Ritsuko Britton, Keith R and Starkschall, George and Tucker, Susan L and Pan, Tinsu and Nelson, Christopher and Chang, Joe Y and Cox, James D and Mohan, Radhe and Komaki. Assessment of gross tumor volume regression and motion changes during radiotherapy for non–small-cell lung cancer as measured by four-dimensional computed. *Inter-*

- national Journal of Radiation Oncology* Biology* Physics*, 68(4):1036—1046, 2007. URL <https://www.sciencedirect.com/science/article/pii/S0360301607001411>.
- [28] Hiroki Shirato, Shinichi Shimizu, Kei Kitamura, Takeshi Nishioka, Kenji Kagei, Seiko Hashimoto, Hidefumi Aoyama, Tatsuya Kunieda, Nobuo Shinohara, Hirotohi Dosaka-Akita, and Kazuo Miyasaka. Four-dimensional treatment planning and fluoroscopic real-time tumor tracking radiotherapy for moving tumor. *International Journal of Radiation Oncology Biology Physics*, 48(2):435–442, 2000. ISSN 03603016. doi: 10.1016/S0360-3016(00)00625-8. URL <https://www.sciencedirect.com/science/article/pii/S0360301600006258>.
- [29] Gig S. Mageras, Alex Pevsner, Ellen D. Yorke, Kenneth E. Rosenzweig, Eric C. Ford, Agung Hertanto, Steven M. Larson, D. Michael Lovelock, Yusuf E. Erdi, Sadek A. Nehmeh, John L. Humm, and C. Clifton Ling. Measurement of lung tumor motion using respiration-correlated CT. *International Journal of Radiation Oncology Biology Physics*, 60(3):933–941, 2004. ISSN 03603016. doi: 10.1016/j.ijrobp.2004.06.021. URL <https://www.sciencedirect.com/science/article/pii/S0360301604010788>.
- [30] U. W. Langner and P. J. Keall. Accuracy in the localization of thoracic and abdominal tumors using respiratory displacement, velocity, and phase. *Medical Physics*, 36(2):386–393, jan 2009. ISSN 00942405. doi: 10.1118/1.3049595. URL <http://doi.wiley.com/10.1118/1.3049595>.
- [31] R. E. Wurm, F. Gum, S. Erbel, L. Schlenger, D. Scheffler, D. Agaoglu, R. Schild, B. Gebauer, P. Rogalla, M. Plotkin, K. Ocran, and V. Budach. Image guided respiratory gated hypofractionated Stereotactic Body Radiation Therapy (H-SBRT) for liver and lung tumors: Initial experience. *Acta Oncologica*, 45(7):881–889, jan 2006. ISSN 0284-186X. doi: 10.1080/02841860600919233. URL <http://www.tandfonline.com/doi/full/10.1080/02841860600919233>.
- [32] Michael Velec, Joanne L. Moseley, Cynthia L. Eccles, Tim Craig, Michael B. Sharpe, Laura A. Dawson, and Kristy K. Brock. Effect of breathing motion on radiotherapy dose accumulation in the abdomen using deformable registration. *International Journal of Radiation Oncology Biology Physics*, 80(1):265–272, 2011. ISSN 03603016. doi: 10.1016/j.ijrobp.2010.05.023. URL <https://www.sciencedirect.com/science/article/pii/S0360301610007467>.
- [33] S. S. Vedam, V. R. Kini, P. J. Keall, V. Ramakrishnan, H. Mostafavi, and R. Mohan. Quantifying the predictability of diaphragm motion during respiration with a noninvasive external marker. *Medical Physics*, 30(4):505–513, 2003. ISSN 00942405. doi: 10.1118/1.1558675. URL <https://aapm.onlinelibrary.wiley.com/doi/abs/10.1118/1.1558675>.

- [34] Paul J. Keall, Gig S. Mageras, James M. Balter, Richard S. Emery, Kenneth M. Forster, Steve B. Jiang, Jeffrey M. Kapatoes, Daniel A. Low, Martin J. Murphy, Brad R. Murray, Chester R. Ramsey, Marcel B. Van Herk, S. Sastry Vedam, John W. Wong, and Ellen Yorke. The management of respiratory motion in radiation oncology report of AAPM Task Group 76a). *Medical Physics*, 33(10):3874–3900, sep 2006. ISSN 00942405. doi: 10.1118/1.2349696. URL <http://doi.wiley.com/10.1118/1.2349696>.
- [35] H H Liu, P Balter, T Tutt, B Choi, J Zhang, C Wang, M Chi, D Luo, T Pan, S Hunjan, G Starkschall, I Rosen, K Prado, Z Liao, R Komaki, J D Cox, R Mohan, and L Dong. Assessing respiration-induced tumor motion and internal target volume using 4DCT for radiation therapy of lung cancer. *Int J Radiat Oncol Biol Phys*, 68:531–540, 2007. URL <https://www.sciencedirect.com/science/article/pii/S0360301607000922>.
- [36] Jan-Jakob Sonke, Joos Lebesque, and Marcel Van Herk. Variability of four-dimensional computed tomography patient models. *International Journal of Radiation Oncology* Biology* Physics*, 70(2):590—598, 2008. URL <https://www.sciencedirect.com/science/article/pii/S0360301607040746>.
- [37] KR Britton, G Starkschall, SL Tucker, T Pan International Journal of ..., and Undefined 2007. Assessment of gross tumor volume regression and motion changes during radiotherapy for non–small-cell lung cancer as measured by four-dimensional computed. *International Journal of Radiation Oncology* Biology* Physics*, 68(4):1036—1046, 2007. URL <https://www.sciencedirect.com/science/article/pii/S0360301607001411>.
- [38] J Lambert, N Suchowerska, D R McKenzie, and M Jackson. Intrafractional motion during proton beam scanning. *Physics in medicine and biology*, 50(20):4853–4862, 2005. ISSN 0031-9155. doi: 10.1088/0031-9155/50/20/008.
- [39] S Mori, J Wolfgang, HM Lu, R Schneider International Journal of ..., and Undefined 2008. Quantitative assessment of range fluctuations in charged particle lung irradiation. *International Journal of Radiation Oncology* Biology* Physics*, 70(1):253—261, 2008. URL <https://www.sciencedirect.com/science/article/pii/S0360301607039910>.
- [40] Martijn Engelsman and Hanne M. Kooy. Target volume dose considerations in proton beam treatment planning for lung tumors. *Medical Physics*, 32(12):3549–3557, nov 2005. ISSN 00942405. doi: 10.1118/1.2126187. URL <http://doi.wiley.com/10.1118/1.2126187>.
- [41] Zhouguang Hui, Xiaodong Zhang, George Starkschall, Yupeng Li, Radhe Mohan, Ritsuko Komaki, James D. Cox, and Joe Y. Chang. Effects of Interfractional Motion and Anatomic Changes on Proton Therapy Dose Distribution in Lung Cancer. *International Journal of*

- Radiation Oncology*Biology*Physics*, 72(5):1385–1395, dec 2008. ISSN 0360-3016. doi: 10.1016/J.IJROBP.2008.03.007. URL <https://www.sciencedirect-com.docelec.univ-lyon1.fr/science/article/pii/S0360301608004148>.
- [42] John W. Wong, Michael B. Sharpe, David A. Jaffray, Vijay R. Kini, John M. Robertson, Janifer S. Stromberg, and Alavro A. Martinez. The use of active breathing control (ABC) to reduce margin for breathing motion. *International Journal of Radiation Oncology Biology Physics*, 44(4):911–919, 1999. ISSN 03603016. doi: 10.1016/S0360-3016(99)00056-5. URL <https://www.sciencedirect.com/science/article/pii/S0360301699000565>.
- [43] Yoshiharu Negoro, Yasushi Nagata, Tetsuya Aoki, Takashi Mizowaki, Norio Araki, Kenji Takayama, Masaki Kokubo, Shinsuke Yano, Sachiko Koga, Keisuke Sasai, Yuta Shibamoto, and Masahiro Hiraoka. The effectiveness of an immobilization device in conformal radiotherapy for lung tumor: Reduction of respiratory tumor movement and evaluation of the daily setup accuracy. *International Journal of Radiation Oncology Biology Physics*, 50(4): 889–898, 2001. ISSN 03603016. doi: 10.1016/S0360-3016(01)01516-4. URL <https://www.sciencedirect.com/science/article/pii/S0360301601015164>.
- [44] R Amzi A Bdulrahman and R Obert T Immerman. FOUR-DIMENSIONAL COMPUTED TOMOGRAPHY SCAN ANALYSIS OF TUMOR AND ORGAN MOTION AT VARYING LEVELS OF ABDOMINAL COMPRESSION DURING STEREOTACTIC TREATMENT OF LUNG AND LIVER JOHN H. H EINZERLING, M. D.,* JOHN F. ANDERSON, B. S.,* L ECH P APIEZ, P H. *Elsevier*, 70(5):1571–1578, 2008. doi: 10.1016/j.ijrobp.2007.12.023. URL <https://www.sciencedirect.com/science/article/pii/S0360301607047633>.
- [45] M Eckermann, M Hillbrand, M Herbst, and H Rinecker. Scanning proton beam radiotherapy under functional apnea. In *PTCOG 50*, page 6.1.1, 2011. URL <https://scholar.google.fr/scholar?hl=en&as{ }sdt=o{ }2C5{ }q=Scanning+proton+beam+radiotherapy+under+functional+apnea{ }btnG=>
- [46] E Pedroni, R Bearpark, T Böhringer, A Coray ... für medizinische Physik, and undefined 2004. The PSI Gantry 2: a second generation proton scanning gantry. *Elsevier*, 14(1):25—34, 2004. URL <https://www.sciencedirect.com/science/article/pii/S0939388915700784>.
- [47] Sven Oliver Grözinger, Eike Rietzel, Qiang Li, Christoph Bert, Thomas Haberer, and Gerhard Kraft. Simulations to design an online motion compensation system for scanned particle beams. *Physics in Medicine and Biology*, 51(14):3517–3531, 2006. ISSN 00319155. doi: 10.1088/0031-9155/51/14/016. URL <http://iopscience.iop.org/article/10.1088/0031-9155/51/14/016/meta>.

- [48] Takuji Furukawa, Taku Inaniwa, Shinji Sato, Takehiro Tomitani, Shinichi Minohara, Kouji Noda, and Tatsuaki Kanai. Design study of a raster scanning system for moving target irradiation in heavy-ion radiotherapy. *Medical Physics*, 34(3):1085–1097, feb 2007. ISSN 00942405. doi: 10.1118/1.2558213. URL <http://doi.wiley.com/10.1118/1.2558213>.
- [49] Hideo D Kubo and Bruce C Hill. Respiration gated radiotherapy treatment: A technical study. *Physics in Medicine and Biology*, 41(1):83–91, jan 1996. ISSN 00319155. doi: 10.1088/0031-9155/41/1/007. URL <http://stacks.iop.org/0031-9155/41/i=1/a=007?key=crossref.8632ff4f73662fcf526d14e38f163202>.
- [50] P. J. Keall, V. R. Kini, S. S. Vedam, and R. Mohan. Potential radiotherapy improvements with respiratory gating. *Australasian Physical and Engineering Sciences in Medicine*, 25(1):1–6, 2002. ISSN 01589938. doi: 10.1007/BF03178368. URL <https://link.springer.com/article/10.1007/BF03178368>.
- [51] Hsiao Ming Lu, Robert Brett, Gregory Sharp, Soiros Safai, Steve Jiang, Jay Flanz, and Hanne Kooy. A respiratory-gated treatment system for proton therapy. *Medical Physics*, 34(8):3273–3278, jul 2007. ISSN 00942405. doi: 10.1118/1.2756602. URL <http://doi.wiley.com/10.1118/1.2756602>.
- [52] Tiezhi Zhang, Harry Keller, Matthew J. O'Brien, Thomas R. Mackie, and Bhudatt Paliwal. Application of the spirometer in respiratory gated radiotherapy. *Medical Physics*, 30(12):3165–3171, 2003. ISSN 00942405. doi: 10.1118/1.1625439. URL <https://onlinelibrary.wiley.com/doi/abs/10.1118/1.1625439>.
- [53] Vijay R. Kini, Subrahmanya S. Vedam, Paul J. Keall, Sumukh Patil, Clayton Chen, and Radhe Mohan. Patient training in respiratory-gated radiotherapy. *Medical Dosimetry*, 28(1):7–11, 2003. ISSN 09583947. doi: 10.1016/S0958-3947(02)00136-X. URL <https://www.sciencedirect.com/science/article/pii/S095839470200136X>.
- [54] S. S. Vedam, P. J. Keall, V. R. Kini, and R. Mohan. Determining parameters for respiration-gated radiotherapy. *Medical Physics*, 28(10):2139–2146, 2001. ISSN 00942405. doi: 10.1118/1.1406524. URL <https://aapm.onlinelibrary.wiley.com/doi/abs/10.1118/1.1406524>.
- [55] Shinichi Minohara, Tatsuaki Kanai, Masahiro Endo, Kouji Noda, and Mitsutaka Kanazawa. Respiratory gated irradiation system for heavy-ion radiotherapy. *International Journal of Radiation Oncology Biology Physics*, 47(4):1097–1103, 2000. ISSN 03603016. doi: 10.1016/S0360-3016(00)00524-1. URL <https://www.sciencedirect.com/science/article/pii/S0360301600005241>.

- [56] Takuji Furukawa, Taku Inaniwa, Shinji Sato, Takehiro Tomitani, Shinichi Minohara, Koji Noda, and Tatsuaki Kanai. Design study of a raster scanning system for moving target irradiation in heavy-ion radiotherapy. *Medical Physics*, 34(3):1085–1097, feb 2007. ISSN 00942405. doi: 10.1118/1.2558213. URL <http://doi.wiley.com/10.1118/1.2558213>.
- [57] P. J. Keall, V. R. Kini, S. S. Vedam, and R. Mohan. Motion adaptive x-ray therapy: A feasibility study. *Physics in Medicine and Biology*, 46(1):1–10, 2001. ISSN 00319155. doi: 10.1088/0031-9155/46/1/301. URL <http://iopscience.iop.org/article/10.1088/0031-9155/46/1/301/meta>.
- [58] Noëlle C. van der Voort van Zyp, Jean-Briac Prévost, Mischa S. Hoogeman, John Praag, Bronno van der Holt, Peter C. Levendag, Robertus J. van Klaveren, Peter Pattynama, and Joost J. Nuyttens. Stereotactic radiotherapy with real-time tumor tracking for non-small cell lung cancer: Clinical outcome. *Radiotherapy and Oncology*, 91(3):296–300, jun 2009. ISSN 0167-8140. doi: 10.1016/J.RADONC.2009.02.011. URL <https://www.sciencedirect.com/science/article/pii/S0167814009000681>.
- [59] Qiang Li, Sven Oliver Groezinger, Thomas Haberer, Eike Rietzel, and Gerhard Kraft. On-line compensation for target motion with scanned particle beams: Simulation environment. *Physics in Medicine and Biology*, 49(14):3029–3046, jul 2004. ISSN 00319155. doi: 10.1088/0031-9155/49/14/001. URL <http://stacks.iop.org/0031-9155/49/i=14/a=001?key=crossref.042a9ebfb192265804a81652fed4be7>.
- [60] Sven Oliver Grözinger, Eike Rietzel, Qiang Li, Christoph Bert, Thomas Haberer, and Gerhard Kraft. Simulations to design an online motion compensation system for scanned particle beams. *Physics in Medicine and Biology*, 51(14):3517–3531, jul 2006. ISSN 00319155. doi: 10.1088/0031-9155/51/14/016. URL <http://stacks.iop.org/0031-9155/51/i=14/a=016?key=crossref.bb2988590f9b2b1fcca97c65dbe2f42d>.
- [61] S. Van De Water, R Kreuger, S Zenklusen, E Hug, and A J Lomax. Tumour tracking with scanned proton beams: Assessing the accuracy and practicalities. *Physics in Medicine and Biology*, 54(21):6549–6563, nov 2009. ISSN 00319155. doi: 10.1088/0031-9155/54/21/007. URL <http://stacks.iop.org/0031-9155/54/i=21/a=007?key=crossref.970ce83a2f10c6d3ee22a881d241af00>.
- [62] C Bert, N Saito, A Schmidt, N Chaudhri, D Schardt, and E Rietzel. Target motion tracking with a scanned particle beam. *Med Phys*, 34(12):4768–4771, 2007. URL <https://aapm.onlinelibrary.wiley.com/doi/abs/10.1118/1.2815934> 4010.1002/{%}28ISSN{%}292473-4209.MedicalPhysicsLetter.

- [63] Christoph Bert and Eike Rietzel. 4D treatment planning for scanned ion beams. *Radiation Oncology*, 2(1):24, 2007. ISSN 1748717X. doi: 10.1186/1748-717X-2-24. URL <http://ro-journal.biomedcentral.com/articles/10.1186/1748-717X-2-24>.
- [64] Sven Oliver Grözinger, Christoph Bert, Thomas Haberer, Gerhard Kraft, and Eike Rietzel. Motion compensation with a scanned ion beam: A technical feasibility study. *Radiation Oncology*, 3(1):34, 2008. ISSN 1748717X. doi: 10.1186/1748-717X-3-34. URL <http://ro-journal.biomedcentral.com/articles/10.1186/1748-717X-3-34>.
- [65] Nami Saito, Christoph Bert, Naved Chaudhri, Alexander Gemmel, Dieter Schardt, Marco Durante, and Eike Rietzel. Speed and accuracy of a beam tracking system for treatment of moving targets with scanned ion beams. *Physics in Medicine and Biology*, 54(16):4849–4862, 2009. ISSN 00319155. doi: 10.1088/0031-9155/54/16/001. URL <http://iopscience.iop.org/article/10.1088/0031-9155/54/16/001/meta>.
- [66] Pierre-frédéric Villard, Michaël Beuve, Behzad Shariat, Vincent Baudet, and Fabrice Jaillet. Simulation of Lung Behaviour with Finite Elements : Influence of Bio-Mechanical Parameters. *ieeexplore.ieee.org*, pages 9–14, 2005. URL <https://ieeexplore.ieee.org/abstract/document/1509262/>.
- [67] Anne Laure Didier, Pierre Frédéric Villard, Jean Yves Bayle, Michaël Beuve, and Behzad Shariat. Breathing thorax simulation based on pleura physiology and rib kinematics. In *Proceedings - 4th International Conference Medical Information Visualisation: BioMedical Visualisation, MediViz 2007*, pages 35–40, 2007. ISBN 0769529046. doi: 10.1109/MEDIVIS.2007.8. URL <https://ieeexplore.ieee.org/abstract/document/4272108/>.
- [68] Jacques Saadé, Anne-laure Didier, Romain Buttin, Jean-michel Moreau, Michaël Beuve, Pierre-frédéric Villard, Jardin Botanique, and Villers Nancy. A Preliminary Study for a Biomechanical Model of the Respiratory System, 2010. URL <https://hal.archives-ouvertes.fr/hal-00509817/http://hal.archives-ouvertes.fr/hal-00509817/>.
- [69] Pierre-fédéric Villard. Simulation du Mouvement Pulmonaire pour un Traitement Oncologique Application à la Radiothérapie et à l’ Hadronthérapie. *Thesis*, 2011.
- [70] H Ladjal, B Shariat, J Azencot, and M Beuve. Appropriate biomechanics and kinematics modeling of the respiratory system: Human diaphragm and thorax. In *2013 IEEE/RSJ International Conference on Intelligent Robots and Systems*, pages 2004–2009, 2013. ISBN 9781467363570. doi: 10.1109/IROS.2013.6696623. URL <https://ieeexplore.ieee.org/abstract/document/6696623/>.

- [71] Petru-stefan Manescu. Continuum description of deformable organs based on tetrahedral meshes : application to dosimetry and imaging for hadron therapy. *Thesis*, 2014.
- [72] Matthieu Giroux, Hamid Ladjal, Michael Beuve, and Behzad Shariat. Biomechanical patient-specific model of the respiratory system based on 4D CT scans and controlled by personalized physiological compliance. In *Lecture Notes in Computer Science (including sub-series Lecture Notes in Artificial Intelligence and Lecture Notes in Bioinformatics)*, volume 10434 LNCS, pages 216–223, 2017. ISBN 9783319661841. doi: 10.1007/978-3-319-66185-8_25. URL http://link.springer.com/10.1007/978-3-319-66185-8_{ }25.
- [73] Linda Hong, Michael Goitein, Marta Bucciolini, Robert Comiskey, Bernard Gottschalk, Skip Rosenthal, Chris Serago, and Marcia Urie. A pencil beam algorithm for proton dose calculations. *Physics in Medicine and Biology*, 41(8):1305–1330, aug 1996. ISSN 00319155. doi: 10.1088/0031-9155/41/8/005. URL <http://stacks.iop.org/0031-9155/41/i=8/a=005?key=crossref.009898f1ce8de9b24b06f05b05c8e9cb>.
- [74] Nobuyuki Kanematsu, Masataka Komori, Shunsuke Yonai, and Azusa Ishizaki. Dynamic splitting of Gaussian pencil beams in heterogeneity-correction algorithms for radiotherapy with heavy charged particles. *Physics in Medicine & Biology*, 54(7):2015, 2009. URL <http://iopscience.iop.org/article/10.1088/0031-9155/54/7/010/meta>.
- [75] Yusuke Egashira, Teiji Nishio, Taeko Matsuura, Satoru Kameoka, and Mitsuru Uesaka. Experimental evaluation of a spatial resampling technique to improve the accuracy of pencil-beam dose calculation in proton therapy. *Medical Physics*, 39(7):4104–4114, jun 2012. ISSN 00942405. doi: 10.1118/1.4722984. URL <http://doi.wiley.com/10.1118/1.4722984>.
- [76] Georgios Kalantzis, Theodora Leventouri, Hidenobu Tachibana, and Charles Shang. A GPU-based pencil beam algorithm for dose calculations in proton radiation therapy. In *Studies in Computational Intelligence*, volume 612, pages 17–29. Springer, Cham, 2016. doi: 10.1007/978-3-319-23509-7_2. URL http://link.springer.com/10.1007/978-3-319-23509-7_{ }2.
- [77] Paige A Taylor, Stephen F Kry, and David S Followill. Pencil Beam Algorithms Are Unsuitable for Proton Dose Calculations in Lung. *International Journal of Radiation Oncology Biology Physics*, 99(3):750–756, nov 2017. ISSN 1879355X. doi: 10.1016/j.ijrobp.2017.06.003. URL <http://www.ncbi.nlm.nih.gov/pubmed/2884337><http://www.pubmedcentral.nih.gov/articlerender.fcgi?artid=PMC5729062>.
- [78] M Lee, A E Nahum, and S Webb. An empirical method to build up a model of proton dose distribution for a radiotherapy treatment-planning package. *Physics in Medicine*

- and Biology*, 38(7):989–998, jul 1993. ISSN 00319155. doi: 10.1088/0031-9155/38/7/009. URL <http://stacks.iop.org/0031-9155/38/i=7/a=009?key=crossref.1be6b762055e84e2ab528d51fa0404b>.
- [79] Barbara Schaffner, Eros Pedroni, and Antony Lomax. Dose calculation models for proton treatment planning using a dynamic beam delivery system: An attempt to include density heterogeneity effects in the analytical dose calculation. *Physics in Medicine and Biology*, 44(1):27–41, jan 1999. ISSN 00319155. doi: 10.1088/0031-9155/44/1/004. URL <http://stacks.iop.org/0031-9155/44/i=1/a=004?key=crossref.5b31bofcofb8d274bd73e0975ca69b84>.
- [80] Kellie R Russell, Ulf Isacson, Mikael Saxner, Anders Ahnesjö, Anders Montelius, Erik Grusell, Christina Vallhagen Dahlgren, Stefan Lorin, and Bengt Glimelius. Implementation of pencil kernel and depth penetration algorithms for treatment planning of proton beams. *Physics in Medicine and Biology*, 45(1):9–27, jan 2000. ISSN 00319155. doi: 10.1088/0031-9155/45/1/302. URL <http://stacks.iop.org/0031-9155/45/i=1/a=302?key=crossref.3e6eddc54830f42fdd8ccdc4c905cf90>.
- [81] E. Pedroni, S Scheib, T Böhringer, Adolf Coray, M Grossmann, S Lin, and Antony Lomax. Experimental characterization and physical modelling of the dose distribution of scanned proton pencil beams. *Physics in Medicine and Biology*, 50(3):541–561, 2005. ISSN 0031-9155. doi: 10.1088/0031-9155/50/3/011.
- [82] W Newhauser. Dosimetry for the gantry beams at the northeast proton therapy center. *Dimensions and geometric relationships Massachusetts General Hospital Report HD-112*, 2001.
- [83] Iwan Kawrakow and Matthias Fippel. VMC++, a fast MC algorithm for radiation treatment planning. In *The Use of Computers in Radiotherapy, XIIIth Int'l Conf., Heidelberg*, pages 126–128, Berlin, Heidelberg, 2000. Springer Berlin Heidelberg. doi: 10.1007/978-3-642-59758-9. URL http://link.springer.com/10.1007/978-3-642-59758-9_{ }46.
- [84] I. Kawrakow. Accurate condensed history Monte Carlo simulation of electron transport. I. EGSnrc, the new EGS4 version. *Medical Physics*, 27(3):485–498, mar 2000. ISSN 00942405. doi: 10.1118/1.598917. URL <http://doi.wiley.com/10.1118/1.598917>.
- [85] Marco Schwarz. Treatment planning in proton therapy. *The European Physical Journal Plus*, 126(7):1–19, 2011. ISSN 2190-5444. doi: 10.1140/epjp/i2011-11067-y. URL <https://link.springer.com/article/10.1140/epjp/i2011-11067-y>.
- [86] Alfredo Ferrari and Others. FLUKA: A multi-particle transport code (Program version 2005). *Cern-2005-010*, (October), 2005. doi: 10.5170/cern-2005-010. URL <http://inspirehep.net/record/701721/files/slac-r-773.pdf>.

- [87] TT Böhlen, F Cerutti, MPW Chin, A Fassò, A. Ferrari, P.G. Ortega, A. Mairani, P.R. Sala, G. Smirnov, and V. Vlachoudis. The FLUKA Code: Developments and Challenges for High Energy and Medical Applications. *Nuclear Data Sheets*, 120: 211–214, 2014. ISSN 00903752. doi: 10.1016/j.nds.2014.07.049. URL <https://www.sciencedirect.com/science/article/pii/S0090375214005018><http://linkinghub.elsevier.com/retrieve/pii/S0090375214005018>.
- [88] S. Agostinelli, J. Allison, K. Amako, J. Apostolakis, H. Araujo, P. Arce, M. Asai, D. Axen, S. Banerjee, G. Barrant, F. Behner, L. Bellagamba, J. Boudreau, L. Broglia, A. Brunengo, H. Burkhardt, S. Chauvie, J. Chuma, R. Chytráček, G. Cooperman, G. Cosmo, P. Degt-yarenko, A. Dell’Acqua, G. Depaola, D. Dietrich, R. Enami, A. Feliciello, C. Ferguson, H. Fesefeldt, G. Folger, F. Foppiano, A. Forti, S. Garelli, S. Giani, R. Giannitrapani, D. Gibin, J. J. Gomez Cadenas, I. Gonzalez, G. Gracia Abril, G. Greeniaus, W. Greiner, V. Grichine, A. Grossheim, S. Guatelli, P. Gumplinger, R. Hamatsu, K. Hashimoto, H. Hasui, A. Heikkinen, A. Howard, V. Ivanchenko, A. Johnson, F. W. Jones, J. Kallenbach, N. Kanaya, M. Kawabata, Y. Kawabata, M. Kawaguti, S. Kelner, P. Kent, A. Kimura, T. Kodama, R. Kokoulin, M. Kossov, H. Kurashige, E. Lamanna, T. Lampen, V. Lara, V. Lefebvre, F. Lei, M. Liendl, W. Lockman, F. Longo, S. Magni, M. Maire, E. Medernach, K. Minamimoto, P. Mora de Freitas, Y. Morita, K. Murakami, M. Nagamatu, R. Nartallo, P. Nieminen, T. Nishimura, K. Ohtsubo, M. Okamura, S. O’Neale, Y. Oohata, K. Paech, J. Perl, A. Pfeiffer, M. G. Pia, F. Ranjard, A. Rybin, S. Sadilov, E. di Salvo, G. Santin, T. Sasaki, N. Savvas, Y. Sawada, S. Scherer, S. Sei, V. Sirotenko, D. Smith, N. Starkov, H. Stoecker, J. Sulkimo, M. Takahata, S. Tanaka, E. Tcherniaev, E. Safai Tehrani, M. Tropeano, P. Truscott, H. Uno, L. Urban, P. Urban, M. Verderi, A. Walkden, W. Wander, H. Weber, J. P. Wellisch, T. Wenaus, D. C. Williams, D. Wright, T. Yamada, H. Yoshida, and D. Zschesche. GEANT4 - A simulation toolkit. *Nuclear Instruments and Methods in Physics Research, Section A: Accelerators, Spectrometers, Detectors and Associated Equipment*, 506(3):250–303, jul 2003. ISSN 01689002. doi: 10.1016/S0168-9002(03)01368-8. URL <http://linkinghub.elsevier.com/retrieve/pii/S0168900203013688><http://www.sciencedirect.com/science/article/pii/S0168900203013688>.
- [89] J Allison, K Amako, J Apostolakis, P Arce, M Asai, T Aso, E Bagli, A Bagulya, S Banerjee, G Barrant, B R Beck, A G Bogdanov, D Brandt, J M C Brown, H Burkhardt, Ph. Canal, D Cano-Ott, S Chauvie, K Cho, G A P Cirrone, G Cooperman, M A Cortés-Giraldo, G Cosmo, G Cuttone, G Depaola, L Desorgher, X Dong, A Dotti, V D Elvira, G Folger, Z Francis, A Galoyan, L Garnier, M Gayer, K L Genser, V M Grichine, S Guatelli, P Guèye, P Gumplinger, A S Howard, I Hřivnáčová, S Hwang, S Incerti, A Ivanchenko, V N Ivanchenko, F W Jones, S Y Jun, P Kaitaniemi, N Karakatsanis, M Karamitros, M Kelsey, A Kimura, T Koi, H Kurashige, A Lechner, S B Lee, F Longo, M Maire, D Mancusi, A Man-

- tero, E Mendoza, B Morgan, K Murakami, T Nikitina, L Pandola, P Paprocki, J Perl, I Petrović, M G Pia, W Pokorski, J M Quesada, M Raine, M A Reis, A Ribon, A Ristić Fira, F Romano, G Russo, G Santin, T Sasaki, D Sawkey, J I Shin, I I Strakovsky, A Taborda, S Tanaka, B Tomé, T Toshito, H N Tran, P R Truscott, L Urban, V Uzhinsky, J M Verbeke, M Verderi, B L Wendt, H Wenzel, D H Wright, D M Wright, T Yamashita, J Yarba, and H Yoshida. Recent developments in Geant4. *Nuclear Instruments and Methods in Physics Research Section A: Accelerators, Spectrometers, Detectors and Associated Equipment*, 835:186–225, 2016. ISSN 0168-9002. doi: <https://doi.org/10.1016/j.nima.2016.06.125>. URL <http://www.sciencedirect.com/science/article/pii/S0168900216306957>.
- [90] Laurie S Waters and Others. MCNPX user’s manual. *Los Alamos National Laboratory*, 2002.
- [91] D B Pelowitz. MCNPX user’s manual, version 2.6.0, LA-CP-07-1473. *Los Alamos National Laboratory, Los Alamos (NM)*, 2008.
- [92] Matthias Fippel and Martin Soukup. A Monte Carlo dose calculation algorithm for proton therapy. *Medical Physics*, 31(8):2263–2273, jul 2004. ISSN 00942405. doi: 10.1118/1.1769631. URL <http://doi.wiley.com/10.1118/1.1769631>.
- [93] A. V. Dementyev and N. M. Sobolevsky. SHIELD - universal Monte Carlo hadron transport code: scope and applications. *Radiation Measurements*, 30(5):553–557, 1999. ISSN 13504487. doi: 10.1016/S1350-4487(99)00231-0. URL <https://www.sciencedirect.com/science/article/pii/S1350448799002310>.
- [94] Jia Wei Zhang, Gai Ge Wang, Andrea Valsecchi, Sergio Damas, Aristeidis Sotiras, Christos Davatzikos, Nikos Paragios, Flavio Luiz Seixas, Luiz Satoru Ochi, Aura Conci, Débora Muchaluat Saade, J. Santamaría, Osacar Cordón, Sergio Damas, I. Aleman, and M. Botella. Deformable medical image registration: A survey. *IEEE Transactions on Medical Imaging*, 32(9):819–828, 2012. ISSN 14327643. doi: 10.1007/s00500-006-0132-0. URL <http://portal.acm.org/citation.cfm?doid=1389095.1389320><http://adsabs.harvard.edu/abs/2012AMM...203...88Z>.
- [95] Lisa Gottesfeld Brown. A survey of image registration techniques. *ACM Computing Surveys*, 24(4):325–376, 1992. ISSN 03600300. doi: 10.1145/146370.146374. URL <http://citeseerx.ist.psu.edu/viewdoc/download?doi=10.1.1.740.3626&rep=rep1&type=pdf><http://portal.acm.org/citation.cfm?doid=146370.146374>.
- [96] Eldad Haber and Jan Modersitzki. Numerical methods for volume preserving image registration. *Inverse Problems*, 20(5):1621–1638, oct 2004. ISSN 02665611. doi:

- 10.1088/0266-5611/20/5/018. URL <http://stacks.iop.org/0266-5611/20/i=5/a=018?key=crossref.c73c2af281f824084ae90991170a938b>.
- [97] A. Behan. 2-D and 3-D Image Registration For Medical, Remote Sensing, and Industrial Applications. *The Photogrammetric Record*, 21(114):180–181, jun 2006. ISSN 0031-868X. doi: 10.1111/j.1477-9730.2006.00375_1.x. URL http://doi.wiley.com/10.1111/j.1477-9730.2006.00375_1.x.
- [98] Medha V Wyawahare, Hemant K Abhyankar, Pradeep M Patil, and Hemant K Abhyankar. Image Registration Techniques: An overview. *International Journal of Signal Processing, Image Processing and Pattern Recognition*, 2(3):11–28, 2009. ISSN 2005-4254. URL <http://citeseerx.ist.psu.edu/viewdoc/download?doi=10.1.1.177.5585&rep=rep1&type=pdf>.
- [99] Jasdeep Kaur and Amanpreet Kaur. Image Registration : A Survey. *IJSRD - International Journal for Scientific Research & Development*, 2(05):371–373, 2014. URL <https://www.sciencedirect.com/science/article/pii/S0262885603001379>.
- [100] Francisco P.M. Oliveira and João Manuel R.S. Tavares. Medical image registration: A review. *Computer Methods in Biomechanics and Biomedical Engineering*, 17(2):73–93, jan 2014. ISSN 10255842. doi: 10.1080/10255842.2012.670855. URL <http://www.tandfonline.com/doi/abs/10.1080/10255842.2012.670855>.
- [101] Richard Castillo, Edward Castillo, Rudy Guerra, Valen E Johnson, Travis Mcphail, Amit K Garg, and Thomas Guerrero. A framework for evaluation of deformable image registration spatial accuracy using large landmark point sets. *Physics in Medicine and Biology*, 54(7):1849–1870, 2009. doi: 10.1088/0031-9155/54/7/001.
- [102] Kujtim Latifi, Geoffrey Zhang, Marnix Stawicki, Wouter van Elmpt, Andre Dekker, and Kenneth Forster. Validation of three deformable image registration algorithms for the thorax. *Journal of Applied Clinical Medical Physics*, 14(1):19–30, jan 2013. ISSN 15269914. doi: 10.1120/jacmp.v14i1.3834. URL <http://doi.wiley.com/10.1120/jacmp.v14i1.3834>.
- [103] Monica Serban, Emily Heath, Gabriela Stroian, D. Louis Collins, and Jan Seuntjens. A deformable phantom for 4D radiotherapy verification: Design and image registration evaluation. *Medical Physics*, 35(3):1094–1102, feb 2008. ISSN 00942405. doi: 10.1118/1.2836417. URL <http://doi.wiley.com/10.1118/1.2836417>.
- [104] U J Yeo, M L Taylor, J R Supple, R L Smith, L Dunn, T Kron, and R D Franich. Is it sensible to “deform” dose? 3D experimental validation of dose-warping. *Medical physics*, 39(8):5065–5072, aug 2012. ISSN 0094-2405 (Print). doi: 10.1118/1.4736534.

- [105] B. Gino Fallone, D. Ryan C. Rivest, Terence A. Riauka, and Albert D. Murtha. Assessment of a commercially available automatic deformable registration system. *Journal of Applied Clinical Medical Physics*, 11(3):101–123, jun 2010. ISSN 15269914. doi: 10.1120/jacmp.v11i3.3175. URL <http://doi.wiley.com/10.1120/jacmp.v11i3.3175>.
- [106] A. Mencarelli, S. van Beek, S. van Kranen, C. Rasch, M. van Herk, and J.-J. Sonke. Validation of deformable registration in head and neck cancer using analysis of variance. *Medical Physics*, 39(11):6879–6884, oct 2012. ISSN 00942405. doi: 10.1118/1.4760990. URL <http://doi.wiley.com/10.1118/1.4760990>.
- [107] Kristy K Brock, Deformable Registration Accuracy Consortium, and Others. Results of a multi-institution deformable registration accuracy study (MIDRAS). *International Journal of Radiation Oncology* Biology* Physics*, 76(2):583–596, 2010.
- [108] JOHN B West and Frank L Matthews. Stresses, strains, and surface pressures in the lung caused by its weight. *Journal of Applied Physiology*, 32(3):332—34, 1972. URL <https://www.physiology.org/doi/abs/10.1152/jappl.1972.32.3.332>.
- [109] J Mead, T Takishima, and D Leith. Stress distribution in lungs: a model of pulmonary elasticity. *Journal of applied physiology*, 28(5):596–608, 1970. ISSN 0021-8987. doi: 10.1152/jappl.1970.28.5.596. URL <https://www.physiology.org/doi/abs/10.1152/jappl.1970.28.5.596><http://www.ncbi.nlm.nih.gov/pubmed/5442255>.
- [110] R Werner, J Ehrhardt, R Schmidt, and H Handels. Patient-specific finite element modeling of respiratory lung motion using 4D CT image data. *Med Phys*, 36(5):1500–1511, 2009. URL <http://www.ncbi.nlm.nih.gov/pubmed/19544766>.
- [111] Jaesung Eom, Chengyu Shi, Xie George Xu, and Suvranu De. Modeling respiratory motion for cancer radiation therapy based on patient-specific 4DCT data. In *Lecture Notes in Computer Science (including subseries Lecture Notes in Artificial Intelligence and Lecture Notes in Bioinformatics)*, volume 5762 LNCS, pages 348–355, 2009. ISBN 3642042708. doi: 10.1007/978-3-642-04271-3_43. URL https://link.springer.com/chapter/10.1007/978-3-642-04271-3_43.
- [112] Adil Al-Mayah, Joanne Moseley, Mike Velec, and Kristy Brock. Effect of friction and material compressibility on deformable modeling of human lung. In *Lecture Notes in Computer Science (including subseries Lecture Notes in Artificial Intelligence and Lecture Notes in Bioinformatics)*, volume 5104 LNCS, pages 98–106, Berlin, Heidelberg, 2008. Springer Berlin Heidelberg. ISBN 3540705201. doi: 10.1007/978-3-540-70521-5_11. URL http://link.springer.com/10.1007/978-3-540-70521-5_11.

- [113] a Al-Mayah, J Moseley, and K K Brock. Contact surface and material nonlinearity modeling of human lungs. *Physics in medicine and biology*, 53(1):305–17, 2008. ISSN 0031-9155. doi: 10.1088/0031-9155/53/1/022. URL <http://www.ncbi.nlm.nih.gov/pubmed/18182705>.
- [114] A. Al-Mayah, J. Moseley, M. Velec, and K. K. Brock. Sliding characteristic and material compressibility of human lung: Parametric study and verification. *Medical Physics*, 36(10):4625–4633, sep 2009. ISSN 00942405. doi: 10.1118/1.3218761. URL <http://doi.wiley.com/10.1118/1.3218761>.
- [115] Elham Karami, Stewart Gaede, Ting-Yim Lee, and Abbas Samani. A biomechanical approach for *in vivo* lung tumor motion prediction during external beam radiation therapy. page 941512, 2015. ISSN 16057422. doi: 10.1117/12.2082447. URL <http://proceedings.spiedigitallibrary.org/proceeding.aspx?doi=10.1117/12.2082447>.
- [116] Hamid Ladjal, Joseph Azencot, Michaël Beuve, Philippe Giraud, and Behzad Shariat. Biomechanical Modeling of the Respiratory System: Human Diaphragm and Thorax. pages 101–115, sep 2014. URL <https://hal.archives-ouvertes.fr/hal-01267706>.
- [117] Hamid Ladjal, Nadir Skendraoui, Matthieu Giroux, Yazid Touileb, Joseph Azencot, Michael Beuve, Philippe Giraud, and Behzad Shariat. Physiological and Biomechanical Model of Patient Specific Lung Motion Based on 4D CT Images. pages 1—5, nov 2015. URL <https://hal.archives-ouvertes.fr/hal-01214310>.
- [118] M. Giroux, H. Ladjal, M. Beuve, P. Giraud, and B. Shariat. Patient-Specific Biomechanical Modeling of the Lung Tumor for Radiation Therapy. *Computer Methods in Biomechanics and Biomedical Engineering*, 20(sup1):95–96, oct 2017. ISSN 1025-5842. doi: 10.1080/10255842.2017.1382878. URL <https://www.tandfonline.com/doi/full/10.1080/10255842.2017.1382878>.
- [119] JR McClelland, DJ Hawkes, T Schaeffter, and AP King. Respiratory motion models: a review. *Medical image analysis*, 2013. URL <http://www.sciencedirect.com/science/article/pii/S136184151200134X>.
- [120] D Sarrut, J Vandemeulebroucke, and S Rit. Intensity-based deformable registration: Introduction and overview. *4D Modeling and Estimation of*, 2013. URL http://link.springer.com/chapter/10.1007/978-3-642-36441-9_{_}6.
- [121] Fassi Aurora, Matteo Seregni, Marco Riboldi, Pietro Cerveri, David Sarrut, Ivaldi Giovanni Battista, Paola Tabarelli De Fatis, Marco Liotta, and Guido Baroni. Surrogate-driven deformable motion model for organ motion tracking in particle radiation therapy. *Physics in*

- medicine*, 2015. URL <http://iopscience.iop.org/article/10.1088/0031-9155/60/4/1565/meta>.
- [122] MC Han, JM Seo, SH Lee, and CH Kim. Continuously Deforming 4D Voxel Phantom for Realistic Representation of Respiratory Motion in Monte Carlo Dose Calculation. *IEEE Transactions on Nuclear Science*, 63:2918–2924, 2016. URL <http://ieeexplore.ieee.org/abstract/document/7546842/>.
- [123] JR McClelland, M Modat, and S Arridge. A generalized framework unifying image registration and respiratory motion models and incorporating image reconstruction, for partial image data or full images. *Physics in Medicine*, 2017. URL <http://iopscience.iop.org/article/10.1088/1361-6560/aa6070/meta>.
- [124] DA Rajon, DW Jokisch, PW Patton, and AP Shah. Voxel size effects in three-dimensional nuclear magnetic resonance microscopy performed for trabecular bone dosimetry. *Medical*, 2000. URL <http://onlinelibrary.wiley.com/doi/10.1118/1.1315313/full>.
- [125] WP Segars. Development and application of the new dynamic Nurbs-based Cardiac-Torso (NCAT) phantom. 2002. URL <https://elibrary.ru/item.asp?id=5227329>.
- [126] C Lee, D Lodwick, and D Hasenauer. Hybrid computational phantoms of the male and female newborn patient: NURBS-based whole-body models. *Physics in medicine*, 2007. URL <http://iopscience.iop.org/article/10.1088/0031-9155/52/12/001/meta>.
- [127] XG Xu, V Taranenko, and J Zhang. A boundary-representation method for designing whole-body radiation dosimetry models: pregnant females at the ends of three gestational periods—RPI-P3,-P6 and-. *Physics in medicine and*, 2007. URL <http://iopscience.iop.org/article/10.1088/0031-9155/52/23/017/meta>.
- [128] J Zhang, YH Na, and PF Caracappa. RPI-AM and RPI-AF, a pair of mesh-based, size-adjustable adult male and female computational phantoms using ICRP-89 parameters and their calculations for organ. *Physics in medicine and*, 2009. URL <http://iopscience.iop.org/article/10.1088/0031-9155/54/19/015/meta>.
- [129] J Zhang, XG Xu, C Shi, and M Fuss. Development of a geometry-based respiratory motion-simulating patient model for radiation treatment dosimetry. *Journal of Applied clinical*, 2008. URL <http://onlinelibrary.wiley.com/doi/10.1120/jacmp.v9i11.2700/full>.
- [130] A Christ, W Kainz, EG Hahn, and K Honegger. The Virtual Family—development of surface-based anatomical models of two adults and two children for dosimetric simulations. *Physics in medicine*, 2009. URL <http://iopscience.iop.org/article/10.1088/0031-9155/55/2/N01/meta>.

- [131] R Kramer, VF Cassola, and HJ Khoury. FASH and MASH: female and male adult human phantoms based on polygon mesh surfaces: II. Dosimetric calculations. *Physics in medicine*, 2009. URL <http://iopscience.iop.org/article/10.1088/0031-9155/55/1/010/meta>.
- [132] VF Cassola, VJ de Melo Lima, and R Kramer. FASH and MASH: female and male adult human phantoms based on polygon mesh surfaces: I. Development of the anatomy. *Physics in medicine*, 2009. URL <http://iopscience.iop.org/article/10.1088/0031-9155/55/1/009/meta>.
- [133] A Christ, W Kainz, EG Hahn, and K Honegger. The Virtual Family—development of surface-based anatomical models of two adults and two children for dosimetric simulations. *Physics in medicine*, 2009. URL <http://iopscience.iop.org/article/10.1088/0031-9155/55/2/N01/meta>.
- [134] WP Segars, G Sturgeon, and S Mendonca. 4D XCAT phantom for multimodality imaging research. *Medical*, 2010. URL <http://onlinelibrary.wiley.com/doi/10.1118/1.3480985/full>.
- [135] CH Kim, JH Jeong, WE Bolch, and KW Cho. A polygon-surface reference Korean male phantom (PSRK-Man) and its direct implementation in Geant4 Monte Carlo simulation. *Physics in medicine*, 2011. URL <http://iopscience.iop.org/article/10.1088/0031-9155/56/10/016/meta>.
- [136] Thomas Barker, Adam Bird, Roger Thetford Serco, and Andrew Cooper. Use of Tetrahedral Mesh Geometry to import a converted CAD file for Shielding and Criticality calculations with MONK and MCBEND. *Proc. 11th International Conference on Radiation Shielding (ICRS-11) and 14th Topical Meeting on Radiation Protection and Shielding (RPS-2008), USA (2008)*, 2008. URL http://answerssoftwareservice.com/resource/pdfs/icrs2008_{_}tetmesh.pdf.
- [137] Thomas Barker, Adam Bird, and Roger Thetford. CAD import for MONK and MCBEND by converting to Tetrahedral Mesh format. *Representations*, 99:570–571, 2008. ISSN 0003018X. URL http://answerssoftwareservice.com/resource/pdfs/answ2008_{_}tetmesh.pdf.
- [138] Qianqian Fang. Mesh-based Monte Carlo method using fast ray-tracing in Plücker coordinates. *Biomedical Optics Express*, 1(1):165, aug 2010. ISSN 2156-7085. doi: 10.1364/BOE.1.000165. URL http://www.ncbi.nlm.nih.gov/entrez/query.fcgi?cmd=Retrieve{&}db=PubMed{&}dopt=Citation{&}list{_}uids=21170299https://www.osapublishing.org/abstract.cfm?URI=boe-1-1-165.

- [139] H Shen and G Wang. A tetrahedron-based inhomogeneous Monte Carlo optical simulator. *Physics in Medicine and Biology*, 55(4):947–962, feb 2010. ISSN 0031-9155. doi: 10.1088/0031-9155/55/4/003. URL <http://iopscience.iop.org/article/10.1088/0031-9155/55/4/003/metahttp://stacks.iop.org/0031-9155/55/i=4/a=003?key=crossref.b42a2fob4296c7667495f2ad82c47b55>.
- [140] Gabriel Paiva Fonseca, Guillaume Landry, Shane White, Michel D’Amours, Hélio Yoriyaz, Luc Beaulieu, Brigitte Reniers, and Frank Verhaegen. The use of tetrahedral mesh geometries in Monte Carlo simulation of applicator based brachytherapy dose distributions. *Physics in medicine and biology*, 59(19):5921–35, oct 2014. ISSN 1361-6560. doi: 10.1088/0031-9155/59/19/5921. URL <http://www.ncbi.nlm.nih.gov/pubmed/25210788http://stacks.iop.org/0031-9155/59/i=19/a=5921?key=crossref.6d7ebdd7e1ad8d23f36c5f3eaac12c00>.
- [141] Christopher M. Poole, Iwan Cornelius, Jamie V. Trapp, and Christian M. Langton. A CAD interface for GEANT4. *Australasian physical & engineering sciences in medicine*, 35(3):329–34, sep 2012. ISSN 0158-9938. doi: 10.1007/s13246-012-0159-8. URL <http://link.springer.com/10.1007/s13246-012-0159-8http://arxiv.org/abs/1105.0963http://www.ncbi.nlm.nih.gov/pubmed/22956356>.
- [142] Tejinder Kataria, Kuldeep Sharma, Vikraman Subramani, KP Karrthick, and ShyamS Bisht. Homogeneity Index: An objective tool for assessment of conformal radiation treatments. *Journal of Medical Physics*, 37(4):207, oct 2012. ISSN 0971-6203. doi: 10.4103/0971-6203.103606. URL <http://www.ncbi.nlm.nih.gov/pubmed/23293452http://www.pubmedcentral.nih.gov/articlerender.fcgi?artid=PMC3532749http://www.jmp.org.in/text.asp?2012/37/4/207/103606>.
- [143] S Agostinelli, J Allison, K Amako, and Others. Geant4 – a simulation toolkit. *Nuclear Instruments and Methods in Physics Research A*, 506(506):250–303, 2003. ISSN 01689002. doi: 10.1016/S0168-9002(03)01368-8.
- [144] John Allison, Katsuya Amako, Jea Apostolakis, HAAH Araujo, P Arce Dubois, MAAM Asai, GABG Barrand, RACR Capra, SACS Chauvie, RACR Chytracak, and Others. Geant4 developments and applications. *IEEE Transactions on Nuclear Science*, 53(1):270–278, 2006. ISSN 00189499. doi: 10.1109/TNS.2006.869826. URL http://ieeexplore.ieee.org/xpls/abs/_all.jsp?arnumber=1610988.
- [145] Yeon Soo Yeom, Jong Hwi Jeong, Min Cheol Han, and Chan Hyeong Kim. Tetrahedral-mesh-based computational human phantom for fast Monte Carlo dose calculations. *Physics in medicine and biology*, 59(12):3173–85, jun 2014. ISSN 1361-6560. doi:

- 10.1088/0031-9155/59/12/3173. URL <http://www.ncbi.nlm.nih.gov/pubmed/24862061><http://stacks.iop.org/0031-9155/59/i=12/a=3173?key=crossref.a0e8117a4ec425d9367e2c33b3037339>.
- [146] Chan Hyeong Kim, Jong Hwi Jeong, Wesley E Bolch, Kun-Woo Cho, and Sung Bae Hwang. A polygon-surface reference Korean male phantom (PSRK-Man) and its direct implementation in Geant4 Monte Carlo simulation. *Physics in Medicine and Biology*, 56(10):3137–3161, may 2011. ISSN 0031-9155. doi: 10.1088/0031-9155/56/10/016. URL <http://stacks.iop.org/0031-9155/56/i=10/a=016?key=crossref.828cb7bad5e72fc9259c61d67d55cabe>.
- [147] Michael Velec, JL Joanne L Moseley, Tim Craig, Laura A Dawson, and Kristy K Brock. Accumulated dose in Liver Stereotactic-Body Radiotherapy: Positioning, Breathing and Deformation Effects. *International Journal of*, 83(4):1132–1140, 2012. URL <http://www.sciencedirect.com/science/article/pii/S0360301611033189>.
- [148] K L Ishikawa, S Takagi, K Matthys, and S Wada. 4D Monte Carlo Dose Calculations for Particle Therapy Combined with the Spring Network Model of Lung Motion. In *World Congress on Medical Physics and Biomedical Engineering, September 7-12, 2009, Munich, Germany*, pages 183–186. Springer, Springer Berlin Heidelberg, 2009. ISBN 978-3-642-03474-9. doi: 10.1007/978-3-642-03474-9_52. URL http://link.springer.com/10.1007/978-3-642-03474-9_{_}52.
- [149] Min Cheol Han, Yeon Soo Yeom, Chan Hyeong Kim, Seonghoon Kim, and Jason W Sohn. New approach based on tetrahedral-mesh geometry for accurate 4D Monte Carlo patient-dose calculation. *Physics in medicine and biology*, 60(4):1601–12, feb 2015. ISSN 1361-6560. doi: 10.1088/0031-9155/60/4/1601. URL <http://www.ncbi.nlm.nih.gov/pubmed/25615567><http://stacks.iop.org/0031-9155/60/i=4/a=1601?key=crossref.od7a2eb6c004fce329f460dcba96a4aa>.
- [150] Petru Manescu, Joseph Azencot, Michael Beuve, Hamid Ladjal, and Jacques Saad. Material density mapping on deformable 3D models of human organs. *International Journal of Biomedical and Biological Engineering*, 6(6):215–224, 2012. ISSN 1307-6892. URL <http://waset.org/Publications?p=66>.
- [151] Petru Manescu, Hamid Ladjal, Joseph Azencot, Michael Beuve, Etienne Testa, and Behzad Shariat. Four-dimensional radiotherapeutic dose calculation using biomechanical respiratory motion description. *International Journal of Computer Assisted Radiology and Surgery*, 9(3):449–457, may 2014. ISSN 1861-6410. doi: 10.1007/s11548-013-0935-2. URL <http://dx.doi.org/10.1007/s11548-013-0935-2><http://link.springer.com/>

- article/10.1007/s11548-013-0935-2<http://link.springer.com/10.1007/s11548-013-0935-2>.
- [152] Yazid Touileb, Petru Manescu, Hamid Ladjal, Joseph Azencot, Michael Beuve, and Behzad Shariat. Motion-induced Monte Carlo dose calculation using deformable tetrahedral meshes. In *2016 IEEE 13th International Symposium on Biomedical Imaging (ISBI)*, pages 1257–1260. IEEE, apr 2016. ISBN 978-1-4799-2349-6. doi: 10.1109/ISBI.2016.7493495. URL <http://ieeexplore.ieee.org/document/7493495/>.
- [153] Wilfried Schneider, Thomas Bortfeld, and Wolfgang Schlegel. Correlation between CT numbers and tissue parameters needed for Monte Carlo simulations of clinical dose distributions. *Physics in Medicine and Biology*, 45(2):459–478, 2000. ISSN 0031-9155. doi: 10.1088/0031-9155/45/2/314. URL <http://stacks.iop.org/0031-9155/45/i=2/a=314?key=crossref.e78c9ce7980571a8752f2265863c8960>.
- [154] A Yezzi, S Kichenassamy, A Kumar, P Olver, and A Tannenbaum. A geometric snake model for segmentation of medical imagery. *IEEE Transactions on Medical Imaging*, 16(2):199–209, apr 1997. ISSN 02780062. doi: 10.1109/42.563665. URL <http://ieeexplore.ieee.org/lpdocs/epic03/wrapper.htm?arnumber=563665>.
- [155] William E. Lorensen and Harvey E. Cline. Marching cubes: A high resolution 3D surface construction algorithm. In *Proceedings of the 14th annual conference on Computer graphics and interactive techniques - SIGGRAPH '87*, volume 21, pages 163–169. ACM, 1987. ISBN 0897912276. doi: 10.1145/37402.37422. URL <http://portal.acm.org/citation.cfm?doid=37401.37422>.
- [156] Marco Attene and Bianca Falcidieno. ReMESH: An interactive environment to edit and repair triangle meshes. In *Proceedings - IEEE International Conference on Shape Modeling and Applications 2006, SMI 2006*, volume 2006, page 41. IEEE, 2006. ISBN 0769525911. doi: 10.1109/SMI.2006.29.
- [157] David F Watson. Computing the n-dimensional Delaunay tessellation with application to Voronoi polytopes. *The computer journal*, 24(2):167—172, 1981. URL <https://academic.oup.com/comjnl/article-abstract/24/2/167/338200>.
- [158] Hang Si. TetGen, a Delaunay-Based Quality Tetrahedral Mesh Generator. *ACM Transactions on Mathematical Software*, 41(2):1–36, feb 2015. ISSN 00983500. doi: 10.1145/2629697. URL <http://doi.acm.org/10.1145/2629697><http://dl.acm.org/citation.cfm?doid=2732672.2629697>.

- [159] Hualiang Zhong and Jeffrey V Siebers. Monte Carlo dose mapping on deforming anatomy. *Physics in medicine and biology*, 54(19):5815–5830, 2009. ISSN 0031-9155. doi: 10.1088/0031-9155/54/19/010.
- [160] Christopher M. Poole, Iwan Cornelius, Jamie V. Trapp, and Christian M. Langton. Fast tessellated solid navigation in GEANT4. *IEEE Transactions on Nuclear Science*, 59(4 PART 3):1695–1701, 2012. ISSN 00189499. doi: 10.1109/TNS.2012.2197415. URL <https://ieeexplore.ieee.org/abstract/document/6213169/>.
- [161] Gee JC; Gerig G Yushkevich, PA; Piven J; Hazlett HC; Smith RG; Ho S. user.guide 3 D active contour segmentation of anatomical structures: significantly improved efficiency and reliability. *neuroImage*, 31(3):2006, 2006. URL <http://eutils.ncbi.nlm.nih.gov/entrez/eutils/elink.fcgi?dbfrom=pubmed&id=16545965&retmode=ref&cmd=prlinks%}5Cnpapers3://publication/doi/10.1016/j.neuroimage.2006.01.015>.
- [162] Edward Castillo, Richard Castillo, Josue Martinez, Maithili Shenoy, and Thomas Guerrero. Four-dimensional deformable image registration using trajectory modeling. *Physics in Medicine and Biology*, 55(1):305–327, jan 2010. ISSN 0031-9155. doi: 10.1088/0031-9155/55/1/018. URL <http://stacks.iop.org/0031-9155/55/i=1/a=018?key=crossref.6fc8715afe2ba47d2a2a3dc153eb2e21>.
- [163] Hang Si. On refinement of constrained delaunay tetrahedralizations. *Proceedings of the 15th International Meshing Roundtable, IMR 2006*, m:509–528, 2006. doi: 10.1007/978-3-540-34958-7_29.
- [164] Stefan Klein, Marius Staring, Keelin Murphy, and Josien PW Viergever, Max A and Pluim. Elastix: a toolbox for intensity-based medical image registration. *IEEE Transactions on Medical Imaging*, 29(1):196–205, jan 2010. ISSN 0278-0062. doi: 10.1109/TMI.2009.2035616.
- [165] Tejinder Kataria, Kuldeep Sharma, Vikraman Subramani, KP Karrthick, and ShyamS Bisht. Homogeneity Index: An objective tool for assessment of conformal radiation treatments. *Journal of Medical Physics*, 37(4):207, oct 2012. ISSN 0971-6203. doi: 10.4103/0971-6203.103606. URL <http://www.pubmedcentral.nih.gov/articlerender.fcgi?artid=3532749&tool=pmcentrez&rendertype=abstracthttp://www.jmp.org.in/text.asp?2012/37/4/207/103606>.
- [166] Carl Lederman, Anand Joshi, Ivo Dinov, Luminita Vese, Arthur Toga, and John Darrell Van Horn. The generation of tetrahedral mesh models for neuroanatomical MRI. *NeuroImage*, 55(1):153–164, mar 2011. ISSN 10538119. doi: 10.1016/j.neuroimage.2010.11.013. URL <http://www.sciencedirect.com/science/article/pii/S1053811910014436>.

- [167] David Sarrut and Laurent Guigues. Region-oriented CT image representation for reducing computing time of Monte Carlo simulations. *Medical Physics*, 35(4):1452, 2008. ISSN 00942405. doi: 10.1118/1.2884854. URL <http://scitation.aip.org/content/aapm/journal/medphys/35/4/10.1118/1.2884854>.
- [168] AN Chernikov and NP Chrisochoides. Tetrahedral image-to-mesh conversion for biomedical applications. *Proceedings of the 2nd ACM Conference on Bioinformatics, Computational Biology and Biomedicine*, 2011. doi: 10.1145/2147805.2147819. URL <http://dl.acm.org/citation.cfm?id=2147819>.
- [169] Andrey N. Chernikov and Nikos P. Chrisochoides. Multitissue Tetrahedral Image-to-mesh Conversion with Guaranteed Quality and Fidelity. <Http://Dx.Doi.Org/10.1137/100815256>, 2011. ISSN 1064-8275. doi: 10.1137/100815256. URL <http://epubs.siam.org/doi/abs/10.1137/100815256>.
- [170] Qianqian Fang and David A. Boas. Tetrahedral mesh generation from volumetric binary and grayscale images. *Proceedings - 2009 IEEE International Symposium on Biomedical Imaging: From Nano to Macro, ISBI 2009*, pages 1142–1145, 2009. ISSN 1945-7928. doi: 10.1109/ISBI.2009.5193259. URL http://ieeexplore.ieee.org/xpls/abs/_all.jsp?arnumber=5193259.
- [171] O Courchesne and F Guibault. Adaptive mesh generation of MRI images for 3D reconstruction of human trunk. *Image Analysis and ...*, 2007. ISSN 03029743 16113349. URL http://link.springer.com/chapter/10.1007/978-3-540-74260-9_{ }92.
- [172] O. Courchesne, F. Guibault, S. Parent, and F. Cheriet. Patient-specific anisotropic model of human trunk based on MR data. *INTERNATIONAL JOURNAL FOR NUMERICAL METHODS IN BIOMEDICAL ENGINEERING*, 31(9), 2015. ISSN 20407947 20407939. doi: 10.1002/cnm.2724. URL <http://onlinelibrary.wiley.com/doi/10.1002/cnm.2724/abstract>.
- [173] Hang Si and Klaus Gärtner. Meshing Piecewise Linear Complexes by Constrained Delaunay Tetrahedralizations. In *Proceedings of the 14th International Meshing Roundtable*, pages 147–163, Berlin/Heidelberg, feb 2005. Springer-Verlag. doi: 10.1007/3-540-29090-7_9. URL http://link.springer.com/10.1007/3-540-29090-7_{ }9.
- [174] Daniel a. Low and James F. Dempsey. Evaluation of the gamma dose distribution comparison method. *Medical Physics*, 30(9):2455, 2003. ISSN 00942405. doi: 10.1118/1.1598711. URL <http://scitation.aip.org/content/aapm/journal/medphys/30/9/10.1118/1.1598711>.

- [175] Pedro Andreo, David T Burns, Klaus Hohlfeld, M Saiful Huq, Tatsuaki Kanai, Fedele Laitano, Vere Smyth, and Stefaan Vynckier. Absorbed dose determination in external beam radiotherapy: an international code of practice for dosimetry based on standards of absorbed dose to water. *IAEA TRS*, 398, 2000.
- [176] R Zhang, WD Newhauser *Physics in Medicine & Biology*, and Undefined 2009. Calculation of water equivalent thickness of materials of arbitrary density, elemental composition and thickness in proton beam irradiation. *iopscience.iop.org*, 2009. URL <http://iopscience.iop.org/article/10.1088/0031-9155/54/6/001/meta>.
- [177] Rui Zhang, Phillip J Taddei, Markus M Fitzek, and Wayne D Newhauser. Water equivalent thickness values of materials used in beams of protons, helium, carbon and iron ions. *Physics in medicine and biology*, 55(9):2481–93, may 2010. ISSN 1361-6560. doi: 10.1088/0031-9155/55/9/004. URL <http://www.ncbi.nlm.nih.gov/pubmed/20371908><http://www.pubmedcentral.nih.gov/articlerender.fcgi?artid=PMC2977971>.
- [178] Mahmoud Reza Akbari, Hassan Yousefnia, and Ehsan Mirrezaei. Calculation of water equivalent ratio of several dosimetric materials in proton therapy using FLUKA code and SRIM program. *Applied Radiation and Isotopes*, 90:89–93, 2014. URL <https://www.sciencedirect.com/science/article/pii/S096980431400089X>.
- [179] Habib Safigholi and William Y Song. Calculation of water equivalent ratios for various materials at proton energies ranging 10–500 MeV using MCNP, FLUKA, and GEANT4 Monte Carlo codes. *Physics in Medicine and Biology*, 63, 2018. URL <https://iopscience.iop.org/article/10.1088/1361-6560/aad0bd/meta>.
- [180] Heeteak Chung, Sina Mossahebi, Arun Gopal, Giovanni Lasio, Huijun Xu, and Jerimy Polf. Evaluation of Computed Tomography Scanners for Feasibility of Using Averaged Hounsfield Unit-to-Stopping Power Ratio Calibration Curve. *International Journal of Particle Therapy*, 5(2):28–37, sep 2018. ISSN 2331-5180. doi: 10.14338/IJPT-17-0035.1. URL <http://theijpt.org/doi/10.14338/IJPT-17-0035.1>.
- [181] Pablo de Vera, Isabel Abril, and Rafael Garcia-Molina. Water equivalent properties of materials commonly used in proton dosimetry. *Applied Radiation and Isotopes*, 83:122–127, 2014. URL <https://www.sciencedirect.com/science/article/pii/S0969804313000249>.
- [182] Hugo Palmans and Frank Verhaegen. Calculated depth dose distributions for proton beams in some low- Z materials. *Physics in Medicine and Biology*, 42(6):1175–1183, jun 1997. ISSN 0031-9155. doi: 10.1088/0031-9155/42/

- 6/013. URL <http://stacks.iop.org/0031-9155/42/i=6/a=013?key=crossref.cd7460187262dd279f42cbc14fd39992>.
- [183] Wayne Newhauser, Jonas Fontenot, Nicholas Koch, Lei Dong, Andrew Lee, Yuanshui Zheng, Laurie Waters, and Radhe Mohan. Monte Carlo simulations of the dosimetric impact of radiopaque fiducial markers for proton radiotherapy of the prostate. *Physics in Medicine and Biology*, 52(11):2937–2952, jun 2007. ISSN 0031-9155. doi: 10.1088/0031-9155/52/11/001. URL <http://www.ncbi.nlm.nih.gov/pubmed/17505081><http://stacks.iop.org/0031-9155/52/i=11/a=001?key=crossref.913b3db1ad141a8a441179a4a2af179>.
- [184] Uwe Schneider, Eros Pedroni, and Antony Lomax. The calibration of CT Hounsfield units for radiotherapy treatment planning. *Physics in Medicine and Biology*, 41(1):111–124, jan 1996. ISSN 0031-9155. doi: 10.1088/0031-9155/41/1/009. URL <http://stacks.iop.org/0031-9155/41/i=1/a=009?key=crossref.7cef62664dbeba7f6a11f0639b13a9e8>.
- [185] B Schaffner and E Pedroni. The precision of proton range calculations in proton radiotherapy treatment planning: experimental verification of the relation between CT-HU and proton stopping power. *Physics in Medicine and Biology*, 43(6):1579–1592, jun 1998. ISSN 0031-9155. doi: 10.1088/0031-9155/43/6/016. URL <http://stacks.iop.org/0031-9155/43/i=6/a=016?key=crossref.44a553a6374b9036eca9bb3354fff29d>.
- [186] Harald Paganetti. Range uncertainties in proton therapy and the role of Monte Carlo simulations. *Physics in Medicine & Biology*, 57(11):R99, 2012. URL <https://iopscience.iop.org/article/10.1088/0031-9155/57/11/R99/meta>.
- [187] Siou-Yin Cai, Chao, , Tsi-Chain Lin, , Mei-Jyun Tung, , Chuan-Jung Lee, and Chung-Chi. Depth dose characteristics of proton beams within therapeutic energy range using the particle therapy simulation framework (PTSim) Monte Carlo technique. *Biomedical journal*, 38, 2015. URL http://biomedj.cgu.edu.tw/pdfs/2015/38/5/images/BiomedJ{}_2015{}_38{}_5{}_408{}_167076.pdf.
- [188] J. K. van Abbema, M. J. van Goethem, J. Mulder, A. K. Biegun, M. J.W. Greuter, A. van der Schaaf, S. Brandenburg, and E. R. van der Graaf. High accuracy proton relative stopping power measurement. *Nuclear Instruments and Methods in Physics Research, Section B: Beam Interactions with Materials and Atoms*, 436(September):99–106, 2018. ISSN 0168583X. doi: 10.1016/j.nimb.2018.09.015. URL <https://doi.org/10.1016/j.nimb.2018.09.015>.

-
- [189] Nick Gould and Philippe L Toint. Preprocessing for quadratic programming. *Mathematical Programming*, 100(1):95–132, may 2004. ISSN 0025-5610. doi: 10.1007/s10107-003-0487-2. URL <http://link.springer.com/10.1007/s10107-003-0487-2>.
- [190] Anna Altman and Jacek Gondzio. Regularized symmetric indefinite systems in interior point methods for linear and quadratic optimization. *Optimization Methods and Software*, 11(1-4):275–302, jan 1999. ISSN 1055-6788. doi: 10.1080/10556789908805754. URL <http://www.tandfonline.com/doi/abs/10.1080/10556789908805754>.